Environmental Factors Affecting CaO and $CaSO_4$-Induced Degradation of Second-Generation Nickel-Based Superalloys

by

Patrick Thomas Brennan

B.S.in Materials Science and Engineering, University of Pittsburgh, 2015

Submitted to the Graduate Faculty of the

Swanson School of Engineering in partial fulfillment

of the requirements for the degree of

Doctor of Philosophy

University of Pittsburgh

2020

UNIVERSITY OF PITTSBURGH

SWANSON SCHOOL OF ENGINEERING

This dissertation was presented

by

Patrick Thomas Brennan

It was defended on

February 7, 2020

and approved by

Gerald H. Meier, PhD., Professor, Department of Mechanical Engineering and Materials Science

Wei Xiong, PhD., Assistant Professor, Department of Mechanical Engineering and Materials Science

David Waldeck, PhD., Professor, Department of Chemistry

Dissertation Director: Brian M. Gleeson, PhD., Harry S. Track Chair Professor, Department Chairman, Department of Mechanical Engineering and Materials Science

Environmental Factors Affecting CaO and $CaSO_4$-Induced Degradation of Second-Generation Nickel-Based Superalloys

Patrick Thomas Brennan, PhD

University of Pittsburgh, 2020

The goal of this research project was to provide fundamental understanding of CaO- and $CaSO_4$-induced degradation observed in aviation gas-turbine engines and to develop a lab-scale test procedure which accurately replicates the degradation observed in field-exposed components. Based on initial assessments, particular attention was paid to characterizing the nature of breakaway internal oxidation caused by $CaSO_4$ deposits and determining how $CaSO_4$-alloy interactions induce subsurface changes in the alloy composition and microstructure which can make the alloy susceptible to internal attack.

Both SEM and TEM analyses were used to characterize the morphology of degradation in field-exposed components. Emphasis was placed on characterizing the composition and phase distribution in the internal oxidation zone (IOZ). Isothermal experiments were conducted to investigate the interactions that take place between CaO or $CaSO_4$ deposits and single crystal superalloys at elevated temperatures. This was achieved by exposing Rene N5 and N500 coupons with CaO or $CaSO_4$ deposits at 900°C or 1150°C in air for various times and characterizing the reaction product. From the results obtained, a novel bi-thermal test procedure was developed which successfully replicated the degradation that occurs in the field-exposed components. It was determined that degradation of the subsurface caused by $CaSO_4$ at 1150°C made the alloys susceptible to internal oxidation when exposed to conditions that better simulate the gas-turbine environment. Following this result, sets of systematic experiments were developed to determine how the environmental variables of atmosphere, thermal profile, and deposit mass influence the

oxidation behavior of a subsurface-depleted alloy and how the behavior is linked to the kinetic competition between internal and external oxidation. Finally, it was observed that N5 is more resistant to $CaSO_4$-induced degradation than N500. Because of this, the influence of alloy composition on the degradation resistance of nickel-based alloys was explored by conducting bi-thermal experiments with $CaSO_4$ deposit on a superalloy with intermediate composition to that of N5 and N500 and by conducting oxidation experiments on model Ni-Cr-Al-Re alloys.

Table of Contents

List of Tables

List of Figures

Acknowledgements

I believe that passion and determination will always bring success to an individual, but that the ultimate heights an individual can achieve is raised by the people who support them. To that end, I wish to express my deepest appreciation to the people in my life who have helped me grow both academically and personally.

First, I thank my current and former committee members: Prof. Gerald Meier, Prof. Wei Xiong, Prof. David Waldeck, and Prof. Jill Millstone for their insightful comments on my research throughout the entire dissertation process.

To my parents, Steve and Presila: your unwavering love and support in all aspects of my life, and the guidance that you've provided, have led me to this academic achievement. I also know that your support will continue to be the foundation of any future achievements. It is to you whom I owe the greatest debt of gratitude.

To my undergraduate professors and personal mentors Gerald Meier, Ian Nettleship, David Schmidt, and Jorg Wiezorek: your mentoring has helped me navigate both the challenging and successful periods that come with the graduate school experience.

To my labmates Nate Bohna, Satia Soltanattar, Emily Kistler, Matt Kovalchuk, Grace de Leon Nope, and Preston Nguyen: for your friendship, ideas, comradery and the personal support that is so crucial to success in graduate school.

To Doug Konitzer and Mike Brennan of GE Aviation: for sharing your expertise with gas-turbine engines which helped guide the project. I must also thank you for being gracious, accomodating, and insightful during my internship at GE Aviation in the summer of 2017.

Finally, I must thank my advisor Dr. Brian Gleeson. Of all the support and encouragement that you have provided to me, the most impactful was seeing how you conduct yourself, and the courtesy and respect with which you treat your work, colleagues, and students. You have been a mentor to me in every sense of the word and I hope to live up to the example that you have set for me.

1.0 Introduction

The commercial aviation industry has grown from its humble origin of carrying small shipments of cargo and passengers in the early twentieth century to becoming a critical generator of economic growth across the world. In 2018, the commercial aviation industry transported a record number of passengers - more than 4.3 billion - generating revenues of $564 billion [1]. Commercial aviation was also responsible for shipping 70.2 billion tons of freight that generated an additional $109.8 billion of revenue [1]. The impact of the commercial aviation industry on our society can be partly attributed to the increasing efficiency of the engines that propel modern aircraft. Highly efficient engines allow people and material to be transported further, faster, and comparatively cheaper than ever before. The predominant technology used for propulsion in commercial aviation today is the high bypass turbofan [2].

A high bypass turbofan operates by drawing air into the engine with the fan blades at the front of the engine. Most of the air is diverted to the "bypass" where it is slightly compressed causing it to accelerate out of the back of the engine to generate most of the engine's thrust. The air diverted to the core of the engine is compressed up to 30 atmospheres of pressure by several stages of compressor blades before it is mixed with jet fuel and ignited in the combustion chamber. The hot expanding gases turn a series of turbine blades which generate electricity for the aircraft's systems and turn the fan blade to draw in more air. A schematic diagram of a turbofan is shown in Fig. 1.1 [2].

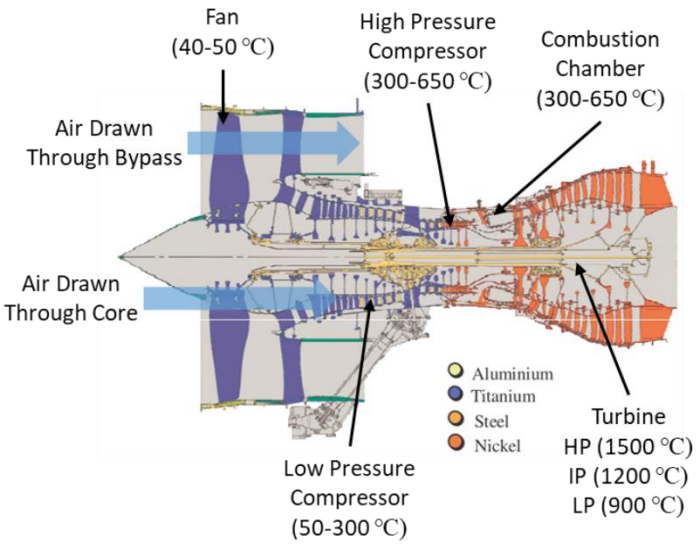

Figure 1-1. Schematic diagram of a turbofan engine used for aero-propulsion. Given temperatures are the approximate gas temperature in each section of the engine [2].

Of particular interest to this research are the materials that are used to make airfoils and shrouds for the high-pressure turbine (HPT). The HPT environment poses one of the most significant materials development and selection challenges in a turbofan engine. Turbine blades can rotate at up to 10,000 rpm which generates large stresses and the temperature of the inlet gas can be as hot at 1500°C [2]. The implementation of active cooling channels and application of thermal barrier coatings on the components means that components in the gas path can reach surface temperatures as high as 1200°C [2–4]. The large stresses and high temperatures that the components are exposed to demand that they be made of a material that has good high temperature mechanical properties and environmental stability. The materials best suited for this application are nickel-based superalloys.

The specific class of superalloys most commonly used at present to make components that serve in the gas path of the HPT are single crystal superalloys. These alloys are optimized with respect to their high temperature mechanical properties and creep life. They maintain a relatively

high yield strength at temperatures as high as 0.8 T_m ($T_m \approx$ 1300-1350 °C) and can withstand brief exposures to temperatures as high as 1200°C [3]. The alloys are also resistant to creep rupture, the failure of a material due to time dependent creep deformation, during the service life of the component which can last up to 5,000,000 flying miles [2, 3]. The long service life of engine components is important to maintaining the efficiency of commercial aviation by minimizing maintenance time and the associated expenses. This is not an insignificant concern as engine maintenance is the largest line item for total fleet maintenance expenses. In 2016, the commercial aviation industry spent $67.6 billion on fleet maintenance. Of this total, 39% - roughly $26.4 billion - was spent on engine maintenance [5]. However, the useful service life of components may also be limited by the rate at which they degrade due to oxidation and corrosion.

During service at elevated temperature, alloys can be rapidly attacked by reactions with oxidants in the atmosphere and/or airborne contaminants such as sulfates which can form corrosive deposits on the components [6]. Alloys with poor environmental resistance have a greater likelihood of early failure due to corrosion and stress corrosion cracking. If the accelerated degradation via oxidation or corrosion continues unabated, the component must be pulled from service prematurely and replaced. Such unwanted degradation can be prevented by adding sufficient aluminum and chromium to nickel-based superalloys to promote the formation of an Al_2O_3 scale that acts as a diffusion barrier between the alloy and the oxidants in the atmosphere. Al_2O_3 is ideal for oxidation and corrosion resistance in the HPT environment because it is a slow growing oxide that is very thermodynamically stable. However, there are some aggressive environmental conditions which can breakdown or prevent the establishment of Al_2O_3 leading to excessive degradation. In aero-turbines, the most common of these forms of attack is “high temperature corrosion” induced by sulfate deposits.

High temperature corrosion of aero-turbine components is an area of research that has been active since the 1960's [7]. Hot corrosion was first reported to cause accelerated oxidation and sulfidation of high-pressure turbine components in military aircraft during the Vietnam War [8]. Similar forms of attack via sulfate deposits are also observed in high-temperature systems for power generation [9] and naval propulsion [10]. Due to the impact of deposit-induced attack across a variety of applications, there is a large body of research on the influences of temperature, atmosphere, alloy composition, and deposit composition on the modes and extents of deposit-induced degradation. However, for the case of aero-applications, nearly all of the past research examines degradation induced by Na_2SO_4 deposits [7]. Na_2SO_4-induced hot corrosion occurs due to the acidic or basic dissolution and subsequent fluxing of the oxide scales in a liquid sulfate film. The fluxing process precludes the establishment or re-establishment of protective oxide scales and results in a rapid oxidation and sulfidation of the alloy. An excellent review of the fluxing processes has been provided by Rapp [8]. The predominant focus on degradation caused by Na_2SO_4 deposits in aero-turbines has, to some extent, resulted in a knowledge gap between the degradation catalogued at the lab-scale and that which takes place in field-exposed components.

For instance, recent publications [7, 11] have reported oxidation-sulfidation attack in high-pressure turbine airfoils and shrouds in the presence of calcium-rich deposits. While modes of degradation associated with calcium-rich deposits have been investigated for applications such as the fluidized bed combustion of coal [12–14], there are currently no published explanations for similar modes of degradation in aero-engine components.

The primary focus for this dissertation research was to develop an understanding of the mechanisms by which calcium-rich deposits can cause accelerated degradation in single-crystal Ni-base superalloys which have a microstructure comprised of a high volume fraction of γ'-Ni_3Al

precipitates in a matrix of γ-Ni. Particular focus was placed on reproducing breakaway internal oxidation observed in field-exposed components with $CaSO_4$ deposit. The component sections were supplied by GE Aviation. Representative cross-sectional micrographs of the degradation observed in these components are shown in Fig. 1.2. The degradation microstructure consists of three characteristic features. There is a dense external layer of nickel-rich oxide with cobalt in solution above an internal oxidation zone with "dendrite-like" intrusions of Al- and Cr-rich oxides. Lastly, a fine distribution of CrS precipitates is typically present in the γ'-denuded zone ahead of the internal oxidation front. More detailed characterization of the reaction product will be presented in chapter 5.

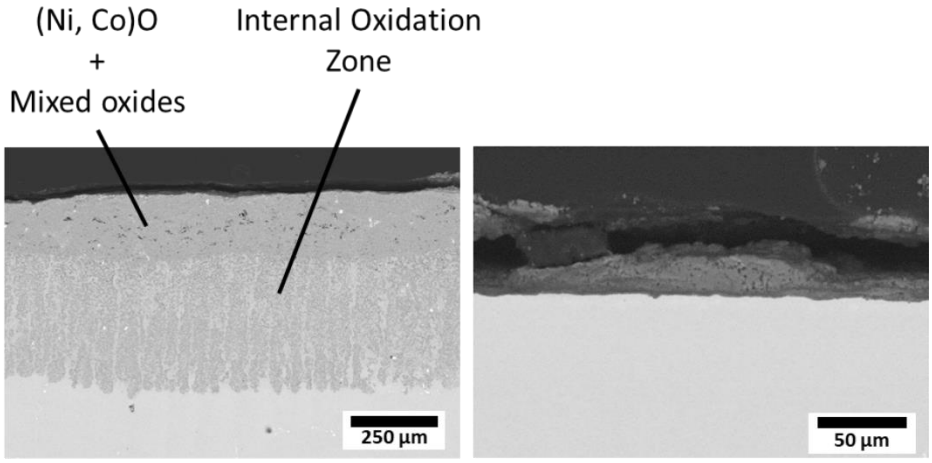

Figure 1-2. The degradation observed in field-exposed components.

The goals of this thesis research were to develop an understanding of the modes of degradation caused by calcium-rich deposits in the high-pressure turbine of aero-engines and to develop lab-scale experiments which replicate these modes of degradation. The result of this research will broaden our understanding of deposit-induced hot corrosion of aero-turbine components and will allow corrosion mitigation strategies to be better targeted against the modes

of degradation that components will face during service. Additionally, the development of a lab-scale testing procedure will allow materials scientists to better evaluate and rank current and future alloys for gas-turbine applications. This tool may lead to the development of alloys with increased service life that improve engine operating efficiency.

2.0 Background and Fundamentals

2.1 Structure and Properties of Second-Generation Single Crystal Nickel-Based Superalloys

The exceptional high temperature mechanical properties and oxidation resistance of single crystal 2nd generation nickel-based superalloys are derived from their carefully controlled composition, phase distribution, and microstructure [3, 4, 15]. The basis of these alloys are the γ and γ' phases in the nickel-aluminum binary system (Fig. 2.1). γ is the FCC Ni solid solution phase (A1) and γ' is the intermetallic Ni_3Al phase ($L1_2$).

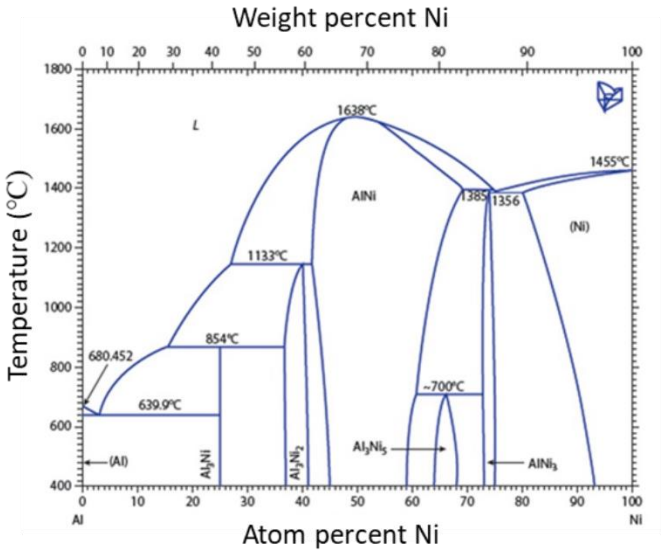

Figure 2-1. Binary Ni-Al phase diagram [16].

The optimal distribution of the two phases in these alloys is a γ matrix with semi-coherent sub-micron cuboidal γ' precipitates with a precipitate volume fraction between 60-75%. The γ'

precipitates are an ideal phase for strengthening because their semi-coherent nature and high shear strength makes them resistant to “cutting through” by dislocations. This increases the alloy’s resistance to plastic deformation by yielding and by time-dependent creep deformation [3]. γ’ precipitate strengthening persists at temperatures as high as 1200°C because the dissolution temperature of the γ’ is typically only 30-100°C below the solidus of the alloy [4]. An example of the γ + γ’ microstructure in a superalloy is shown in Fig. 2.2. The effect of γ’ precipitation strengthening on the tensile properties and creep strength of two phase γ + γ’ alloys compared to single phase γ or γ’ alloys is shown in Fig. 2.3.

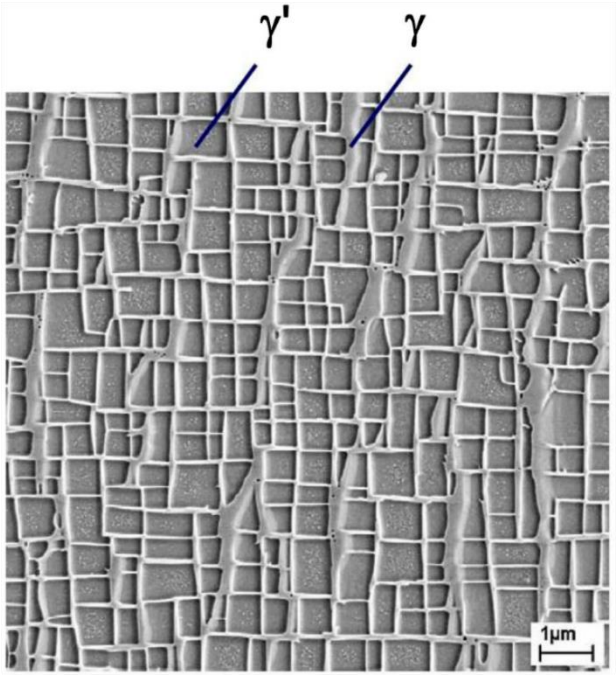

Figure 2-2. Microstructure of a nickel-based superalloy. Cuboidal γ’ precipitates in a γ matrix [15].

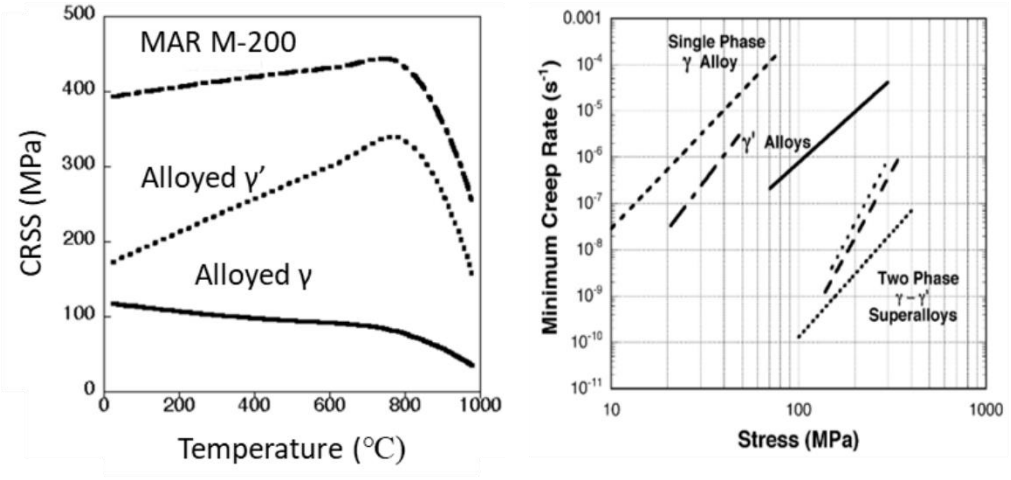

Figure 2-3. Effect of γ' precipitate strengthening on critical resolved shear stress (left) and creep rate (right) of nickel-based alloys [3].

Another key microstructural feature of these alloys is that they are cast as single crystals to further increase their maximum service temperature by improving creep resistance at very high temperatures. At temperatures above 1000°C, the thermomechanical creep process is dominated by stress-directed atomic diffusion [17]. The elimination of grain boundaries decreases atomic diffusivity in the alloy by removing the short circuit diffusion paths for atoms and vacancies. Slowing the atomic diffusion in the alloy decreases the creep rate and results in an increase in the alloys expected creep rupture life [3].

Controlling the microstructure of these alloys begins during the single crystal casting process. Single crystal components are cast by vacuum induction melting an ingot and pouring the molten alloy into a heated mold. A seed crystal at the bottom of the mold acts as a nucleation site to encourage solidification along the (001) orientation during cooling. The cooling rate of the melt is carefully controlled by withdrawing the mold from the furnace to maintain a unidirectional thermal gradient which is necessary for single crystal growth. Complex part geometries, such as turbine blades with internal cooling channels, can be realized by using a complex mold structure

which can be dissolved during post processing. A schematic diagram of the single crystal casting process is shown in Fig. 2.4 [3]. After casting, the phase distribution and chemical segregation in the alloy is controlled through heat treatment by homogenizing the alloy at a temperature between the γ' dissolution temperature and the solidus temperature. Subsequently, an aging treatment is used to control the distribution, shape, and size of the γ' precipitates to achieve the desired mechanical properties [18].

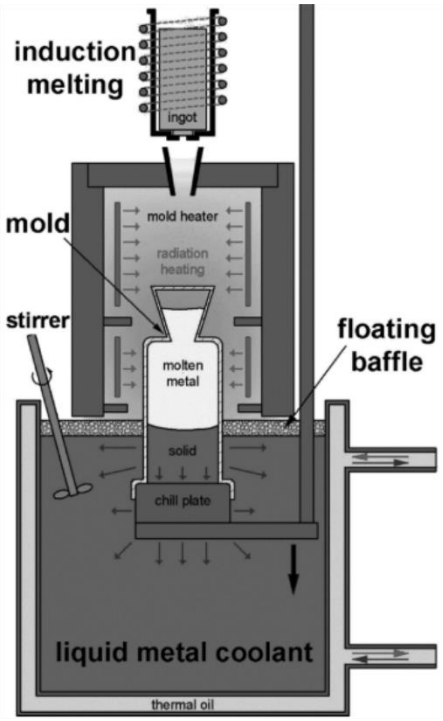

Figure 2-4. Schematic diagram of the single crystal casting process [3].

In additional to nickel and aluminum; elements such as cobalt, chromium, hafnium, molybdenum, rhenium, tantalum, titanium, tungsten, and yttrium are added to further improve mechanical properties and oxidation resistance of the alloy [3]. The roles of these alloying elements are complex, but they can be roughly grouped into two primary categories. The first

category are elements added for solid solution strengthening of the γ and γ'. Co, Mo, Re, and W are elements which partition to and strengthen the γ-phase while Ta and Ti partition to and strengthen the γ'-phase. The second category of elements are added to increase the oxidation and corrosion resistance of the alloys. These elements are Cr, Hf, and Y. The addition of chromium to the alloys decreases the concentration of aluminum in the alloy necessary to form and maintain a protective Al_2O_3 scale [19] while hafnium and yttrium slow the oxidation rate and increase the adhesion of the Al_2O_3 scale through the "reactive element effect" [20]. The fundamentals of the selective oxidation of aluminum in nickel-based alloys to form a protective Al_2O_3 scale, along with the compositional and environmental factors which effect this process, will be covered in greater detail in section 2.2.

2.2 Oxidation of Nickel-Based Alloys

2.2.1 Thermodynamics, Kinetics, and Mechanisms of Al_2O_3 Scale Formation

The oxidation of metals is a phenomenon that occurs for all structural metals and alloys in high temperature environments. For a metal or alloy to be "resistant" to oxidation or corrosion during service, the material's oxidation rate - the rate at which an oxide product develops - must be low. This is achieved when the alloy can grow a compact and adherent oxide scale, such as Al_2O_3 on its surface. Such a scale acts as a diffusion barrier to slow the consumption of metal by oxidation. As a result, superalloys which serve in the high-pressure turbine of aero-engines are designed to ensure that aluminum in the alloy is preferentially oxidized to form an external α-Al_2O_3 scale [15].

A more generalized treatment of alloy oxidation will now be presented. Criteria for the selective oxidation of element B in an alloy A-B [21] are presented below. If these criteria are met, the outward diffusion of B to the surface of the alloy will be sufficient to form a continuous external BO_υ scale.

1.) The value of ΔG^o of formation (per mole O_2) for the solute metal oxide, BO_v, must be more negative than ΔG^o of formation (per mole O_2) for the base metal oxide AO_v.
2.) The value of ΔG for the reaction $B + v\underline{O} = BO_v$ must be negative. Therefore, the base metal must have a solubility and diffusivity for oxygen which is sufficient to establish the required activity of dissolved oxygen $\underline{O}$ at the reaction front to form BO_υ.
3.) The concentration of B in the alloy must be higher than that required for the transition from external to internal oxidation.

The classical treatments for the mechanisms and kinetics of oxide scale growth were proposed by Wagner based on seven critical assumptions [22]:

1.) The oxide layer is a compact, perfectly adherent scale.
2.) Migration of ions or electrons across the scale is the rate-controlling process.
3.) Thermodynamic equilibrium is established at both the metal–scale and scale–gas interfaces.
4.) The oxide scale shows only small deviations from stoichiometry and, hence, the ionic fluxes are independent of position within the scale.
5.) Thermodynamic equilibrium is established locally throughout the scale.

6.) The scale is thick compared with the distances over which space charge effects (electrical double layer) occur.

7.) Oxygen solubility in the metal may be neglected.

In Wagner's theory for oxide scaling, the growth of an oxide scale is driven by a chemical potential gradient for oxygen and metal ions between the scale-gas and scale-alloy interface. This gradient drives the diffusion of ions from one interface to the other which in turn establishes an electrical potential across the scale. This electrical potential drives the transport of electrons from the scale-alloy interface to the scale-gas interface and facilitates the chemical reactions necessary to form new oxide at the scale-alloy and/or scale-gas interface. A schematic for these processes is shown in Fig. 2.5.

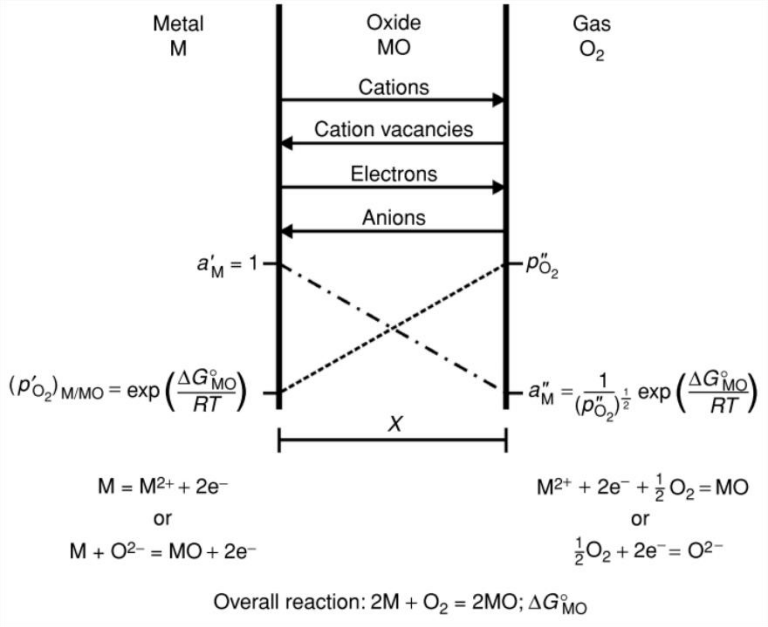

Figure 2-5. Diffusion of electronic species through a scale in Wagner's model for oxidation [21].

Because the diffusion of charged species through the scale is the rate limiting step for oxidation, the growth of a scale of thickness X with respect to time t is parabolic (equation 2.1). Therefore, the oxidation rate of an alloy that forms a compact oxide scale decreases with increasing exposure time and scale thickness.

$$x^2 = k_p t \tag{2.1}$$

In equation 2.1, k_p is the parabolic rate constant for oxidation. In Wagner's theory, k_p can be related to the self-diffusion coefficients of the ions in the oxide by equation 2.2.

$$k_p = \int_{scale-alloy\ int}^{scale-gas\ int} \left(v \frac{D_B^*}{f_M} + \frac{D_O^*}{f_O} \right) d\left(ln a_{O_2}\right) \tag{2.2}$$

D^* are the self-diffusion coefficients of metal and oxygen ions in the oxide, v is the stoichiometric constant for an oxide BO_v, f are the correlation coefficients for diffusion (these values are near unity) and the limits of integration are the boundary conditions at the scale-alloy and scale-gas interfaces.

While Wagner's theory establishes the fundamental treatment for oxidation, when experimentally measured rate constants are compared to those calculated from equation 2.2, larger than predicted rate constants are measured for many oxides, including Al_2O_3 [23]. The difference between the observed growth rate for Al_2O_3 and that predicted by equation 2.2 comes from factors not considered in Wagner's theory. The most influential of these factors is the presence of grain boundaries in the oxide scale. The microstructure of thermally grown Al_2O_3 typically consists of

columnar grains throughout the thickness of the scale with equiaxed grains near the scale-gas interface [24]. An example of this microstructure is shown in Fig. 2.6.

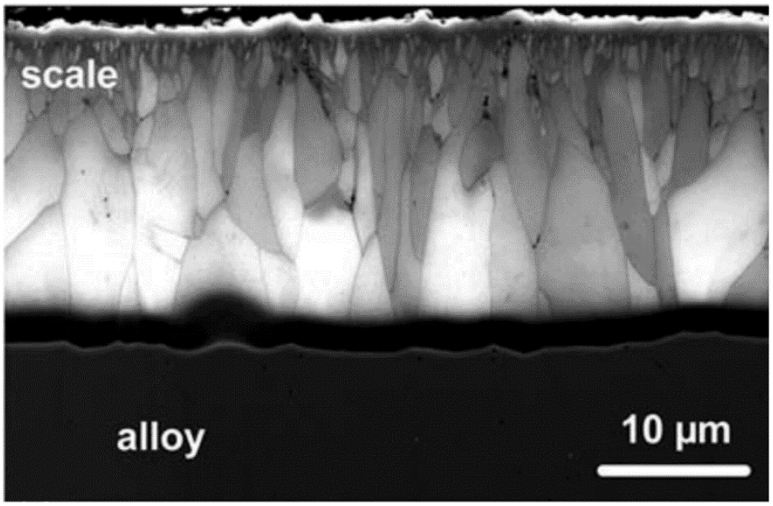

Figure 2-6. SEM micrograph of Al_2O_3 grown on FeCrAlY after 2000 h at 1200°C [25].

The influence of grain boundaries on the effective diffusion coefficients of cations and anions through the scale can be demonstrated by equation 2.3 where D_{gb} is the grain boundary diffusion coefficient, δ is the grain boundary width and g is the grain size in the oxide.

$$D_{eff} = D_{lattice} + 2\frac{(D_{gb}\delta)}{g} \tag{2.3}$$

While there is variability in the data regarding the lattice and grain boundary diffusivity of oxygen and aluminum in Al_2O_3, it is likely diffusion through grain boundaries is several orders of magnitude greater than diffusion through the lattice [26, 27]. Because of this, the oxidation kinetics of Al_2O_3 are controlled by the faster grain boundary diffusion [28].

The specific transport process for ions through thermally grown Al_2O_3 on Fe-Cr-Al and Ni-Al alloys with and without additions of the reactive element (RE) yttrium were determined through experiments using ^{18}O and ^{16}O during different stages of an oxidation exposure [29, 30]. The influence of RE additions - such as Ce, Hf, La, Y, and Zr - on the mechanism of Al_2O_3 growth is covered in this review because Hf and Y are added to the commercial alloys studied for this thesis.

The oxygen tracer experiments on Fe-Cr-Al [29] began by oxidizing the alloys for 3 h at 1000°C in air enriched with 10% ^{18}O. The furnace tube was then evacuated and filled with standard air for 9 h during the second stage of the exposure. After the experiment, secondary ion mass spectroscopy was used to determine where new Al_2O_3 forms during oxidation by measuring the concentration of ^{16}O in the scale as a function of depth from the scale gas interface. The results revealed that new oxide formed at both the scale-gas and scale-alloy interface on the RE-free alloy and that new oxide formed only at the scale-alloy interface in the RE-containing alloy. The same behavior was observed for Al_2O_3 growth on NiAl and NiAlY alloys [30]. The formation of new oxide only at the scale-alloy interface in RE-containing alloys proved that the addition of reactive elements to Al_2O_3-forming alloys suppresses the outward diffusion of Al^{3+} through the scale. Therefore, Al_2O_3 growth in the Hf- and Y-containing alloys investigated for this research project occurs through the inward diffusion of oxygen through the Al_2O_3 scale.

More recent analysis has attempted to explain the oxidation behavior of Al_2O_3 with and without RE additions by linking the defect species that are generated at the scale-alloy and scale-gas interfaces to the transport of oxygen and aluminum ions through grain boundaries. The speciation of defects generated are in turn dictated by the oxygen partial pressure at the scale-alloy

and scale-gas interfaces and the presence of reactive element dopants. This more recent analysis is elaborated in the following.

During oxidation in air at 1000°C, the P_{O_2} at the scale-alloy interface is roughly 10^{-31} Pa as defined by the equilibrium between Al and Al_2O_3. The P_{O_2} at the scale-gas interface is roughly 2 x 10^4 Pa. Kitaoka et al. [31] determined that the dissociation of oxygen to create oxygen vacancies by the reaction in equation 2.4 occurs at the low P_{O_2} scale-alloy interface and that O_2 molecules are adsorbed at the high P_{O_2} scale-gas interface to generate aluminum vacancies by the reaction in equation 2.5.

$$O_O^{\times} \rightarrow \frac{1}{2} O_2 + V_O^{\bullet\bullet} + 2e' \tag{2.4}$$

$$\frac{1}{2} O_2 \rightarrow O_O^{\times} + \frac{2}{3} V_{Al}''' + 2h^{\bullet} \tag{2.5}$$

In a RE-free Al_2O_3-forming alloy, the outward diffusion of the oxygen vacancies generated at the scale-alloy interface results in a counter flow of oxygen ions inward to the scale-alloy interface. Likewise, the inward diffusion of aluminum vacancies generated at the scale-gas interface results in the outward diffusion of aluminum to the scale-gas interface. It is by these processes that new Al_2O_3 forms at both the scale-alloy and scale-gas interfaces in alloys without RE additions. The mechanism by which RE's affect Al_2O_3 growth have been investigated by Heuer et al. [27]. The authors determined that adding Hf or Y to the alloy resulted in RE segregation to the grain boundaries of thermally-grown Al_2O_3. The presence of this segregation modifies the donor/acceptor grain boundary states which inhibits the ionization of Al at the scale-alloy interface

resulting in less outward diffusion of aluminum to the scale-gas interface to form new oxide. This leaves the inward diffusion of oxygen to the scale-alloy interface as the primary mechanism for the growth of Al_2O_3 in RE doped alloys.

While Al_2O_3 scale formation is the desired behavior for Ni-based superalloys, under harsh exposure conditions, an alloy may be unable to establish or maintain external Al_2O_3. When this occurs, aluminum will oxidize in the bulk of the alloy as non-protective discontinuous oxide precipitates leaving the base alloy susceptible to reaction. Therefore, understanding the factors that dictate the transition between external oxidation and non-protective internal oxidation is necessary to understanding the degradation observed in the field-exposed components.

2.2.2 Thermodynamics, Kinetics, and Mechanisms of Internal Aluminum Oxidation

Internal oxidation of aluminum in a nickel-based alloy occurs when the supply of aluminum to the oxidation front is insufficient to establish or maintain an external Al_2O_3 scale. In this case, there is no barrier to slow the permeation of oxygen into the alloy and discontinuous Al_2O_3 precipitates form in the alloy at the interface where the equilibrium activity product, $a_{Al}a_O^{1.5}$, for Al_2O_3 formation is established [32]. The fundamental treatment for the kinetics of internal oxidation provided by Rapp based on the assumed conditions in Fig. 2.7 is presented below [33].

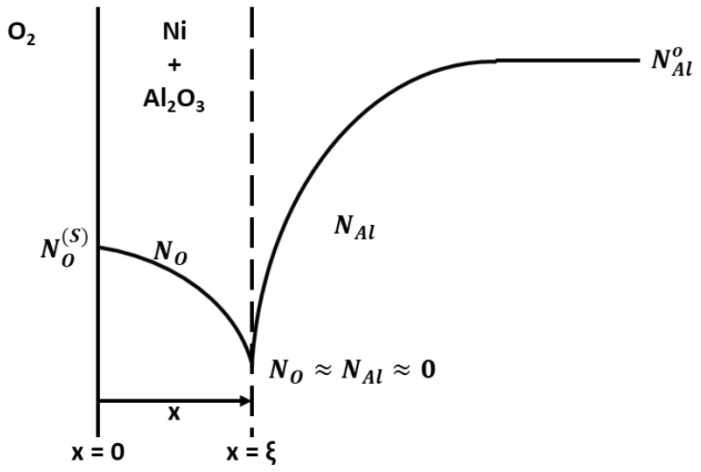

Figure 2-7. Concentration profiles used to derive internal oxidation kinetics. N_O and N_{Al} are the mole fraction of O and Al in the alloy, $N_O^{(S)}$ is the mole fraction of O at the external surface, and N_{Al}^{o} is the mole fraction of Al in the bulk alloy.

The depth "ξ" of the internal oxidation zone is shown in equation 2.6. The rate limiting step for internal oxidation is the diffusion of oxygen to the oxidation front. The corresponding velocity of the internal oxidation front (equation 2.7) is given by taking the derivative of equation 2.6 with respect to time.

$$\xi = 2\gamma(D_O t)^{\frac{1}{2}} \tag{2.6}$$

$$\frac{d\xi}{dt} = \gamma\left(\frac{D_O}{t}\right)^{\frac{1}{2}} \tag{2.7}$$

γ is a time-independent dimensionless parameter which can be determined by solving for N_O and N_{Al} as a function of position in the alloy using the error function solution for Fick's 2nd law with the following boundary conditions (equations 2.8-11).

$$N_O = N_O^{(S)} \; for \; x = 0 \; and \; t > 0 \tag{2.8}$$

$$N_O = 0 \; for \; x \geq \xi \; and \; t > 0 \tag{2.9}$$

$$N_{Al} = N_{Al}^{o} \; for \; x > 0 \; and \; t = 0 \tag{2.10}$$

$$N_{Al} = 0 \; for \; x \leq \xi \; and \; t > 0 \tag{2.11}$$

Assuming that $\frac{D_{Al}}{D_O} \ll \frac{N_O^{(S)}}{N_{Al}^{o}} \ll 1$, equation 2.6 becomes equation 2.12 and equation 2.7 becomes equation 2.13 where v =1.5 is the stoichiometric ratio for an oxide BO_v ($AlO_{1.5}$).

$$\xi = \left[\frac{2N_O^{(S)} D_O}{vN_{Al}^{o}} t\right]^{1/2} \tag{2.12}$$

$$\frac{d\xi}{dt} = \left[\frac{N_O^{(S)} D_O}{2vN_{Al}^{o} t}\right]^{1/2} \tag{2.13}$$

In most practical applications, the P_{O_2} of the atmosphere is high enough to form NiO which means that the internal oxidation zone is formed below an external NiO scale. The internal oxidation observed in the field-exposed components exhibits this general morphology. Therefore, the kinetics of internal oxidation in combination with external scale formation is reviewed below.

The modifications to the kinetic model for internal oxidation with external scale formation were first published by Maak [34]. There are two additional considerations for this model. The first is that the oxygen solubility $N_O^{(S)}$ is dictated by the equilibrium P_{O_2} between the external scale and the alloy at the scale-alloy interface. The second is that the problem becomes a moving boundary problem because the position of the external scale-alloy interface advances as the external scale thickens. A schematic of the internal oxidation process with external scale formation is provided in Fig. 2.8. In this situation, x becomes the distance from the original external surface, X is the position of the external scale-IOZ interface and ξ is the position of the internal oxidation front. The new boundary conditions used to derive the internal oxidation kinetics with external scale growth are presented in equations 2.14-17.

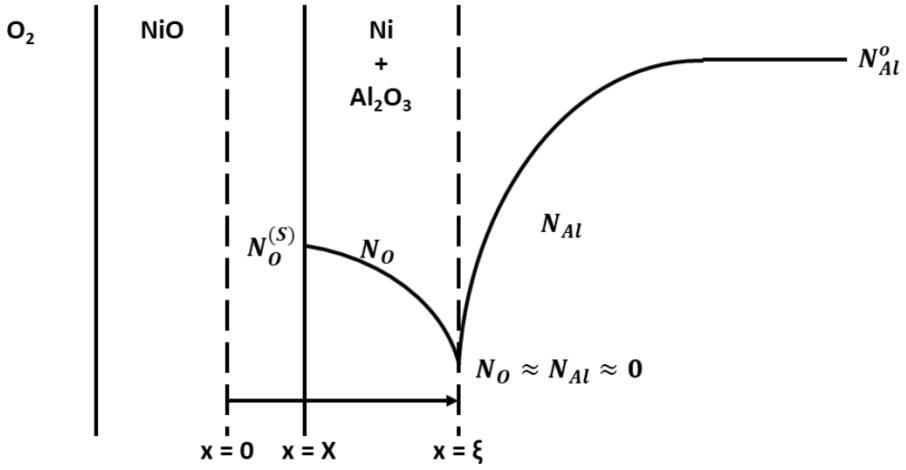

Figure 2-8. Concentration profiles used to derive internal oxidation kinetics where N_o and N_{Al} are the mole fraction of O and Al in the alloy, $N_O^{(S)}$ is the mole fraction of O at the external scale-alloy interface, and N_{Al}^{o} is the mole fraction of Al in the bulk alloy.

$$N_O = N_O^{(S)} \; for \; x = X \; and \; t > 0 \tag{2.14}$$

$$N_O = 0 \; for \; x \geq \xi \; and \; t > 0 \tag{2.15}$$

$$N_{Al} = N_{Al}^{o} \; for \; x \geq 0 \; and \; t = 0 \tag{2.16}$$

$$N_{Al} = 0 \; for \; x \leq \xi \; and \; t > 0 \tag{2.17}$$

Doing the same analysis which yielded equation 2.12 will yield the expression which defines the kinetics for internal oxidation with external scale formation (equation 2.18) where F is an auxiliary function described by $F(u) = \pi^{\frac{1}{2}} u e^{u^2} erfc(u)$.

$$N_O^{(S)} D_O = N_{Al}^{o} \times \frac{\xi(\xi - X)}{2t} \times \frac{1}{F\left(\frac{\xi}{2(D_{Al}t)^{\frac{1}{2}}}\right)} \tag{2.18}$$

The typical internal oxidation morphology for a nickel-based alloy oxidized in a high P_{O_2} environment is shown below in Fig. 2.9. From the outer part of the product to the inner part, there are four distinct regions. First, there is an external NiO scale. Below this is a region of NiO + $NiAl_2O_4$ which forms when the external NiO layer advances into the IOZ and envelops the internal oxide precipitates. The internal oxidation zone consists of two regions of rod-like oxide precipitates. The outer region is alloy + $NiAl_2O_4$ precipitates and the inner region is alloy + Al_2O_3 precipitates. This IOZ assemblage is a result of the oxygen concentration in the internal oxidation

zone and the intermediate thermodynamic stability of $NiAl_2O_4$ between NiO and Al_2O_3. In the first 65-70% of the IOZ, the concentration of oxygen is typically above that required for the reaction $NiO + Al_2O_3 = NiAl_2O_4$ to proceed. In the last 30-35% of the IOZ, the concentration of oxygen in the drops below this value but remains above what is necessary for Al_2O_3 formation. The development of this product is well described by Hindam and Whittle [35].

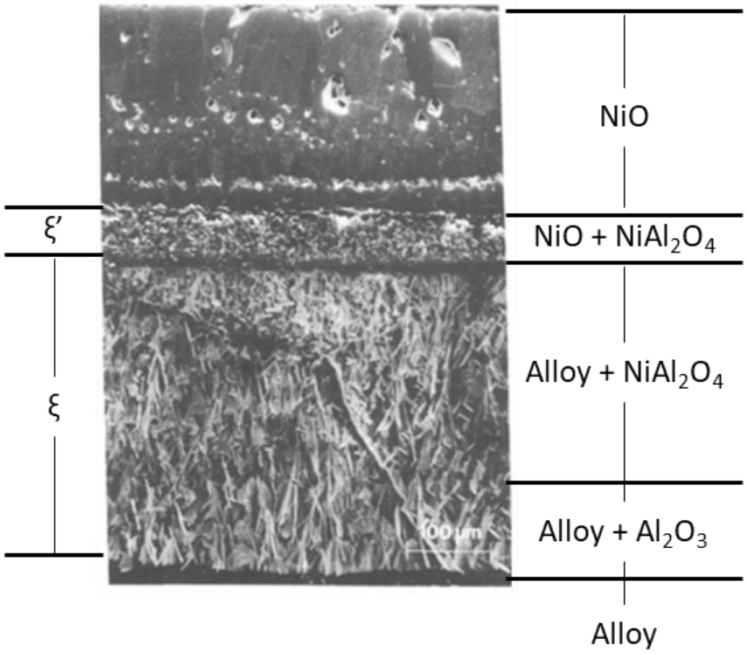

Figure 2-9. Typical assemblage of the reaction product which results from the internal oxidation of Al_2O_3-forming nickel-based alloys [35].

2.2.3 Factors Dictating the Transition Between External and Internal Oxidation Behavior

The transition between external and internal oxidation of Al in an Al_2O_3-forming nickel-based alloy is largely a function of the concentration of Al in the alloy. Protective external oxidation occurs if the alloy can 1.) initially establish an external scale during exposure and 2.) subsequently maintain the supply of Al to the oxidation front necessary to maintain the growth of

the oxide scale. Wagner once again developed the classical treatment for determining the critical concentration of B in an alloy A-B alloy required to establish and maintain an external oxide scale [32]. These treatments are reviewed in [21].

The critical concentration of Al required to establish an external Al_2O_3 scale is calculated by equating the number of moles of Al arriving at the internal oxidation front via diffusion to the number of moles of oxide per volume element in the IOZ. This mass balance is presented in equation 2.19.

$$\frac{f A d\xi}{V_m} = \left[\frac{A D_{Al}}{V_m}\frac{\partial N_{Al}}{\partial x}\right] dt \tag{2.19}$$

On the left side of the equation, f is the mole fraction of Al_2O_3 precipitates at the oxidation front and V_m is the molar volume of the alloy. f/V_m is the concentration of oxide per volume. The number of moles of oxide in a volume element $Ad\xi$ is $(f/V_m)Ad\xi$ where A is the cross-sectional area for diffusion. The right side of the equation is the number of moles of Al arriving at the oxidation front by diffusion in the time dt. By substituting equation 2.12 and the error function solution for $N_{Al}(x, t)$ into equation 2.19, the enrichment factor α, which represents the accumulation of oxide in the IOZ, can be derived as equation 2.20.

$$\alpha = \frac{f}{N_{Al}^o} \approx \frac{2v}{\pi}\left[\frac{N_{Al}^o D_{Al}}{N_O^{(S)} D_O}\right] \tag{2.20}$$

If the volume fraction of oxide at the oxidation front, $g = f\frac{V_{ox}}{V_M}$, reaches a critical value, g^*, then a continuous layer of Al_2O_3 will form. The critical solute concentration $N_{Al}^{*,establish}$

required to establish an external oxide scale derived from equation 2.20 is given by equation 2.21. g^* values are difficult to quantify but g^* values for most relevant oxides are near 0.3 [21].

$$N_{Al}^{*,establish} = \left[\frac{\pi g^*}{2v} N_O^{(S)} \frac{D_O V_m}{D_{Al} V_{ox}}\right] \tag{2.21}$$

If external Al_2O_3 is established, there must be a sufficient supply of Al to the scale-alloy interface to maintain the growth of the layer. Should it be too small, the activity of Al at the oxidation front will be too small to form Al_2O_3. This will result in scale breakdown and allow oxygen to penetrate into the alloy to cause internal oxidation. The critical concentration of Al for the maintenance of an external scale ($N_{Al}^{*,maintain}$) can be calculated by equating the flux of aluminum to the scale-alloy interface to the flux of Al required to maintain the growth of the oxide based on the oxidation kinetics of the scale (equation 2.22). A schematic diagram of the supply of Al to the scale-alloy interface is shown in Fig. 2.10. As indicated in this figure, an imposed limiting assumption is that the amount of Al in the alloy at the Al_2O_3-alloy interface is zero. This is not physically possible, but it simplifies the analysis.

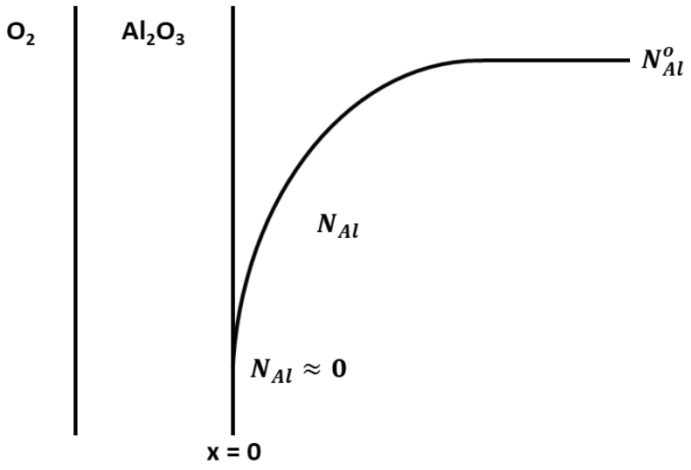

Figure 2-10. Diffusion of Al to the Al_2O_3-alloy interface [21].

$$J_{Al} = \frac{D_{Al}}{V_m}\left(\frac{\partial N_{Al}}{\partial x}\right)_{x=0} = \frac{1}{2v}\left(\frac{k_p^{1/2}}{M_O}t^{-1/2}\right) \tag{2.22}$$

The left side of this equation is the flux of Al to the scale-alloy interface and the right side of the equation is the flux of Al required to sustain the growth of the scale. By evaluating the concentration gradient at x = 0 (the scale-alloy interface), the critical $N_{Al}^{*,maintian}$ is given by equation 2.23 [36].

$$N_{Al}^{*,maintain} = \frac{V_m}{32v}\left(\frac{\pi k_p}{D_{Al}}\right)^{1/2} \tag{2.23}$$

In the case of Al_2O_3 formation on superalloy components during service, the critical concentration of aluminum ($N_{Al}^{*,establish}$ and $N_{Al}^{*,maintain}$) are difficult to predict because there are several environmental factors in addition to the composition of the alloy which affect the values.

Therefore, understanding how the composition of the alloy and the environment in which it operates affects the alloy's ability to form and maintain protective Al_2O_3 is necessary to explain how $CaSO_4$-induced degradation may lead to the internal oxidation observed in the field-exposed components.

2.2.3.1 Compositional Effects on The Boundary Between Internal and External Oxidation: The Third Element Effect

One of the critical aspects of this research project was determining how calcium-containing deposits such as CaO and $CaSO_4$ can result in breakaway internal oxidation in the 2nd generation single crystal superalloys studied in this thesis. Therefore, understanding how the composition of a nickel-based alloy affects N_{Al}^* will provide insight into how compositional changes caused by reaction with CaO and $CaSO_4$ deposits may affect the alloy's ability to form a protective scale.

There are currently only simplified models that predict N_{Al}^* in nickel-based alloys based on composition. This means that our knowledge of the influence of alloy composition on the transition between external and internal oxidation is mainly based on careful experimentation. The most well-regarded empirical results for this transition are those collected by Giggins and Pettit who recorded N_{Al}^* at 1000, 1100, and 1200°C over a wide range of compositions in the NiCrAl system. The results of these experiments at 1000 °C are presented as an "oxide map" in Fig. 2.11 [19]. Their results show that chromium can profoundly affect the transition between external and internal Al_2O_3 formation by significantly decreasing N_{Al}^*. This beneficial effect of chromium has been termed the "third element effect"

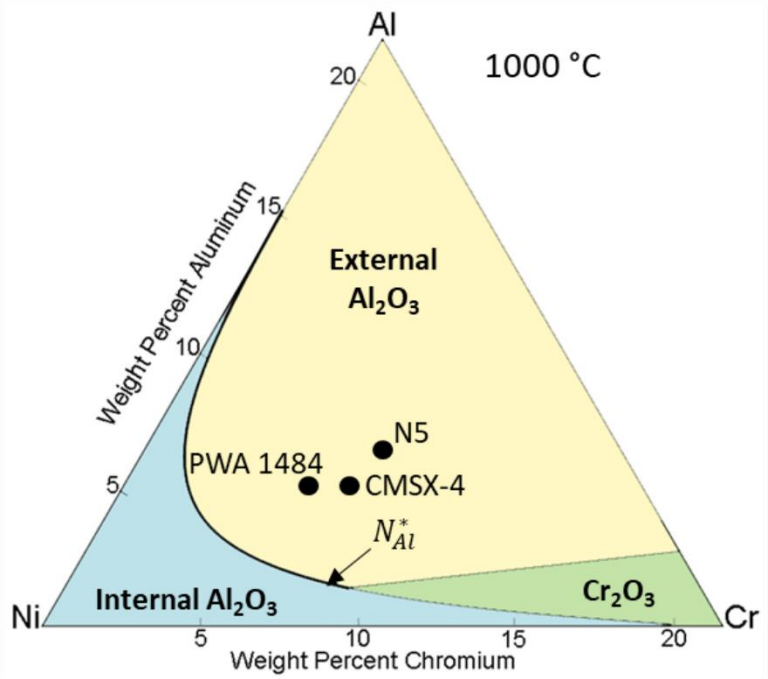

Figure 2-11. Oxide map predicting the oxidation behavior of NiCrAl alloys at 1000 °C. The composition of common 2nd generation nickel-based superalloys are superimposed on the diagram (Adapted from [19]).

The mechanism of this third element effect was first posed in the context of the Cu-Zn-Al system by Wagner to be a "gettering" effect [37]. According to this theory, and applying it to the Ni-Cr-Al system, the thermodynamic stability of Cr_2O_3 is intermediate to that of NiO and Al_2O_3, so that the initial establishment of a Cr_2O_3 scale (for kinetic reasons) would preclude further Ni oxidation but still permit Al oxidation. Moreover, the initially formed Cr_2O_3 scale would retard the dissolution and diffusion of oxygen into the alloy, which allows more time for aluminum to reach the oxidation front and form an Al_2O_3 scale. Some justification for this theory was that the formation of a Cr_2O_3 scale or subscale during the transient stages of oxidation was observed prior to the formation of an Al_2O_3 scale in Ni-15Cr-6Al [38]; however, there are deficiencies in this explanation for the effect of chromium on N_{Al}^* which have led to the theory falling out of favor. For example, the conditions for the gettering effect are met by adding manganese as a third element

with intermediate oxygen affinity to the Fe-Mn-Al and Ni-Mn-Al systems. If the gettering effect held true, the addition of manganese to the alloy would decrease N_{Al}^{*}; however, experiments have found that Mn has little or even a negative effect on the oxidation behavior of the alloys [39–41]. Alternative explanations for the third element effect propose that the beneficial effect of chromium is due to α-Cr_2O_3 acting as a "template" stabilize α-Al_2O_3 opposed to faster growing metastable phases of Al_2O_3. Additionally, there is evidence that chromium can increase the flux of aluminum to the oxidation front in the alloy.

Identifying the mechanisms for the template effect was the subject of research by Yihong Kang [41]. When aluminum oxidizes, initially it nucleates and grows as metastable Al_2O_3 phases such as γ or θ [42, 43]. These metastable Al_2O_3 phases grow faster than α-Al_2O_3 which means that a greater concentration of aluminum in the alloy is required to sustain the growth of metastable Al_2O_3. Several studies have found that the presence of Cr, Fe, or Ti in an alloy during oxidation accelerates the transformation of θ-Al_2O_3 to α-Al_2O_3 [44–46]. The mechanism behind the template effect is that the more rapid nucleation of oxides such as α-Cr_2O_3, α-Fe_2O_3, and α-Ti_2O_3 with the same rhombohedral corundum structure as α-Al_2O_3 will promote the transformation from metastable Al_2O_3 to the desired α-Al_2O_3.

Kang studied the oxidation behavior of Ni-8Al, Ni-8Al-6Cr, and Ni-8Al-6Mn (at%) in air at 1100°C during the early stages of oxidation. His results showed that, after 3 minutes of exposure, the Al_2O_3 precipitates in Ni-8Al were entirely γ-phase while much of Al_2O_3 precipitates formed in the Ni-8Al-6Cr alloy had transformed to α-phase. This can be seen in a phase map of the internal oxide precipitates presented in Fig. 2.12. EDS analysis of the oxide precipitates revealed significant chromium enrichment between the Al_2O_3 precipitates and the alloy matrix. This

suggests that the oxidation of aluminum occurs in the alloy followed shortly by the formation of α-Cr_2O_3 at the Al_2O_3-alloy interface which stabilizes α-Al_2O_3. This can be seen in Fig. 2.13.

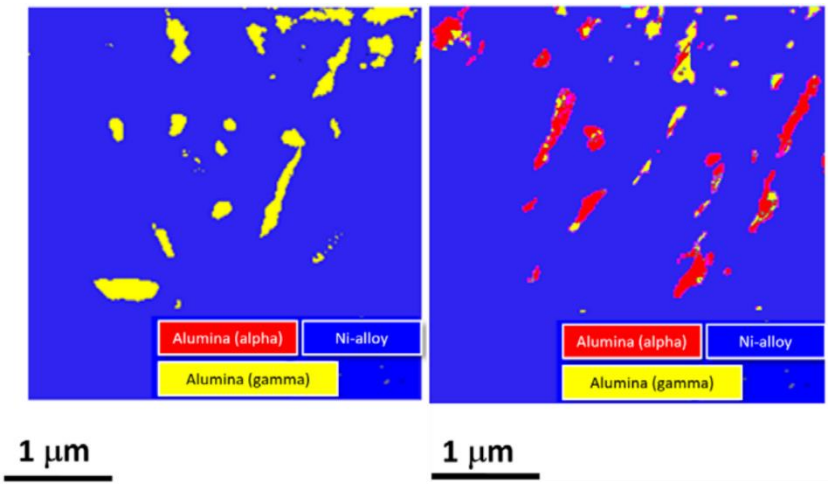

Figure 2-12. PED-TEM phase map of the internal oxidation zone in Ni-8Al (left) and Ni-8Al-6Cr (right) [41].

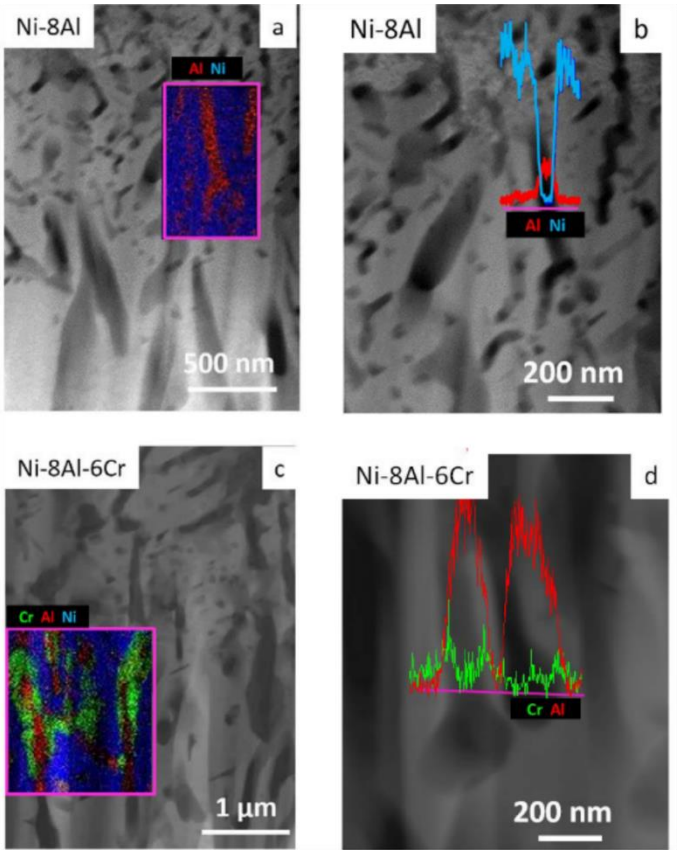

Figure 2-13. The composition of internal oxide precipitates in Ni-8Al and Ni-8Al-6Cr after a 3 minute exposure in dry air at 1100°C [41].

The accelerated transformation from γ-Al_2O_3 to α-Al_2O_3 was found to be beneficial in decreasing $N_{Al}^{*,establish}$ because of the influence that the Al_2O_3 crystal structure has on the morphology of the internal oxide precipitates. It was found that the difference in interfacial surface energy between γ-Al_2O_3 or α-Al_2O_3 and the alloy causes γ-Al_2O_3 precipitates to have a rod-like morphology and α-Al_2O_3 precipitates to have a plate-like morphology. Kang calculated that the coarse plate-like α-Al_2O_3 precipitates decrease the oxygen permeability (the product of oxygen solubility and diffusivity) in the alloy by decreasing the area of precipitate-alloy interface available to act as short-circuit diffusion paths for oxygen into the alloy. Decreasing the oxygen permeability would decrease $N_{Al}^{*,establish}$ through equation 2.21. This hypothesis is supported by calculations of

the oxygen permeability made from measurements of the internal oxidation depth in Ni-Al-Cr and Ni-Al-Mn alloys after a 4-hour exposure in dry air at 1100°C. The oxygen permeability decreases with increasing chromium content because chromium stabilizes plate-like α-Al_2O_3. The oxygen permeability increases with increasing manganese content because manganese stabilizes rod-like γ-Al_2O_3. This can be seen in Fig. 2.14.

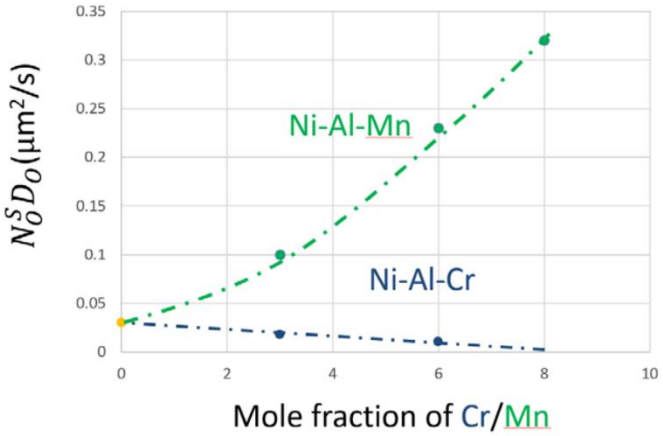

Figure 2-14. Effect of third element concentration on measured oxygen permeability in Ni-8Al [41].

In addition to the template effect of Cr, there is evidence that the presence of chromium in Al_2O_3-forming alloys such as Fe-Cr-Al boosts the concentration of aluminum at the surface of the alloy. This enrichment of aluminum at the surface is attributed to the addition of chromium increasing the chemical potential gradient that drives the diffusion of aluminum from the bulk alloy to the aluminum depleted sub-surface. This happens because the addition of chromium decreases the chemical potential of aluminum relative to that of iron in the sub-surface compared to a binary NiAl alloy [47–49] resulting in a steeper chemical potential gradient. This can be seen in Fig. 2.15.

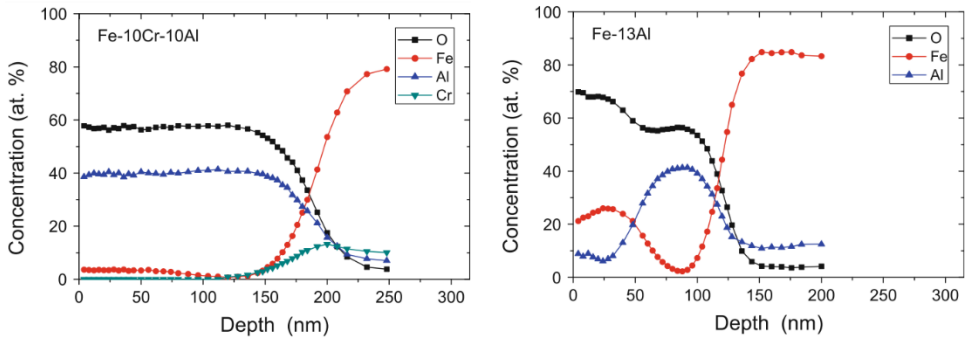

Figure 2-15. Concentration profiles versus depth measured after a 1 minute exposure in oxygen at 1000°C by Auger electron spectroscopy combined with plasma sputtering [47].

2.2.3.2 Influence of Temperature

The surface temperature that gas path components experience during service in the high-pressure turbine can vary between 600°C and 1200°C depending on the location of the part in the engine and the performance of the aircraft. Due to the dynamic thermal exposure conditions, it is important to understand the effect of exposure temperature on the transition between external and internal oxidation.

It is well established that $N_{Al}^{*,establish}$ and $N_{Al}^{*,maintain}$ are strongly linked to exposure temperature. Al_2O_3 scales form and are maintained more easily at high temperature [19, 50]. This is clearly shown in an oxide map generated for NiAl between 900°C and 1300°C in Fig. 2.16.

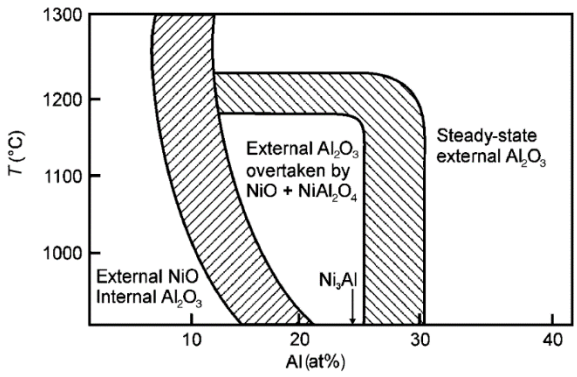

Figure 2-16. Effect of temperature on oxidation behavior of NiAl [50].

The influence of temperature on $N_{Al}^{*,establish}$ is linked to the thermally activated diffusion of oxygen and aluminum in nickel. In Fig. 2.16, the left-most boundary represents $N_{Al}^{*,establish}$ as predicted by equation 2.21 where it can be seen that, as $\frac{D_O}{D_{Al}}$ decreases, $N_{Al}^{*,establish}$ decreases. Due to a difference in the activation energy for the substitutional diffusion of aluminum and interstitial diffusion of oxygen in nickel (equations 2.24 [51] and 2.25 [52]), as temperature increases, $\frac{D_O}{D_{Al}}$ and, therefore, $N_{Al}^{*,establish}$ decreases.

$$D_{Al}\left(\frac{m^2}{s}\right) = 1.9x10^{-4}\exp\left(-\frac{265\,kJ/mol}{RT}\right) \tag{2.24}$$

$$D_{O}\left(\frac{m^2}{s}\right) = 4.9x10^{-6}\exp\left(-\frac{164\,kJ/mol}{RT}\right) \tag{2.25}$$

The influence of temperature on $N_{Al}^{*,maintain}$ is linked to the rate at which fast growing metastable Al_2O_3 phases transform to slow growing α-Al_2O_3. In Fig. 2.16, the knee-like region marks compositions at temperatures which can supply enough aluminum to establish an Al_2O_3

scale but not enough to maintain scale growth during longer exposure, *i.e.* $N_{Al}^{*,establish}$ is satisfied but $N_{Al}^{*,maintain}$ is not. This region exists because, at temperatures below ≈1200°C in Ni-Al, the transformation of metastable γ- and θ-Al_2O_3 to α-Al_2O_3 is slow and metastable alumina scales have much larger growth rates than α-Al_2O_3 (Fig. 2.17) [42, 43]. As described in equation 2.23, the growth rate of the oxide plays a significant role on $N_{Al}^{*,maintain}$ for the maintenance of the scale. Therefore, $N_{Al}^{*,maintain}$ decreases significantly at higher temperatures where the transformation from fast growing metastable Al_2O_3 to slow growing α-Al_2O_3 becomes more rapid.

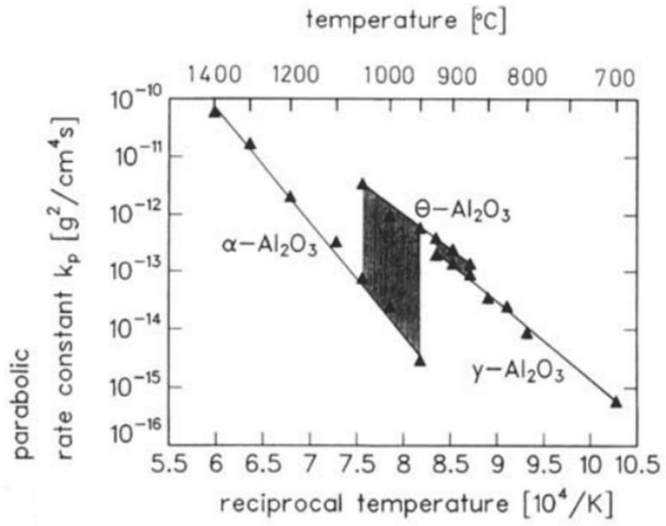

Figure 2-17. Parabolic rate constants for α-, γ-, and θ-Al_2O_3 [42].

2.2.3.3 Influence of Atmospheric Steam

Water vapor is present in the high-pressure turbine environment from the intake of water or humid air and from the high air-to-fuel ratio combustion process [53]. The presence of water vapor in the atmosphere has been shown to be detrimental to Al_2O_3 scale formation. It has been postulated that moisture in the atmosphere can result in hydrogen-induced embrittlement of the

scale-alloy interface in alloys with sulfur impurities [54]. The interstitial hydrogen released into the alloy by the dissociation of H_2O during exposure is attracted to the tensile stress state of the scale-alloy interface and, in the presence of sulfur, it embrittles the interface and may lead to scale spallation. Wet oxidizing environments have also been found to increase the $N_{Al}^{*,establish}$ in NiCrAl alloys. The results from Zhao et al. [55] are presented in Figs. 2.18 and 2.19.

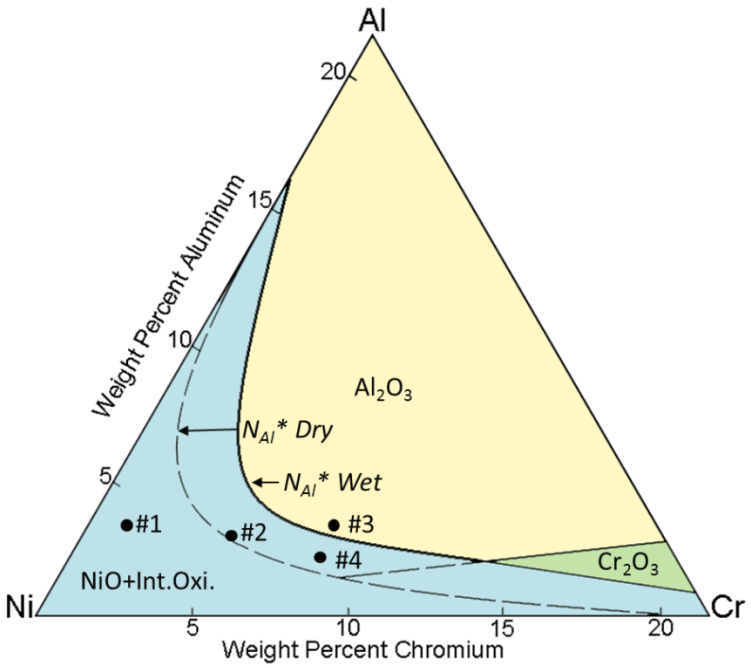

Figure 2-18. Effect of 30% water vapor on the boundary between internal and external Al_2O_3 formation during oxidation at 1000 °C in air. Corresponding cross-sectional SEM images are shown in Fig. 2.19 [55].

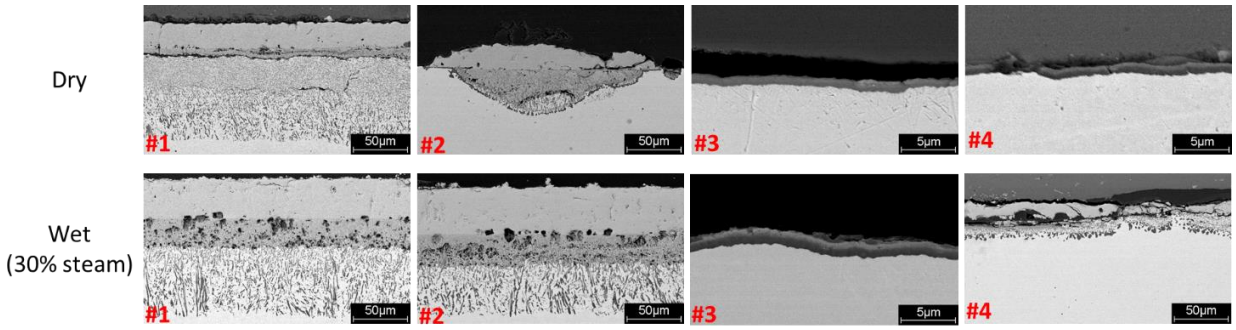

Figure 2-19. SEM micrographs of model NiCrAl alloys oxidized at 1000 °C in dry air or air + 30% steam [55].

The results of these experiments found that the value for $N_{Al}^{*,establish}$ increased by 60% in alloys oxidized in air with 30% water vapor compared to the alloys oxidized in dry air. To determine the mechanism by which atmospheric steam increases $N_{Al}^{*,establish}$, the author's considered the effect of steam on the variables in equation 2.21: v_{eff}, oxygen permeability ($D_O N_O^{(s)}$), D_{Al}, and g*.

v_{eff} can vary between 1.5 for Al_2O_3 and 2 for $NiAl_2O_4$ so any change in v_{eff} could not affect $N_{Al}^{*,establish}$ significantly enough to explain the 60% difference. Therefore, the change in the effective stoichiometry of the internal oxidation product cannot account for the increase in $N_{Al}^{*,establish}$. Recent work published on the effect of steam on oxygen permeability in Fe-Ni alloys determined that the presence of atmospheric steam has a negligible effect on the oxygen permeability which suggests steams effect on $N_{Al}^{*,establish}$ is not a result of changes in oxygen permeability [56]. Zhao et al. did not experimentally determine if steam has a significant effect on D_{Al} but did show that it would take an unreasonably large change in D_{Al} to account for the 60% change in $N_{Al}^{*,establish}$. Zhao et al. concluded that the critical volume fraction of Al_2O_3 precipitates, g*, is the variable that is affected by steam to increase the N_{Al}^{*} in wet atmospheres. They measured

that the volume fraction of internal Al_2O_3 was the same in the alloys tested in wet air and dry air, but that there were a smaller number of coarser, more widely spaced, oxide precipitates in the alloy tested in wet air. From this it was inferred that the extent of lateral growth for Al_2O_3 precipitates needed to form a continuous scale is much larger in wet air than in dry air. Therefore, in order to form a continuous scale in these conditions, a larger number of Al_2O_3 precipitates is required to establish an Al_2O_3 scale which requires a higher aluminum content. The reason that steam affects the morphology of internal alumina precipitates is still unknown. Zhao et al. [55] proposed that hydrogen enters the alloy and acts as a component which affects the thermodynamic driving forces for the nucleation and growth of internal Al_2O_3 precipitates.

2.3 State of the Art for Deposit-Induced Corrosion in the Aviation Industry

2.3.1 Na_2SO_4-Induced Hot Corrosion

In addition to atmospheric and environmental factors that are detrimental to an alloy's ability to form and maintain a protective Al_2O_3 scale, more aggressive modes of degradation caused by corrosive deposits can breakdown protective scales and lead to accelerated oxidation and sulfidation attack. The current understanding of deposit-induced degradation in aero-applications is largely based on investigations into degradation caused by molten sulfate deposits. This attack is called hot corrosion [8]. Hot corrosion is the process by which thermally-grown oxides are dissolved and fluxed into a liquid sulfate mixture (typically assumed to be Na_2SO_4) by acidic or basic reactions. When the component surface is first wetted by a molten sulfate salt, the

acidity or basicity of the sulfate melt can be given by the following reaction where SO_3 is defined as the acidic component and Na_2O as the basic component (equation 2.26).

$$Na_2SO_4 = SO_3 + Na_2O \tag{2.26}$$

The acidity/basicity of the melt dictates the mode of oxide dissolution and the solubility of the oxides in the melt. It is affected by interactions between the deposit, alloy, and atmosphere. Rapp compiled data on solubilities of several technically important oxides in liquid Na_2SO_4 at 900°C as a function of the basicity of the melt. These solubility curves are shown in Fig. 2.20 [57].

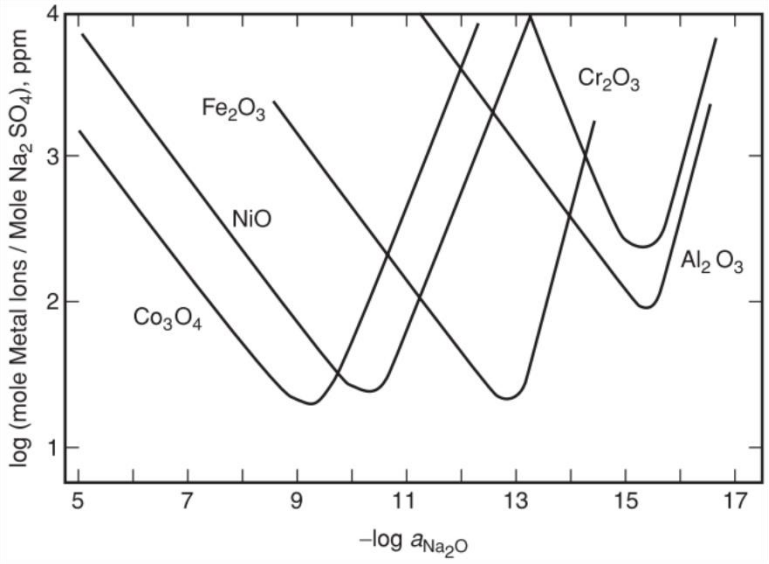

Figure 2-20. Solubilities of several oxides in Na_2SO_4 at 900 °C. Figure is from [21] and data is from [57–63].

Hot corrosion is typically separated into two distinct mechanisms, called Type I and Type II corrosion, based on the exposure temperature and SO_3 content in the atmosphere [64]. Type I hot corrosion occurs through basic dissolution of the oxide in liquid Na_2SO_4 at temperatures above

the melting point of Na_2SO_4 (T_m = 884°C). Type II hot corrosion occurs when liquid Na_2SO_4 formation is stabilized below the melting point of Na_2SO_4 by SO_3 in the atmosphere. The temperature range where hot corrosion is a concern is between 700 °C and the dew point of the sodium sulfate, which is the temperature at which the liquid sulfate begins to volatilize rapidly. This dew point depends on the thermodynamic equilibrium in the high pressure turbine environment and the deposit composition, but is generally around 1000 °C for pure Na_2SO_4 deposits [65].

Conventional Type I Na_2SO_4-induced hot corrosion occurs by basic dissolution and associated fluxing of protective oxide into the liquid deposit where it reprecipitates as a porous non-protective oxide. Basic dissolution occurs when Na_2O activity in the molten sulfate is sufficiently high. Using an NiO scale formed on Ni as an example, high basicity is established through the following steps. During the initial stages of Type I hot corrosion, the equilibrium oxygen potential established by the SO_3 component of the sulfate melt (from equation 2.27) is sufficient to form NiO at the alloy-sulfate interface.

$$SO_3 = SO_2 + \frac{1}{2}O_2 \tag{2.27}$$

The consumption of oxygen to form NiO results in a decrease in P_{O_2} at the alloy-sulfate interface which results in a corresponding increase in P_{SO_2}. The increase in P_{SO_2} near the sulfate-alloy interface increases the sulfidizing potential near the interface and NiS_x begins to form. The removal of both oxygen and sulfur from the molten sulfate at the alloy-sulfate interface decreases the P_{SO_3} locally which results in a relative increase in the a_{Na_2O} near the alloy sulfate interface. This basic Na_2O reacts with the thermally grown oxides to form species that are soluble in the

melt. In nickel-based alloys, NiO is susceptible to hot corrosion attack by forming NiO_2^{2-} through basic dissolution via the following reaction.

$$NiO + Na_2O = 2Na^+ + NiO_2^{2-} \tag{2.28}$$

Rapp and Goto [66] determined that this fluxing reaction is able to proceed because the solubility gradient of the dissolved species in the melt is negative through the thickness of the sulfate melt. Because this criterion is met, NiO_2^{2-} released by basic dissolution at the oxide-sulfate interface will diffuse away from the oxide-sulfate interface driven by the NiO_2^{2-} gradient and precipitate as non-protective oxides. Should the solubility gradient vanish, the sulfate melt will become saturated at the oxide-sulfate interface and no further oxide dissolution will occur. A schematic of this process is shown in Fig. 2.21.

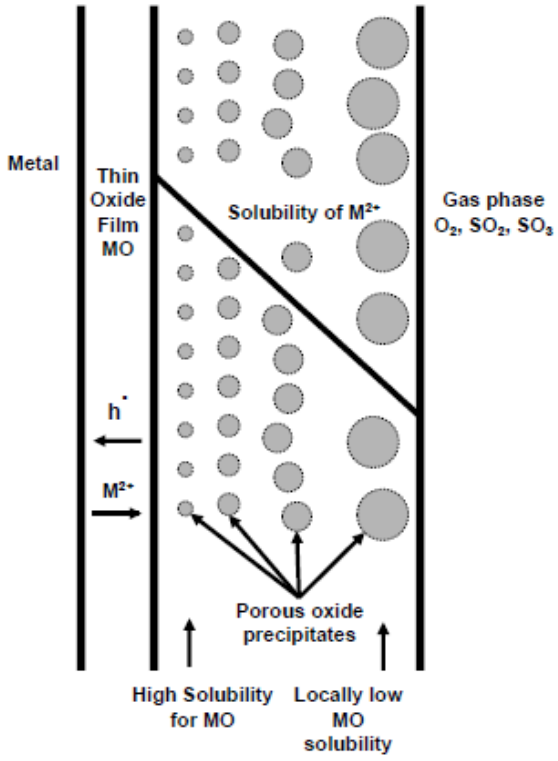

Figure 2-21. Fluxing and precipitation of thermally grown oxides in molten Na_2SO_4 with a negative solubility gradient [8].

Type II hot corrosion occurs below the melting point of Na_2SO_4 when SO_3 in the atmosphere is high. A recent review and assessment of Type II hot corrosion of Ni in 1000 ppm $SO_2 + O_2$ was presented by Gheno et al. [67]. The authors proposed that NiO reacts with SO_3 to form $NiSO_4$. Because $NiSO_4$ is soluble in Na_2SO_4, increasing the $NiSO_4$ content in the sulfate solution decreases the temperature of first liquid formation (the $NiSO_4$-Na_2SO_4 eutectic temperature is 671 °C). The liquid sulfate penetrates the NiO scale which allows SO_3 to enter the alloy to cause sulfidation. When nickel is sulfidized, an interconnected sulfide network forms within the oxide and allows the fast transport of metal, oxygen, and sulfur ions throughout the corrosion product resulting in accelerated oxidation-sulfidation. It should be noted that this form of attack is not self-sustaining. After longer exposure periods, the consumption of SO_3 in the melt

by the oxidation-sulfidation of nickel will decrease the P_{SO_3} in the sulfate solution. This results in a decrease in the solubility of NiO in the solution and destabilizes liquid phase. When the liquid becomes unstable, porous NiO will precipitate and further dissolution will not occur. This process is shown in Fig. 2.22.

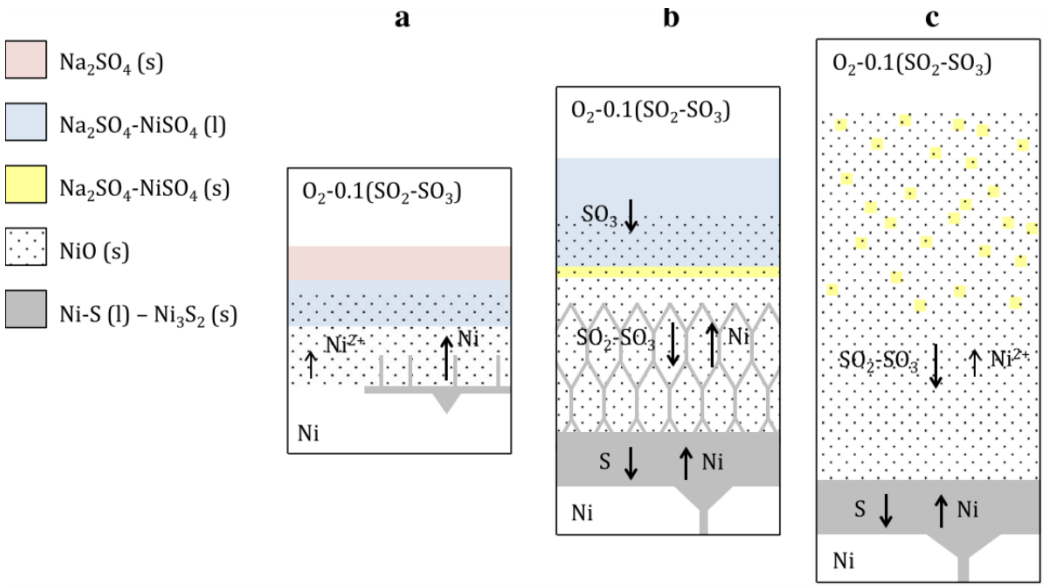

Figure 2-22. Schematic representation of the type II hot corrosion process for Ni [67].

While attack induced by Na_2SO_4 deposits is a significant concern to the service life of high pressure turbine components, little effort has been made to determine if the other alkali sulfates commonly found on high pressure turbine components such as K_2SO_4, $MgSO_4$, and $CaSO_4$ [68] cause other modes of degradation. Of particular interest are $CaSO_4$ deposits. The degradation of high-pressure turbine components with deposits rich in $CaSO_4$ was the impetus for this research and has been reported previously [7, 69]. However, interactions between alumina-forming nickel-based alloys and calcium-containing deposits are less understood than those for Na_2SO_4.

2.3.2 Degradation Caused by Calcium-Containing Deposits

The thermodynamic stability between CaO and $CaSO_4$ plays an important role in the possible modes of calcium-rich deposit-induced degradation. The stability of a calcium-containing deposit can be expected to toggle between CaO and $CaSO_4$ in the dynamic environment of the high-pressure turbine. Because of this, both CaO- and $CaSO_4$-induced modes of degradation must be considered and reviewed. The stability between CaO and $CaSO_4$ in a low P_{SO_2} oxidizing environment representative of a high-pressure turbine [10] is shown in Fig. 2.23.

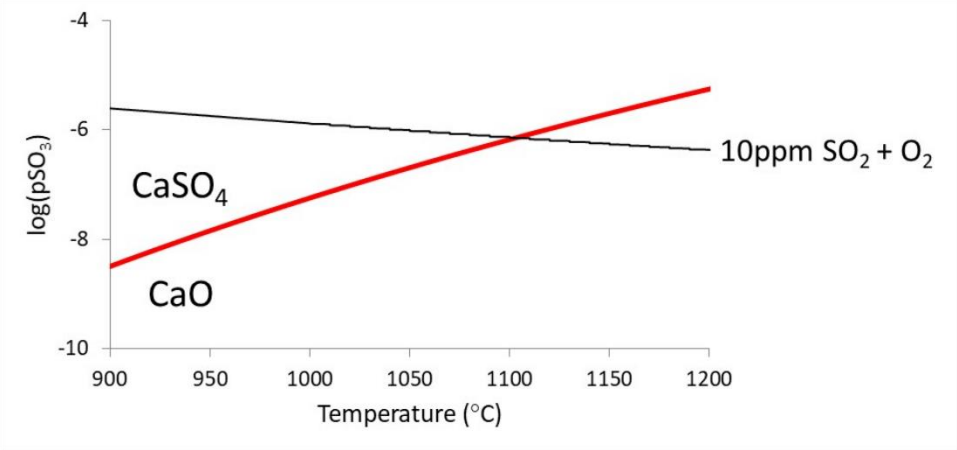

Figure 2-23. Thermodynamic stability of $CaSO_4$-CaO in 10 ppm SO_2 + O_2. Thermodynamic data taken from [70]

It should be noted that the melting points of CaO and $CaSO_4$ (2572°C and 1460°C respectively) are much higher than the temperature that components are exposed to during service. Therefore, the modes of calcium-containing deposit-induced degradation are likely to take place through solid-state reactions.

While explanations for CaO- or $CaSO_4$-induced degradation in aero-engines have not been reported, modes of calcium-rich deposit-induced degradation have been proposed to explain

accelerated oxidation and sulfidation observed in in-bed heat exchangers for the fluidized bed combustion of coal and other applications in power generation [12, 13, 71–73]. The mechanisms of CaO and $CaSO_4$-induced degradation from these works can be used to gain insight into the modes of degradation that may be taking place in gas-turbine engines.

2.3.2.1 CaO-Induced Degradation

An early investigation into CaO-induced attack in oxidizing environments was conducted by Chiang et al. [14] who studied the oxidation behavior of Cr_2O_3-forming alloys with CaO deposits in oxygen at temperatures between 850°C and 1050°C. Their work showed that, at elevated temperatures, CaO deposits are not stable in contact with thermally grown Cr_2O_3. Reaction between CaO and Cr_2O_3 occurred to form non-protective calcium chromates (Ca_xCr_yO). The authors discovered that CaO-induced degradation on Cr_2O_3-forming alloys was particularly aggressive at 1050°C due to the formation of a liquid Ca_xCr_yO phase.

Gheno et al. [72] and Jung [73] were among the first to study the mechanisms of CaO-induced degradation of Al_2O_3-forming alloys. Both found that CaO deposits are not stable in contact with Al_2O_3. During high temperature exposure, CaO and Al_2O_3 react to form non-protective calcium aluminates. In the cement literature, calcium aluminates are an important constituent in cement, calcium aluminates named and defined as $xCaO + yAl_2O_3 = C_xA_y$. Pseudo binary phase diagrams for the CaO-Cr_2O_3 and CaO-Al_2O_3 systems show that the possible stoichiometries of calcium chromate and aluminate phases that may form by reaction between CaO and Cr_2O_3 and Al_2O_3 (Fig. 2.24).

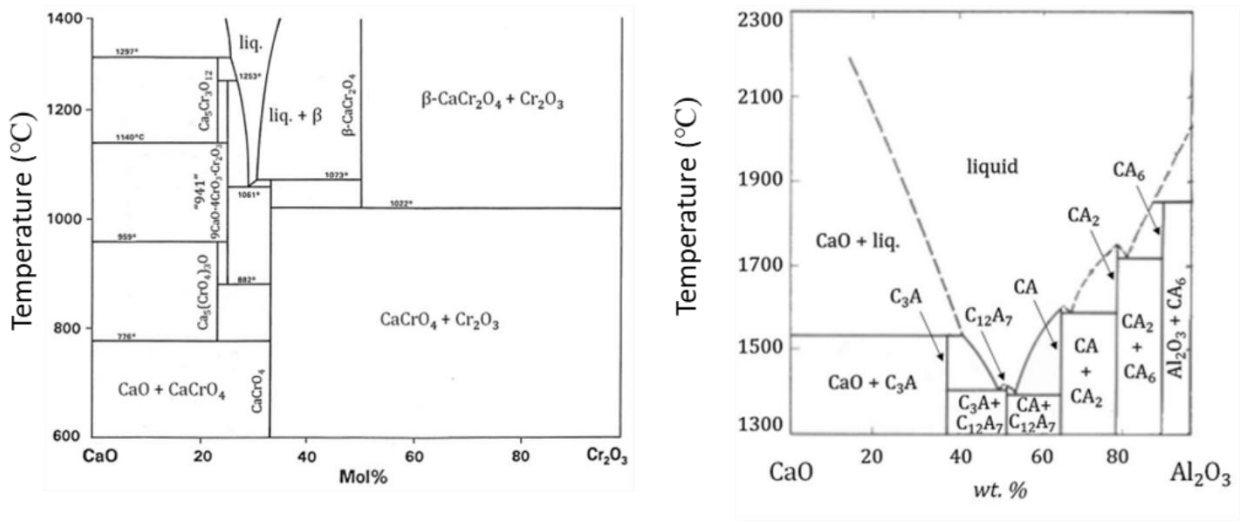

Figure 2-24. $CaO\text{-}Cr_2O_3$ (left) and $CaO\text{-}Al_2O_3$ (right) phase [74, 75].

Gheno et al. characterized in greater detail how CaO deposits react with different Al_2O_3-forming NiCoCrAlY compositions at elevated temperatures. Circular coupons with a diameter of 1 cm were exposed with 35 $\frac{mg}{cm^2}$ of CaO at 1100°C for 50 hours. All alloys formed an external product that consisted of a thin Al_2O_3 layer at the scale-alloy interface below a thicker layer of multi-phase C_xA_y. The C_xA_y region was identified to be primarily made of $CaAl_2O_7$ and $CaAl_2O_4$ with the Al-rich $CaAl_4O_7$ being present closer to the Al_2O_3 scale and the $CaAl_2O_4$ being closer to the CaO. The high-Cr alloy studied (Ni-30Co-33Cr-12Al-0.1Y) exhibited a larger extent of degradation compared to the high-Al alloy (Ni-20Co-16Cr-23Al-0.1Y) due to the formation of liquid (at 1100°C) Ca_xCr_yO above the Ca_xAl_yO layer. The presence of an external Ca_xCr_yO layer on the Cr-rich alloys suggests that the deposit reacted with the Cr-rich transient oxidation product on the alloy prior to the establishment of an exclusive Al_2O_3 scale. This was proven when the Cr-rich alloy was oxidized for 10 hours with no CaO deposit then re-exposed for 40 hours with CaO deposit. In this experiment, the CaO reacted with the thermally grown Al_2O_3 to form calcium

aluminates but no calcium chromate was formed. Images of Al- and Cr-rich alloys after exposure are shown in Fig. 2.25.

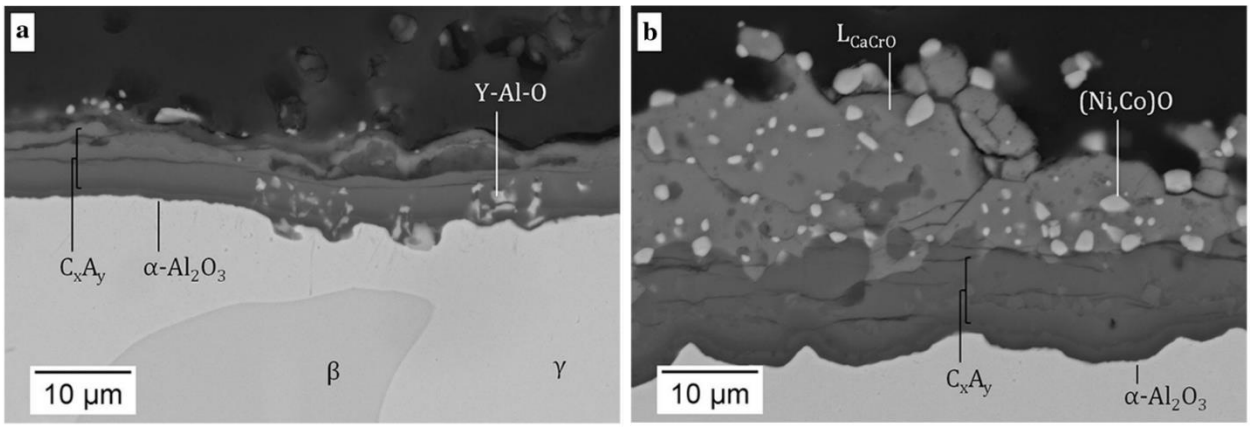

Figure 2-25. Reaction product formed on Ni-20Co-16Cr-23Al-0.1Y (left) and Ni-30Co-33Cr-12Al-0.1Y (right) after 50 hours of exposure at 1100°C with 35 $\frac{mg}{cm^2}$ of CaO [72].

The authors determined that rapid formation of the non-protective C_xA_y thins the protective Al_2O_3 scale. Because the C_xA_y layer is an ineffective diffusion barrier, oxygen is able to transport relatively quickly through thin Al_2O_3 scale. Using this information, the authors developed a kinetic model for the oxidation rate of an Al_2O_3-forming alloy with CaO deposit based on the model for multi-layered oxide scale growth proposed by Yurek et al. [76]. Figure 2.26 is a schematic from [72] that shows the reaction product formed on Al_2O_3-forming NiCrAlY with CaO deposit at 1100°C with a description of the reactions, transport, and kinetics for the process.

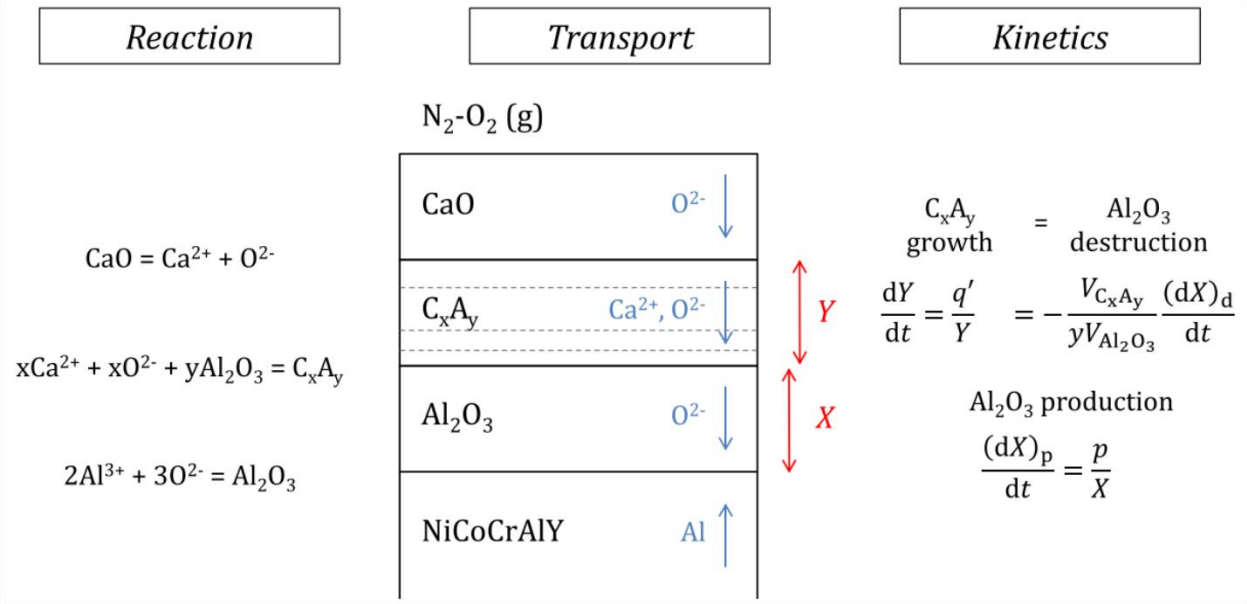

Figure 2-26. Schematic diagram explaining the development of the Al_2O_3 + Ca_xAl_y O reaction product during CaO-induced degradation [72].

The growth of the C_xA_y layer is controlled by the diffusion of Ca^{2+} through C_xA_y [77–80] to the Al_2O_3-Ca_xAl_yO interface where the following reaction takes place.

$$xCa^{2+} + xO^{2-} + yAl_2O_3 = C_xA_y \tag{2.29}$$

The growth of the Al_2O_3 layer is dictated by two processes. The first is the destruction of Al_2O_3 to form C_xA_y by equation 2.29 and the second is its generation by oxidation of aluminum at the Al_2O_3-alloy interface. The authors described the multi-phase calcium aluminate layers as a single layer of average stoichiometry C_xA_y because the stoichiometry and thickness of the individual calcium aluminates do not affect the oxygen flux used for the oxidation reaction. Because the growth of the C_xA_y layer is limited by diffusion, its thickening kinetics are parabolic

and described by equations 2.30 and 2.31 where Y is the thickness of the C_xA_y layer and q' is the apparent parabolic rate constant for C_xA_y layer growth.

$$\frac{dY}{dt} = \frac{q'}{Y} \tag{2.30}$$

$$Y^2 = 2q't \tag{2.31}$$

The thickening rate of the Al_2O_3 scale is the sum of the Al_2O_3 destruction rate at the Al_2O_3-C_xA_y interface and the Al_2O_3 production rate at the Al_2O_3-alloy interface. The rate of destruction can be derived from the mass balance in equation 2.29 and is given by equation 2.32 where V_i is the molar volume of phase "i". The rate of Al_2O_3 production is given in equation 2.33 and relies on the assumption that the growth mechanism of Al_2O_3 at the Al_2O_3-alloy interface is unaffected by reaction with CaO. In equation 2.33, X is the thickness of the Al_2O_3 layer and p is the intrinsic parabolic rate constant for Al_2O_3 growth.

$$\frac{(dX)_d}{dt} = -\frac{yV_{Al_2O_3}}{V_{C_xA_y}}\frac{dY}{dt} \tag{2.32}$$

$$\frac{(dX)_p}{dt} = \frac{p}{X} \tag{2.33}$$

Adding equations 2.32 and 2.33 yields the net Al_2O_3 growth rate given in equation 2.34.

$$\frac{dX}{dt} = \frac{p}{X} - \frac{yV_{Al_2O_3}}{V_{C_xA_y}}\frac{dY}{dt} \tag{2.34}$$

Substituting equations 2.30 and 2.31 into equation 2.34 and defining $\alpha = \frac{yV_{Al_2O_3}}{V_{C_xA_y}}$ will yield equation 2.35 which can be solved to yield equations 2.36 and 2.37 where p' is the apparent rate constant for the growth of the Al_2O_3 layer considering the destruction of Al_2O_3 at the C_xA_y-Al_2O_3 interface.

$$\frac{dX}{dt} = \frac{p}{X} - \alpha\frac{q'}{\sqrt{2q't}} \tag{2.35}$$

$$X^2 = 2p't \tag{2.36}$$

$$p' = \frac{1}{2}\left[2p + \alpha^2 q' - \alpha\sqrt{q'(4p + \alpha^2 q')}\right] \tag{2.37}$$

The relationship between p and p' and q and q' are the general equations given by Yurek et al. [76] presented in equations 2.38 and 2.39. It follows that the ratio of layer thickness is given by equation 2.40.

$$p' = \frac{p}{1 + \alpha\frac{Y}{X}} \tag{2.38}$$

$$q' = \frac{q}{1 + \frac{1}{\alpha}\frac{X}{Y}} \tag{2.39}$$

$$\frac{Y}{X} = \alpha \frac{q}{p} \tag{2.40}$$

When the authors used the measurements from their experiments to compare to what would be predicted by their model, they found that the p' obtained from their measurements was roughly 6 times smaller than that predicted by the model. The difference could not be attributed to any experimental error and was therefore attributed to limitations in the assumptions made for the analysis. However, their analysis is still useful as it provides a semi-quantitative model that explains the effect of CaO-induced degradation on the rate of aluminum consumption. Because the Al_2O_3 is thinned by reaction to form C_xA_y, it is a less effective diffusion barrier. Substituting equation 2.36 into equation 2.33 yields equation 2.41: the rate of Al_2O_3 production as a function of p, the normal growth rate of Al_2O_3, and p', the apparent growth rate of Al_2O_3 considering destruction to form C_xA_y.

$$\frac{(dX)_p}{dt} = \frac{p}{\sqrt{2p't}} \tag{2.41}$$

Because $p' < p$, the rate of aluminum consumption from the alloy is larger with CaO than the alloy oxidized without CaO whose Al_2O_3 production rate is given by equation 2.42.

$$\frac{(dX)_p}{dt} = \frac{p}{\sqrt{2pt}} \tag{2.42}$$

The influence of increased Al consumption on the bulk concentration of aluminum in the alloy required to maintain an Al_2O_3 scale was considered by the authors who used the results from their model and Wagner's analysis for $N_{Al}^{*,maintain}$ to predict $N_{Al}^{*,maintain}$ for an Al_2O_3-forming alloy with and without CaO-induced degradation. The resulting chart is presented here as Fig. 2.27.

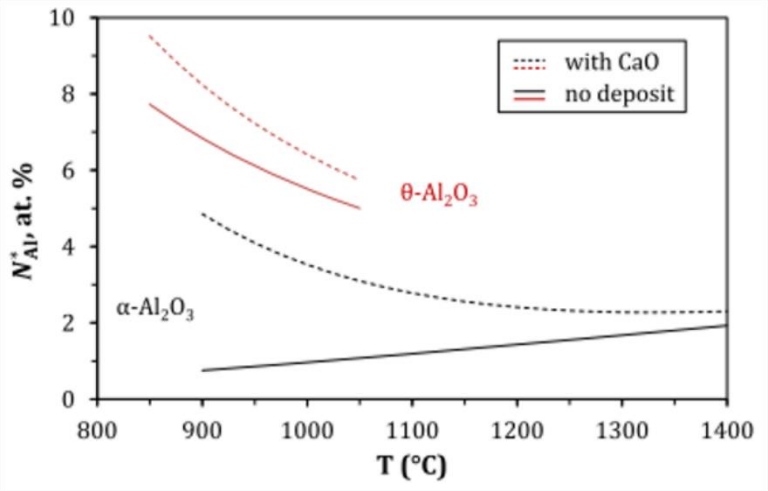

Figure 2-27. Minimum bulk aluminum concentration required to maintain external Al_2O_3 growth with and without CaO reaction as a function of temperature [72].

2.3.2.2 $CaSO_4$-Induced Degradation

Due to a smaller body of completed research, there is much less known about mechanisms of $CaSO_4$-induced degradation at high temperatures and nearly all of the research examines attack of Cr_2O_3 forming Fe- and Ni-based alloys used for heat exchangers in the fluidized bed combustion (FBC) of coal. The prevailing explanation provided for the degradation was that it was caused

when a dense layer of $CaSO_4$ deposited on a heat exchanger and, according to the interpretation provided by Stringer and Minchener [12], the SO_2 potential (P_{SO_2}) at the deposit-alloy interface dropped below that for $CaSO_4$-CaO equilibrium. The $CaSO_4$ consequently decomposed locally at the deposit-alloy interface to form CaO and release SO_3. The authors calculated that the equilibrium P_{S_2} established by $CaSO_4$ decomposition would be sufficiently high to form sulfides of nickel and chromium. This resulted in the formation of internal nickel and chromium sulfides beneath the protective Cr_2O_3 layer that eventually prevented the maintenance of the Cr_2O_3 scale and lead to extensive degradation of the alloy by oxidation and sulfidation.

The release of sulfur from a $CaSO_4$ deposit acting as the initiator for corrosion is a promising starting point for studying Ca-rich deposit-induced internal oxidation observed in the field exposed components of interest. However, the mode of degradation under these conditions are likely different from that described by Stringer and Minchener. There are two key differences between the FBC environment and the gas-turbine environment. The first is that the P_{S_2} in the FBC environment is much higher than that of the turbine environment due to a much higher level of sulfur impurities in coal as opposed to jet fuel. The second difference is that the maximum exposure temperature of the components of interest in the FBC is 900°C [81] while it is 1200°C for the high-pressure turbine components. Possible reaction mechanisms for $CaSO_4$-induced degradation in high-pressure turbine environments based on thermodynamic calculations are put forward in the following paragraphs.

Thermodynamic calculations of the stability of CaO-$CaSO_4$ deposits and the thermally grown oxides formed on 2nd generation superalloys reveal two possible modes of degradation in the HPT environment. One possible degradation mechanism was proposed by Chiang et al. [14]. In their research, the authors conducted an experiment where they deposited $CaSO_4$ on a Cr_2O_3

forming alloy exposed at 900°C in O_2. They observed that the $CaSO_4$ deposit did not significantly affect Cr_2O_3 scale growth at 900°C. However, they believed that $CaSO_4$-induced degradation of Cr_2O_3 and, potentially, Al_2O_3 forming alloys could occur at higher temperatures where the thermal decomposition of $CaSO_4$ to form CaO and release SO_3 was more rapid. In this mechanism, the thermal decomposition of $CaSO_4$ could cause corrosion through reactions 2.43 and 2.44 for an Al_2O_3 forming alloy.

$$CaSO_4 \rightarrow CaO + SO_3 \tag{2.43}$$

$$CaO + Al_2O_3 \rightarrow CaAl_2O_4 \tag{2.44}$$

The CaO formed by decomposition would react with the thermally grown Al_2O_3 scale to form non-protective calcium aluminates and the released SO_3 would establish a sulfur potential high enough to form nickel and chromium sulfides. Thermodynamic calculations of the stability of $CaSO_4$-CaO in a 10 ppm SO_2 + O_2 atmosphere representative of the atmosphere of the high pressure turbine [10] (seen previously in Fig. 2.23) show that the thermal decomposition temperature of $CaSO_4$ in this environment is ≈1100°C. However literature concerning the thermal decomposition kinetics of $CaSO_4$ reveal that the decomposition is quite sluggish at temperatures below 1200°C [82, 83].

Similar calculations show that the second mechanism to consider for $CaSO_4$-induced degradation is direct interaction between $CaSO_4$ and Al_2O_3 via the reaction in equation 2.45.

$$CaSO_4 + Al_2O_3 \rightarrow CaAl_2O_4 + SO_3 \tag{2.45}$$

In this case, $CaSO_4$ would react directly with the thermally grown Al_2O_3 scale to form non-protective calcium aluminates and release SO_3. Thermodynamic calculations of the stability of $CaSO_4$ in contact with Al_2O_3 in a 10 ppm $SO_2 + O_2$ atmosphere show that the reaction in equation 2.45 is possible at temperatures above ≈950°C (Fig. 2.28).

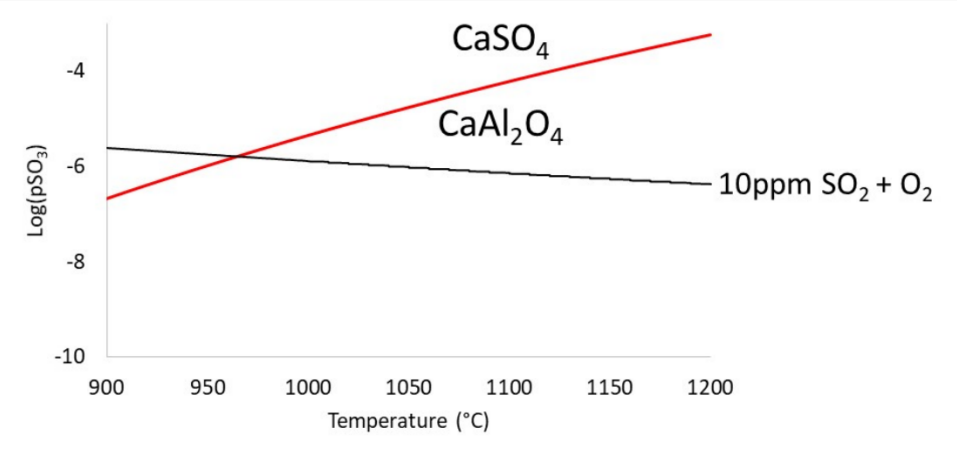

Figure 2-28. Thermodynamic stability of $CaSO_4$ in contact with Al_2O_3 in 10 ppm $SO_2 + O_2$. Thermodynamic data taken from [70].

3.0 Deficiencies in the Current Body of Knowledge and Research Objectives

The preceding review of the literature on deposit-induced degradation of nickel-based superalloys reveals that the majority of the research has been dedicated to describing corrosion caused by molten Na_2SO_4-rich deposits. While that work has led to an extensive understanding of corrosion caused by molten sulfates, the same principles cannot be applied to degradation caused by calcium-rich deposits. Therefore, it has become necessary to identify the conditions where degradation caused by calcium-rich deposits becomes severe and to elucidate the mechanisms by which the degradation occurs.

The goal of this research project was to provide the foundational understanding of CaO- and $CaSO_4$-induced degradation in aviation gas-turbine engines and to develop a lab-scale test procedure which accurately replicates the degradation observed in field-exposed components. Developing such an understanding will lay the groundwork for future mitigation strategies and aid in the alloy development process by providing a novel test procedure which can be used to better evaluate and rank alloy performance. In this study, special attention was paid to characterizing the nature of breakaway internal oxidation caused by $CaSO_4$ deposits and determining how $CaSO_4$-alloy interactions induce changes in the alloy composition and microstructure that make it susceptible to internal oxidation.

Chapter 5 presents SEM and TEM analysis that details the morphology of the degradation observed in field-exposed components. Emphasis is placed on characterizing the composition and phase distribution in the internal oxidation zone. Chapter 6 presents the results of isothermal experiments conducted to investigate the interactions that take place between CaO or $CaSO_4$ deposits and 2nd generation superalloys at elevated temperatures. This was achieved by exposing

Rene N5 and N500 coupons with CaO or $CaSO_4$ deposits at 900°C or 1150°C in air for various times and characterizing the reaction product. Chapter 7 presents the thought process and principles used to develop the bi-thermal test procedure which successfully replicated the degradation that occurs in the field-exposed components. Discussion is focused on explaining how subsurface depletion of Al and Cr and enrichment of S caused by $CaSO_4$-induced degradation can sensitize a superalloy to breakaway internal oxidation. Chapter 8 details how the environmental variables of thermal profile and deposit mass influence the oxidation behavior of a subsurface-depleted alloy and how the oxidation behavior is closely linked to the kinetic competition between internal and external oxidation in the subsurface-depleted alloys. Chapter 9 examines how the severity of $CaSO_4$-induced degradation varies with alloy composition. Observations from the field-exposed components and from the results of the lab-scale experiments have shown that N5 is more resistant to $CaSO_4$-induced degradation than N500. The influence of alloy composition on the oxidation resistance of nickel-based alloys was explored by conducting $CaSO_4$-induced degradation experiments on a model superalloy with composition intermediate to that of N5 and N500. Additionally, the internal oxidation behavior of model Ni-Cr-Al-Re alloys was studied at 1000°C. Finally, the thesis ends with a summary of the key research findings and suggestions for future work that should be done to further investigate deposit-induced internal oxidation.

4.0 Experimental Procedures and Set-Up

Most of the experiments for this thesis were done by exposing coupons of the 2nd generation single-crystal nickel-based superalloys N5 and N500 with CaO or $CaSO_4$ deposit in a horizontal tube furnace. The nominal compositions of N5 and N500 are presented in Table 4.1. Rectangular coupons of the alloys (25 × 12.5 × 3 mm) were received from GE Aviation in the as-cast condition and prepared for furnace testing by grinding the flat surfaces of the coupons to a P1200-grit finish using SiC paper. The ground coupons were then degreased by ultrasonic cleaning in ethanol.

Table 4-1. Nominal composition of Rene N5 and Rene N500 (at%).

At%	Ni	Cr	Co	Al	Mo	W	Ta	Re	Hf	Y
N5	Bal.	8.1	7.7	13.8	0.9	1.6	2.2	1.0	0.05	0.01
N500	Bal.	6.9	7.6	13.9	0.9	2.0	2.1	-	0.05	0.03

Prior to furnace testing, either CaO or $CaSO_4$ was applied to the largest face of the clean coupons by wetting that face with 200 proof ethanol and emplacing the desired mass of deposit into the ethanol bead. 99.9% purity CaO and 99% purity $CaSO_4$-anhydrous powders were used. The ethanol-powder mixture was then spread evenly over the coupon surface and the coupons were heated on a hot plate set at 150°C to evaporate ethanol and any moisture absorbed by the deposit. The coupon was then weighed using an analytical balance. With this procedure an accurate deposit mass to ± 0.01 mg was measured.

Furnace testing was done in a controlled atmosphere and the target temperature was maintained in the 10 cm hot zone within ± 5°C. The work tubes used were 99.8% aluminum oxide with an inner diameter of 4.45 cm. Experiments were conducted using either bottled air or bottled

air + steam. The air used for the experiments was 99.999% purity. The inlet gas was flowed through the furnace tube at a rate of 50 $\frac{mL}{min}$. The gas outlet led into a Na_2CO_3-saturated water bath to remove and SO_2/SO_3, if present, from the exiting gas before being directed into a fume hood. For the steam tests, 30% steam was the target content in the atmosphere for the experiments. According to steam tables published in reference [84], the temperature of water in equilibrium with air + 30% steam is 70°C. 30% steam was added to the inlet gas by bubbling bottled air was through deionized water heated to 72°C. Above this bubbler was a condenser kept at 70°C using flowing heated water from a separate bath to condense excess water vapor in the gas before entering the furnace. A schematic of the overall experimental set-up is shown in Fig. 4.1. Samples were inserted and removed from the furnace while maintaining the controlled atmosphere by using a custom-made assembly. The samples were placed into an Al_2O_3 crucible which was suspended from an Al_2O_3 rod with Kanthal A1 wire. The rod had a magnet tied at its end and fitted into an enclosed extension of the Pyrex endcap. The endcap mated with a gas-tight steel adapter that fit over the end of the furnace tube. The mate was sealed with high-temperature vacuum grease and affixed via springs. The samples were moved into and out of the furnace using the magnet at the end of the guide rod. Figure 4.2 shows a picture of this set-up.

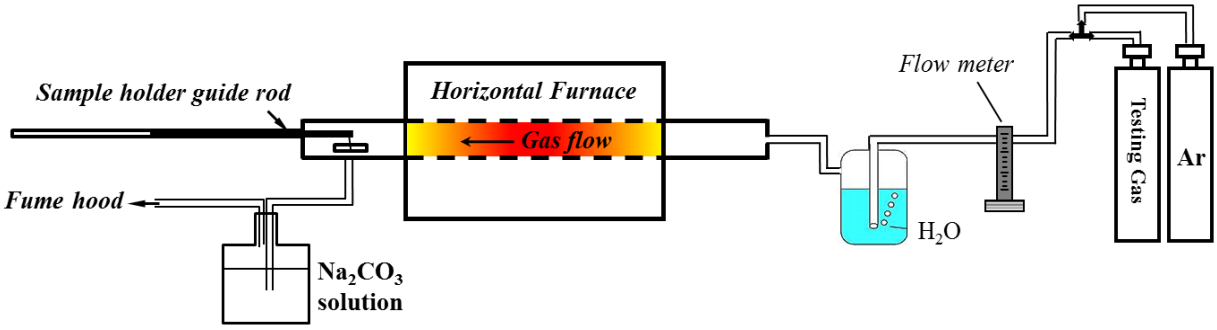

Figure 4-1. Schematic of the furnace set up.

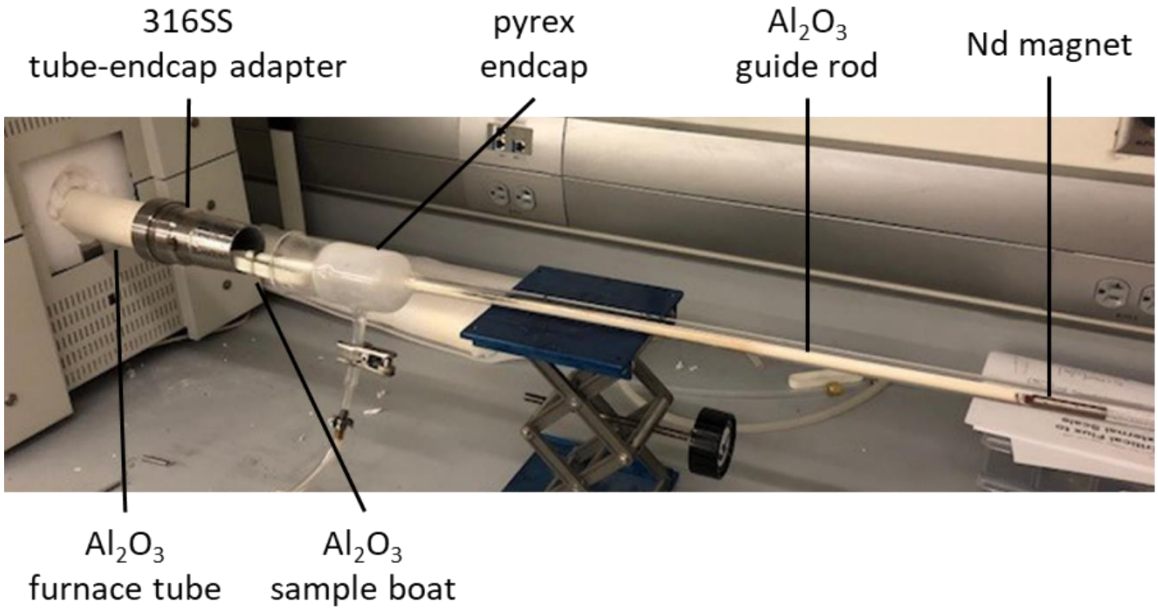

Figure 4-2. Set-up for the sample insertion and removal procedure.

All coupons were characterized after exposure by cross-sectional imaging using electron microscopy techniques. Samples mounted in epoxy resin were prepared for microscopy by cross-sectioning with an oil-lubricated saw and polishing with oil or alcohol-based solutions to retain any water-soluble corrosion products. Most coupons were cross-sectioned twice prior to grinding and polishing to ensure that three unique cross-sections could be characterized. Mounted cross-

sections were prepared by standard metallographic grinding and polishing techniques to a 0.25 μm finish. The samples were then cleaned in ethanol and coated with a thin film of palladium before electron microscopy.

The composition and make-up of the reaction products formed on N5 and N500 were found to be complex so most phase identification was made through interpreting semi-quantitative EDS analysis while considering the thermodynamic stability of relevant species. For scanning electron microscopy, an accelerating voltage of 20 kV was used when characterizing alloy coupons and 10 kV was used when characterizing the bulk Al_2O_3-$CaSO_4$ diffusion couples. X-Ray diffraction with a copper source was used in addition to EDS analysis to characterize the reaction product formed in the $CaSO_4$-Al_2O_3 diffusion couples. Additionally, bright-field and STEM transmission electron microscopy imaging using 200 kV accelerating voltage was done to characterize in greater detail the morphology and assemblage of the internal oxidation product in the field-exposed components. TEM samples were prepared by using focused ion beam milling to lift a thin sample for examination from the areas of interest in the mounted component cross-sections.

5.0 Characterization of Degradation Morphology Observed in Field Exposed Components

Three N500 and two N5 components suspected to have been attacked by calcium-rich deposits were provided by GE Aviation for characterization. While we cannot report the area of operation and duration of service for these parts, we can say that they are similar for all five components. Fig. 5.1 presents low magnification optical microscopy images of cross-sections from each component which had extensive degradation. The images revealed that the extent of degradation was greater in the N500 components (#1-#3) than in the N5 components (#4 and #5). The maximum total thickness of the external and internal degradation product exceeded 800 μm for all three N500 components and largest attack depth was 2200 μm for component #3. The maximum thickness for the degradation product in the N5 components was 367 μm for component #4. Remnant deposit was found on components #1 and #5 during SEM imaging and EDS analysis measured the deposit to be greater than 90% $CaSO_4$ with the remainder being $MgSO_4$ or MgO. Further SEM and TEM characterization of the components was done to gather more detailed analysis of the assemblage of the corrosion products.

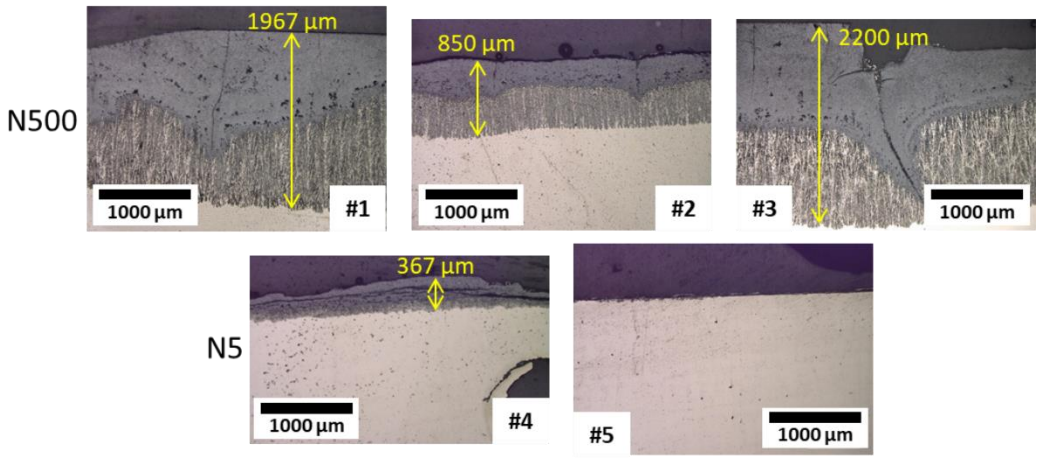

Figure 5-1. Cross-sectional optical images of field-exposed components. Components #1-3 are N500 and components #4 and #5 are N5.

Cross-sectional SEM micrographs of the reaction product from N500 components #1, #2, and #3 are presented in Fig. 5.2. The assemblage of the reaction product is similar for all three components. The degradation consists of an internal oxidation zone beneath an external Ni-rich oxide scale. The IOZ consists of "dendrite-like" intrusions of coarse Al- and Cr-rich oxide precipitates and the entire external layer of Ni-rich oxide is intermixed with what appear to be precipitates rich in Al and Cr. This suggests that the external product was once part of the internal oxidation zone that had eventually fully oxidized. A fine distribution of CrS precipitates is present in the γ' denuded zone ahead of the internal oxidation front in components #1 and #3 but is absent in component #2.

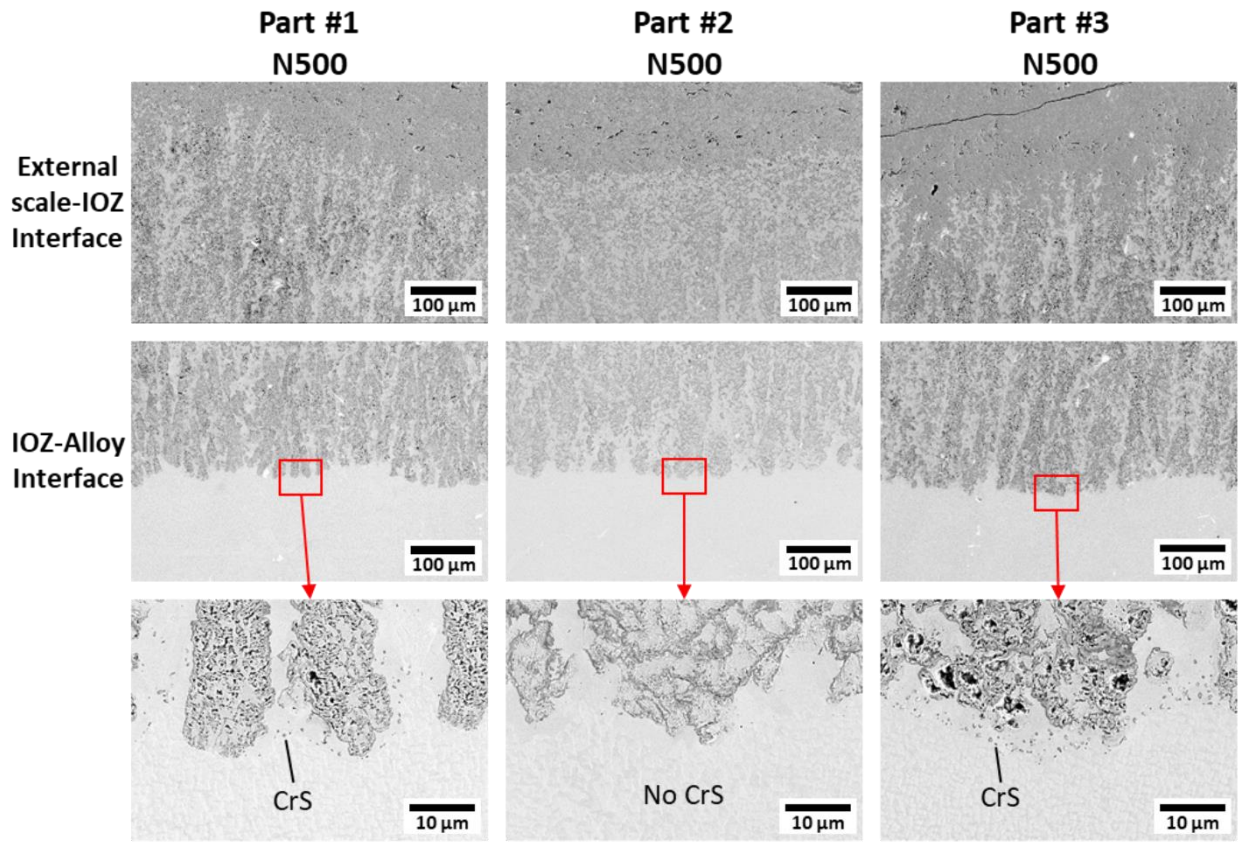

Figure 5-2. Cross-sectional SEM micrographs of components #1, #2, and #3. The top row of images shows the interface between the external NiO and the internal oxidation zone, the middle row of images shows the internal oxidation front and the bottom row shows high magnification images of the internal oxidation front.

Cross-sectional SEM micrographs of the reaction product from N5 components #4 and #5 are shown in Fig. 5.3. The assemblage of the reaction product in component #4 is similar, though less severe, to that observed in the N500 components. There is an external layer of Ni-rich oxide intermixed with Al- and Cr-rich oxide above an internal oxidation zone with coarse and irregular Al- and Cr-rich internal oxide precipitates. In component #5, the attack is much less severe. The external oxide product was found to be rich in Al, Cr, and Ni, which indicates $Ni(Al, Cr)_2O_4$ spinel formation. EDS analysis also detected 1-2 at% calcium in the external product which suggests that there is some reaction that takes place between the calcium-rich deposit and the thermally grown

oxides. In localized areas across the alloy surface, internal Al_2O_3 precipitates formed. A fine distribution of CrS precipitates is present in the γ'-denuded zone ahead of the oxidation front in component #5 but is absent in component #4.

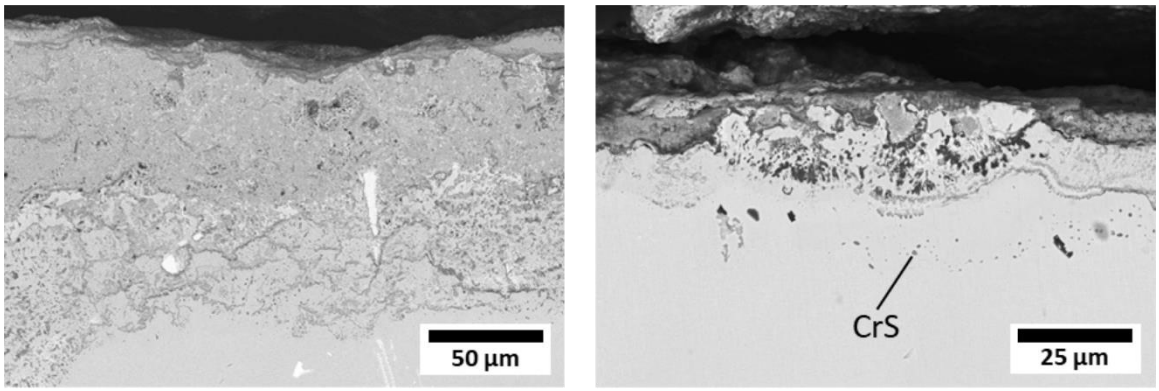

Figure 5-3. SEM micrographs of corrosion product formed on the N5 components #4 (left) and #5 (right).

The nature of the degradation product raises questions regarding the initiation and propagation of the internal oxidation process and the role that sulfur enrichment in the alloy subsurface may play. The make-up of the internal oxide product and extent of sulfur enrichment was determined through SEM and TEM analysis of samples prepared by FIB lift-outs from locations in component #2.

5.1 Make-Up of Internal Oxide Product

The make-up of the internal oxide product was characterized at the base of the IOZ (near the interface between the IOZ and the external Ni-rich scale) and at the internal oxidation front. The location of the sample lifted from the base of the IOZ is shown in Fig. 5.4 and the area analyzed

by EDS is shown in Fig. 5.5. The base of the IOZ is comprised of γ-Ni that is highly depleted of solute elements and a mix of several oxides. EDS analysis shows the main oxide products to be NiO and $NiAl_2O_4$ spinel. Additionally, Ta_2O_5 was present mixed with the $NiAl_2O_4$ and WO_3 particles had formed at Ni-NiO interfaces. The location of the sample lifted from the internal oxidation front is shown in Fig. 5.6 and the area analyzed by EDS is shown in Fig. 5.7. EDS analysis identified Al_2O_3, Cr_2O_3, Ta_2O_5 and γ-Ni islands. NiO and WO_3 were not observed near the internal oxidation front.

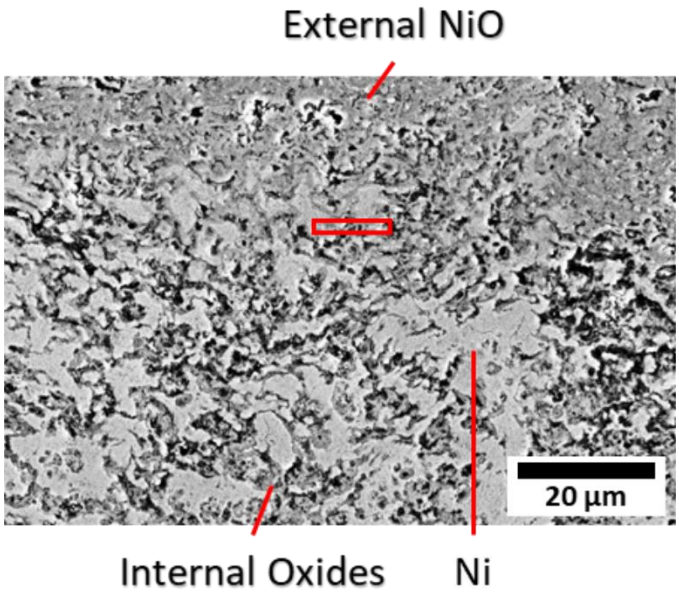

Figure 5-4. SEM image marking the location where the FIB lift-out was taken near the base of the IOZ (red box).

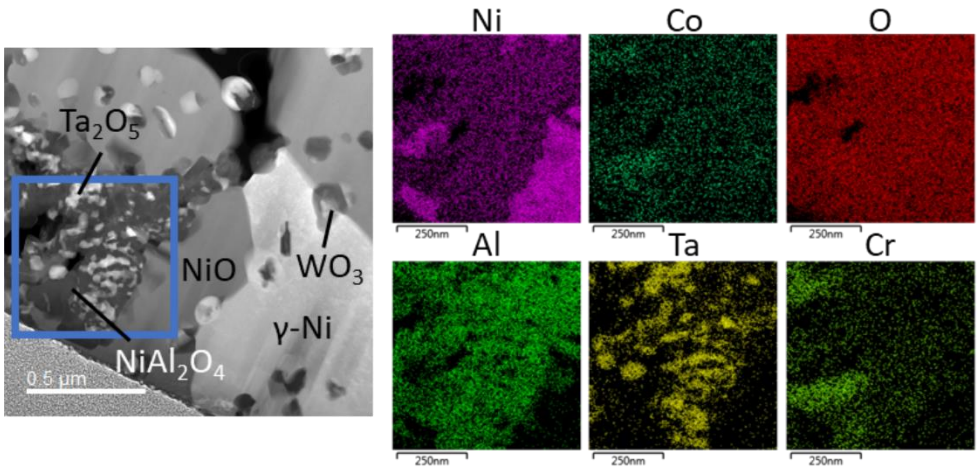

Figure 5-5. High magnification of an area near the base of the IOZ. EDS mapping was done in the blue box.

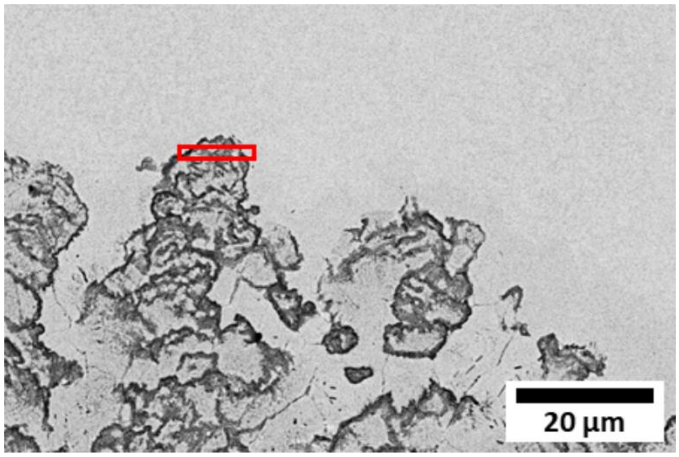

Figure 5-6. SEM image marking the location where the FIB lift-out was taken near the internal oxidation front (red box).

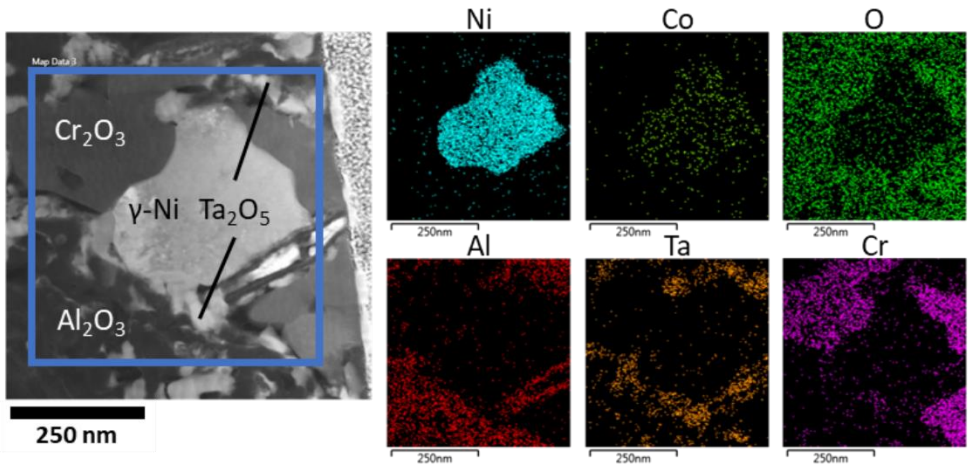

Figure 5-7. High magnification of an area near the internal oxidation front. EDS mapping was done in the blue box.

The make-up of the internal oxidation product as a function of depth in the IOZ is consistent with what would be expected for internal oxidation of N5 and N500 based on the relative thermodynamic stability of the oxides in the alloy presented in Fig. 5.8. This phase constitution is also consistent with what is observed for oxidation of dilute Ni-Al alloys [35].

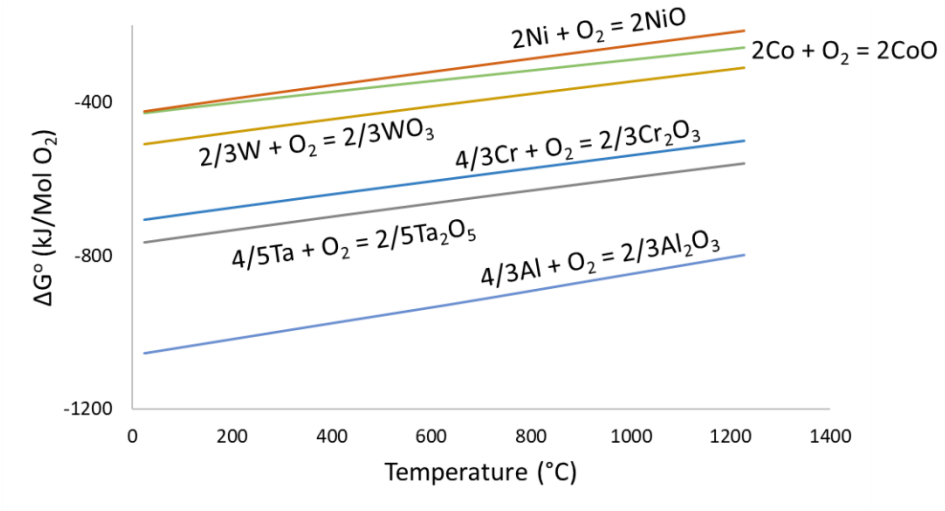

Figure 5-8. Relative stability of relevant oxide phases. Thermodynamic data from [70]

Near the internal oxidation front, the P_{O_2} is relatively low and only sufficient to form Al_2O_3, Ta_2O_5, and Cr_2O_3. Near the base of the internal oxidation front, the P_{O_2} is higher and sufficient to form WO_3, NiO and $Ni(Al, Cr)_2O_4$ spinel.

5.2 Presence of Sulfur Near the Internal Oxidation Front

The N500 components 1-3 all exhibited a very similar morphology of internal oxidation, but only components 1 and 3 had a fine distribution of CrS particles ahead of the internal oxidation product. The absence of CrS particles ahead of the internal oxidation front in component #2 raised questions about the role sulfur plays in the internal oxidation process. EELS analysis was done to determine if sulfur was present in the γ'-denuded zone ahead of the internal oxidation front in component #2. Micrographs of the area examined and the results of the EELS analysis from line scans 1 (γ-Ni) and 2 (Al_2O_3) are shown in Fig. 5.9. EELS show that there is no sulfur present in

the oxide precipitates but that there is indeed sulfur in solution in the γ-Ni at the internal oxidation front. Thus, though sulfur is present, it is ostensibly at a level that is insufficient to stabilize CrS formation at least in the region analyzed.

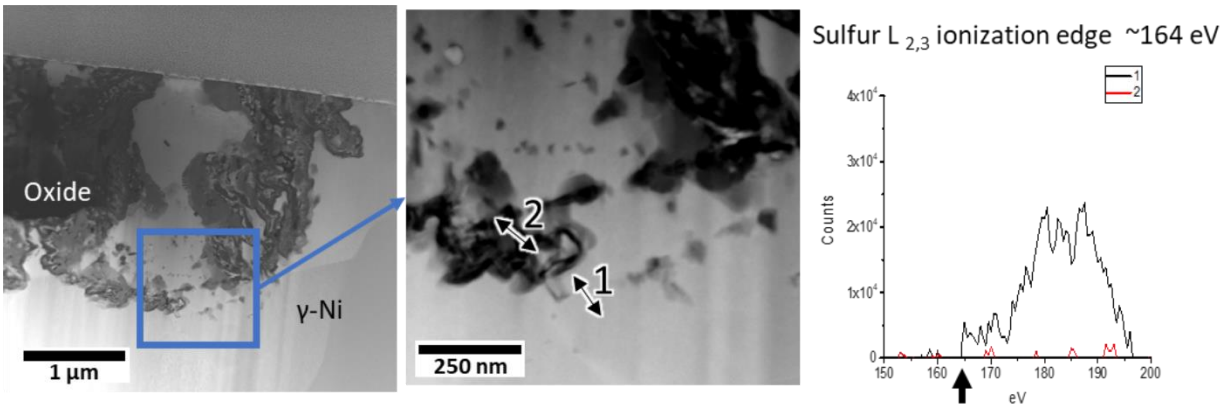

Figure 5-9. EELS analysis detects sulfur in the γ'-denuded zone ahead of the internal oxidation front.

5.3 Conclusions

The assemblage of the degradation morphology found in field-exposed components was found to have three characteristic features. The first is an external Ni-rich oxide layer, the second is an internal oxidation zone of coarse and irregular Al- and Cr-rich oxide precipitates, and the third is the enrichment of sulfur at the internal oxidation front which often manifests as CrS precipitates. The morphology is quite similar to the typical internal oxidation morphology expected from the internal oxidation of aluminum in a nickel alloy in a high P_{O_2} environment.

The results of the field-exposed component characterization informed our decision to study how exposure environment, alloy composition, and subsurface sulfur enrichment in combination

with calcium-containing deposit-induced degradation can lead to internal oxidation in nickel-based superalloys. To determine how calcium-rich deposits might cause such degradation in aero-engines components, the interactions that take place between CaO and $CaSO_4$ deposits and alloys N5 and N500 at 900°C and 1150°C were studied. The results of this work are presented in chapter 6.

6.0 Describing Interactions Between Single-Crystal 2nd Generation Superalloys and CaO or $CaSO_4$ Deposits in Oxidizing Environments

6.1 Experimental Procedure

The interactions between single-crystal 2nd generation superalloys and calcium-rich deposits were investigated by exposing coupons of Rene N5 and N500 with CaO or $CaSO_4$ deposits. CaO-alloy interactions at 900°C and 1150°C were assessed by exposing coupons with $2.5 \pm 0.5 \frac{mg}{cm^2}$ of CaO for 100 hours at 900°C or for 24 hours at 1150°C. $CaSO_4$-alloy interactions were investigated by exposing coupons with $20 \pm 1 \frac{mg}{cm^2}$ of $CaSO_4$ for 100 hours at 900°C or for 0.5, 1, 8, or 24 hours at 1150°C. The temperatures for the exposure were chosen as an approximation of the temperatures that components would experience during the takeoff (1150°C) and cruise (900°C) stages of a flight. All coupons were characterized after exposure by cross-sectional imaging using electron microscopy and EDS analysis. Mounted cross-sections were prepared by standard metallographic techniques.

6.2 Results and Discussion

6.2.1 CaO-Alloy Interactions

Figure 6.1 presents representative cross-sectional images of the reaction product formed on N5 and N500 with $2.5 \pm 0.5 \frac{mg}{cm^2}$ of CaO for 100 h at 900°C and 24 h at 1150°C in air. The

alloys exposed at 900°C formed an adherent mixed oxide and calcium aluminate reaction product. Al_2O_3 was the primary phase formed at the scale-alloy interface and the bulk of the external reaction product consisted of mixed Ni, Co, Al, Cr oxides and bands of calcium aluminate. The outer portion of the product consisted of calcium chromate with embedded particles of (Ni, Co)O. Local areas where limited internal oxidation of aluminum occurred were present in both N5 and N500, though they were more common in N500. For the alloys exposed at 1150°C, a thin layer of Al_2O_3 was present at the scale-alloy interface, with thicker layers of calcium aluminates above. The assemblage of the Al_2O_3-C_xA_y layers matched the reaction product that was reported to form on Al_2O_3-forming NiCrAlY alloys by Gheno et al. [72]. The C_xA_y region consisted primarily of two phases of calcium aluminate; an innermost $CaAl_4O_7$ layer and an outermost $CaAl_2O_4$ layer. EDS measurements of the C_xA_y layers from the cross-section of alloy N5 are shown in Fig. 6.2. The remainder of the product consisted of dense (Ni, Co)O surrounding darker islands of calcium aluminate. No calcium chromate was observed in the CaO-induced reaction product formed at 1150°C.

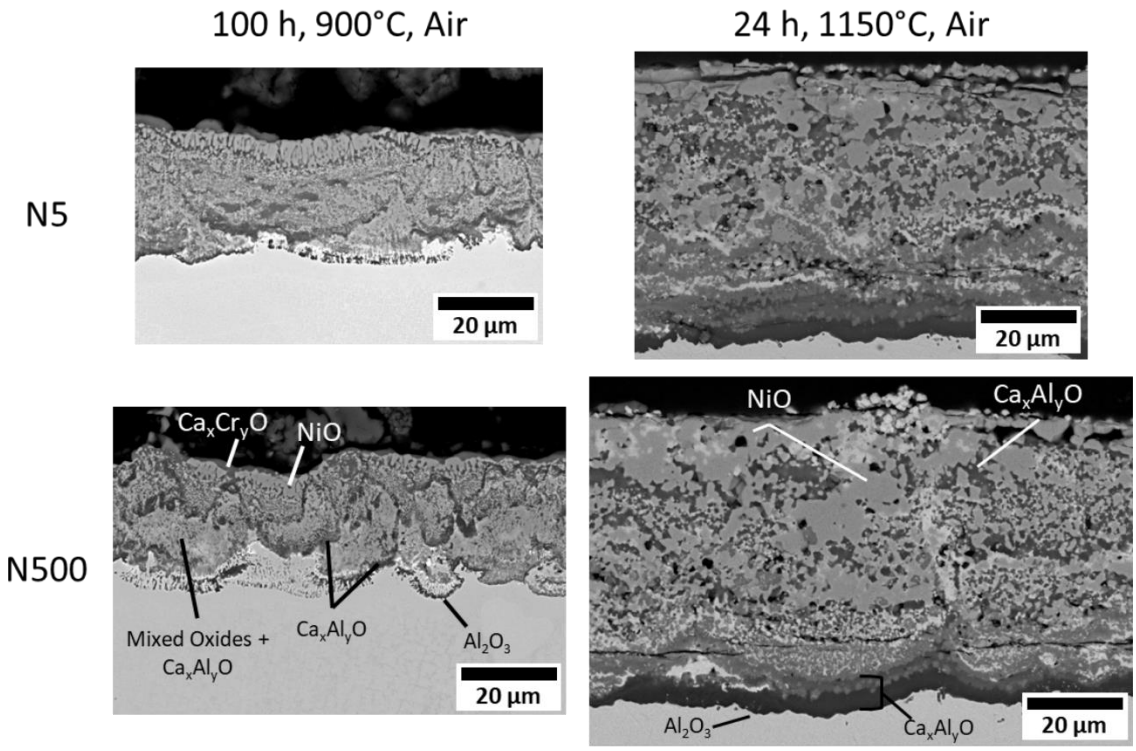

Figure 6-1. Reaction product formed on N5 and N500 with CaO deposit after 100 h at 900°C and 24 h at 1150°C.

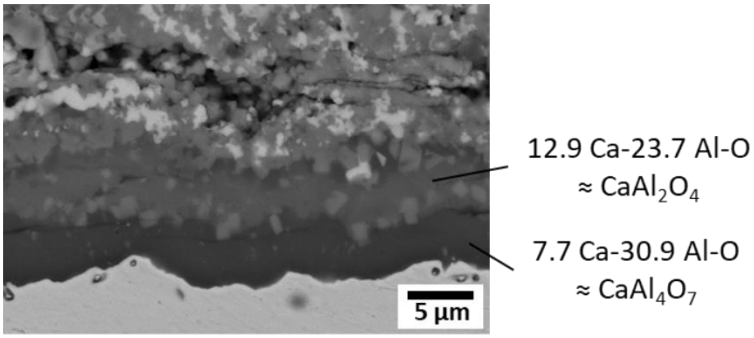

Figure 6-2. EDS measurements of the Ca_xAl_yO from the N5 coupon exposed at 1150°C for 24 hours.

The mode CaO-induced degradation observed in these experiments is consistent with previously published results [72, 73, 85]. CaO deposits cause accelerated oxidation by reacting with Al_2O_3 and Cr_2O_3 during the transient stages of exposure to form non-protective calcium aluminates and calcium chromates. The failure to establish a protective oxide scale results in the broad-front oxidation of the alloy. Calcium and oxygen continue to diffuse through the reaction product where it reacts with Al_2O_3 to produce layers of calcium aluminate.

While internal oxidation did occur locally in the coupons exposed at 900°C, broad-front breakaway internal oxidation similar to the attack observed in the field-exposed components was not observed in the present experiments nor has it been reported in the relevant literature. This suggests that, while CaO-alloy interactions can cause accelerated oxidation at high temperatures, the breakaway internal attack observed in field-exposed components is not likely to be caused by CaO deposits.

6.2.2 $CaSO_4$-Alloy Interactions

A cross-sectional image of the reaction product formed on N5 and N500 exposed with 20 ± 1 $\frac{mg}{cm^2}$ of $CaSO_4$ deposit for 100 h at 900°C in air is shown in Fig. 6.3. Both alloys formed a continuous Al_2O_3-based scale; however, EDS measurements of the scale detected small amounts of calcium. This suggests that there is limited interaction between the thermally grown Al_2O_3 and the deposit. The lack of degradation at 900°C is attributed to this temperature being too low for significant interaction between the deposit and Al_2O_3 to take place due to low reaction kinetics [14].

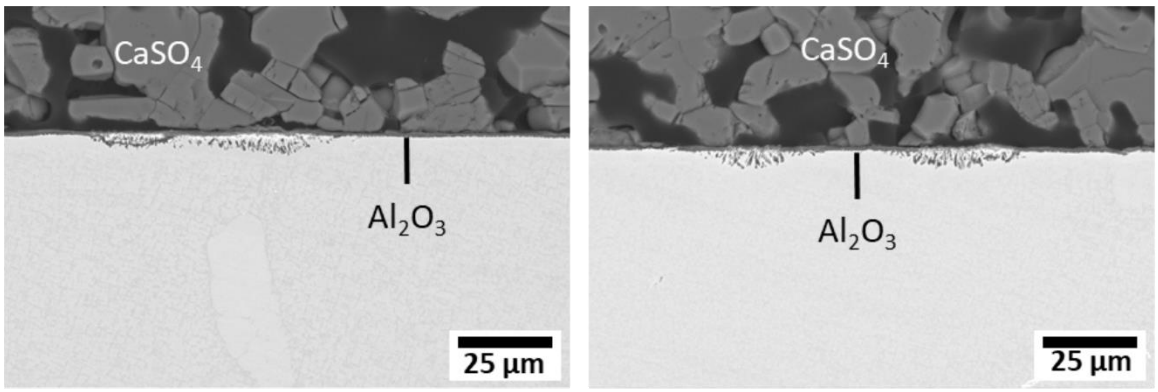

Figure 6-3. Reaction product formed on N5 (left) and N500 (right) exposed with 20 ± 1 $\frac{mg}{cm^2}$ of $CaSO_4$ for 100 h at 900°C.

Cross-sectional images of the reaction product formed on N5 and N500 exposed with 20 ± 1 $\frac{mg}{cm^2}$ of $CaSO_4$ for 0.5, 1, 8, and 24 h at 1150°C in air are shown in Fig. 6.4. After 0.5 h of exposure, EDS analysis determined that an external layer of Ca- and Al-rich reaction product containing 1-2 at% S was present on the surface of both alloys. Several large NiO nodules had formed on the N500 coupon while the Ca- and Al-rich layer on N5 remained largely intact. Additionally, there was a distribution of CrS particles in the γ'-denuded zone similar to that observed in the field-exposed components. The formation of sulfides suggests that SO_3 was released by the $CaSO_4$ deposit as the $CaSO_4$ was the only source of sulfur in the experiments. Figure 6.5 shows a higher magnification image of a NiO nodule on the surface of N500 after 0.5 h of exposure. The Ca- and Al-rich layer remains on the surface of the NiO nodule. This proves that the alloy was able to initially form the Ca- and Al-rich product but not able to supply sufficient aluminum to maintain the growth of the external product. Consequently, external scale breakdown occurred and resulted in nickel oxidation.

After 1 h of exposure, NiO nodules had formed on N5 which suggests that the incubation time for scale breakdown caused by $CaSO_4$ deposit is longer in N5 than N500. Areas of external

Ca- and Al-rich product were still present on N500 at this time but the NiO nodules had continued to grow and were the dominant feature on the surface of the alloy.

After 8 h of exposure, the NiO nodules on both alloys had coalesced to form a relatively uniform external nickel-rich reaction product. The product contained a significant amount of sulfur in addition to oxygen, which suggests duplex scale formation of NiO + NiS_x. In most areas, a thin layer of Al_2O_3 was present at the base of the nickel-rich product. The distribution of CrS particles in the γ'-denuded zone was still present after 8 h and, occasionally, Ni_3S_2 was observed below the Al-rich oxide layer. The degradation morphology in the coupons exposed for 24 h was similar to that observed after 8 h. The depletion of Al and Cr from the alloy subsurface near the scale-alloy interface was measured by EDS after the 24-h exposure. In alloy N5, the aluminum concentration dropped from the nominal composition of 13.8 at% to 7.7 at% and the chromium concentration dropped from 8.1 at% to 4.5 at %. In alloy N500, the aluminum concentration dropped from the nominal composition of 13.9 at% to 6.5 at% and the chromium concentration dropped from 6.9 at% to 3.7 at %.

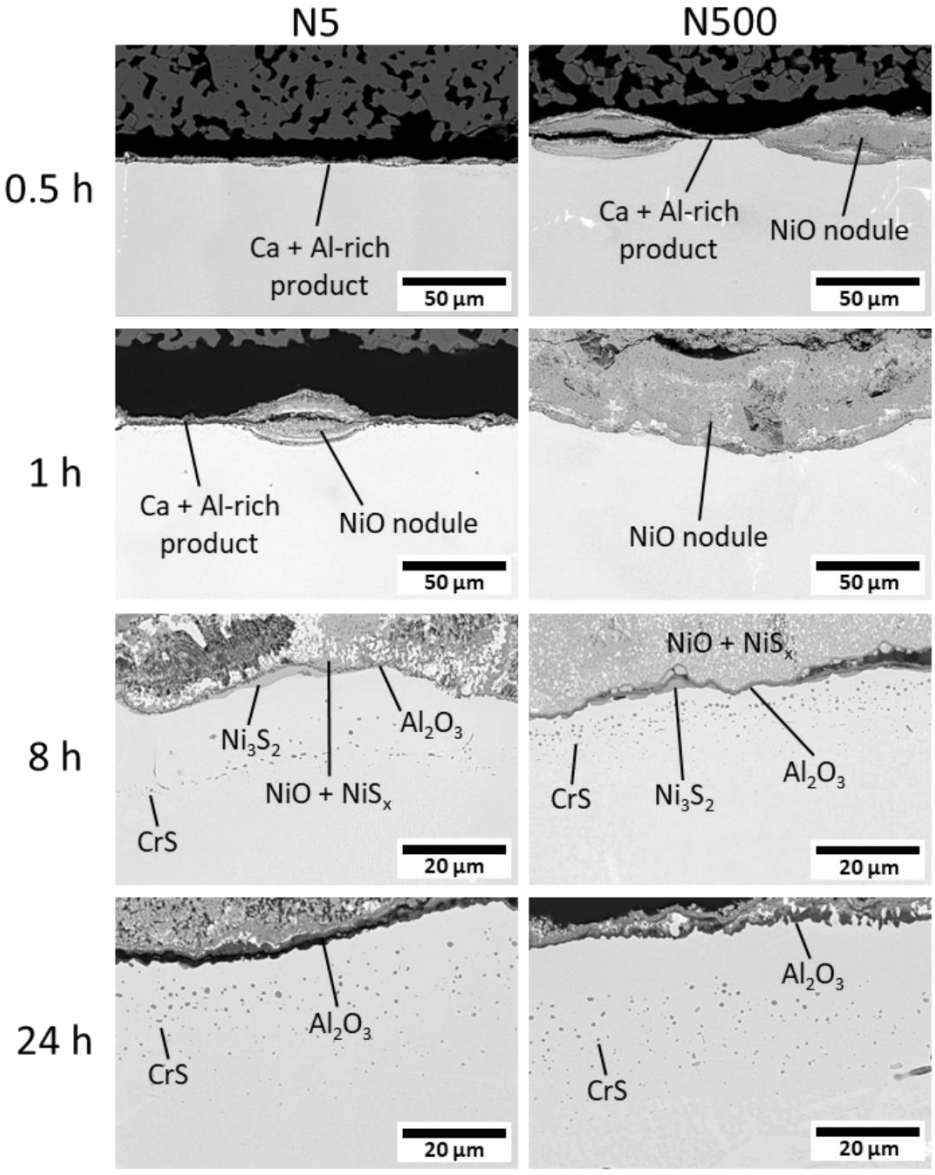

Figure 6-4. Reaction product formed on N5 and N500 exposed with 20 $\frac{mg}{cm^2}$ of $CaSO_4$ for 0.5, 1, 8, and 24 h at 1150°C in air.

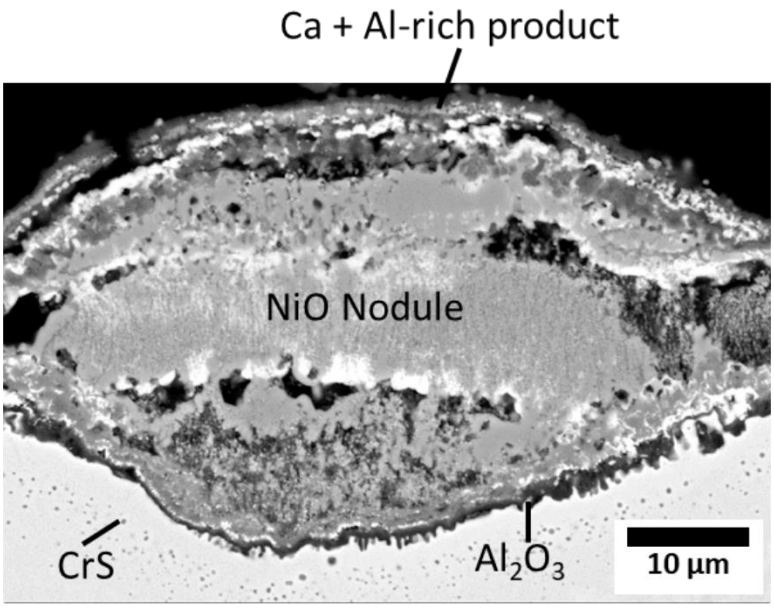

Figure 6-5. NiO nodule formed on N500 after 0.5 h of exposure at 1150°C with $CaSO_4$ deposit. Growth of the external Ca- and Al-rich product could not be maintained and scale breakdown resulted in NiO formation.

6.2.3 $CaSO_4$-Al_2O_3 Interactions

The degradation caused by $CaSO_4$ was further assessed by placing 20 $\frac{mg}{cm^2}$ of $CaSO_4$ on bulk Al_2O_3 and exposing the samples for 0.5, 8, and 24 h at 1150°C in air. Subsequent characterization of the reaction product by SEM and XRD showed that $Ca_4Al_6O_{16}S$ and $CaAl_2O_4$ had formed by 0.5 h and that the layer continued to grow with exposure time. The assemblage of the product was determined by EDS analysis to be $Ca_4Al_6O_{16}S$ above $CaAl_2O_4$. Representative XRD spectra from the reaction product are shown in Fig 6-6 and micrographs of the coupons exposed for 0.5 h and 24 h are shown in Fig. 6-7.

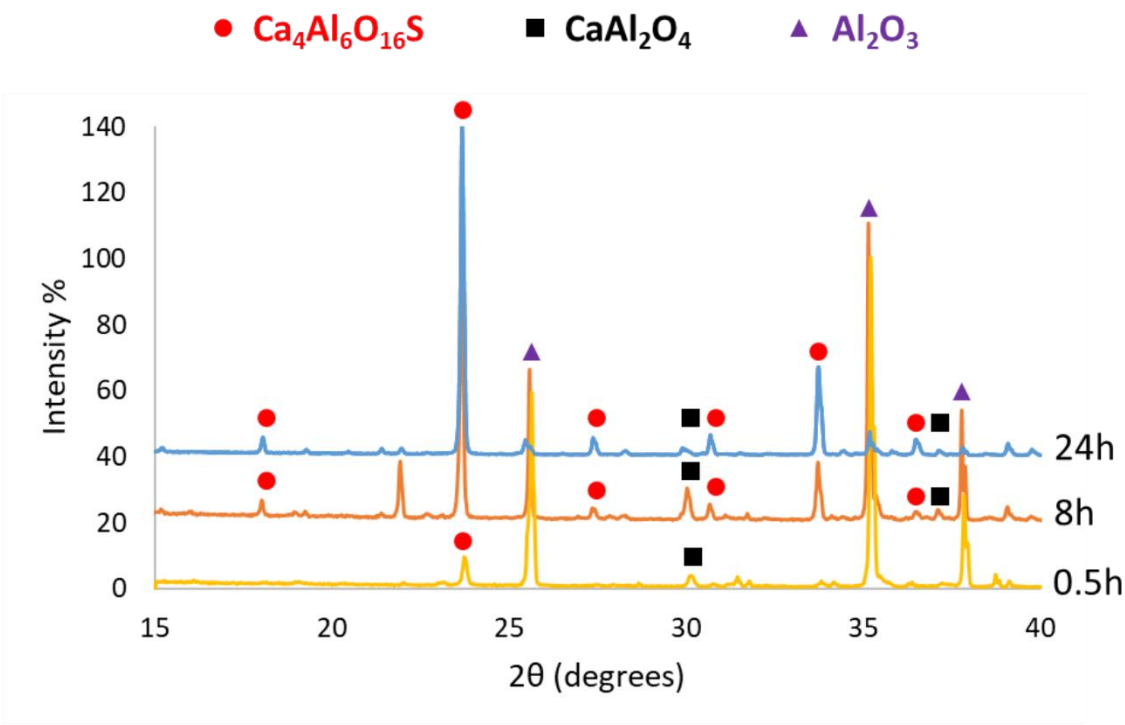

Figure 6-6. XRD analysis of reaction product formed between $CaSO_4$ and Al_2O_3 at 1150°C in air. The reaction product contains $Ca_4Al_6O_{16}S$ and $CaAl_2O_4$.

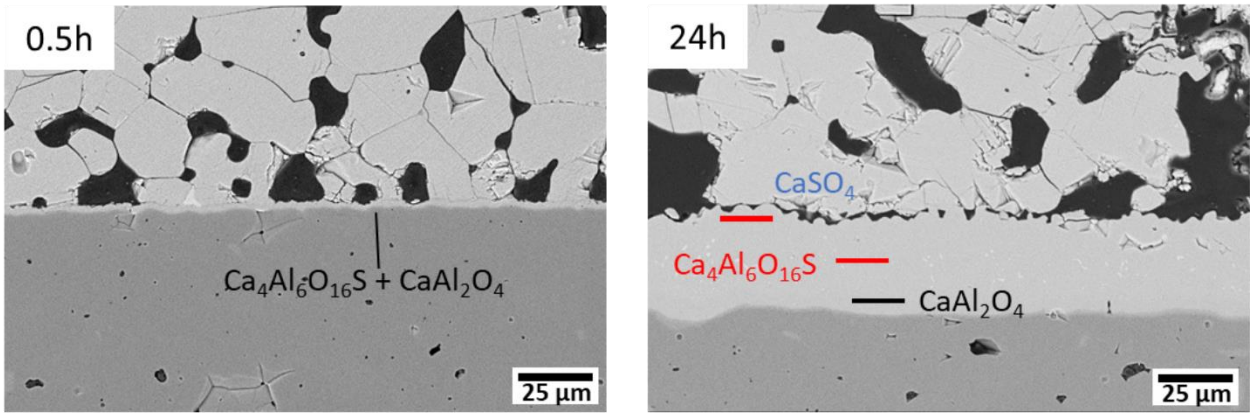

Figure 6-7. Assembelage of the reaction product formed between $CaSO_4$-Al_2O_3 coupons exposed for 0.5 h and 24 h at 1150°C in air as determined by EDS analysis.

Recording the thickness of the layer as a function of the square-root of time shows that the layer thickened according to diffusion-controlled parabolic kinetics with a rate constant of k_p = 4.6x10^{-11} $\frac{cm^2}{s}$ at 1150°C (Fig. 6.8). Additionally, the y-intercept value for the line of best fit for the data is negative. This indicates that there was an incubation stage prior to the formation of the reaction product. No enrichment of aluminum was detected in the $CaSO_4$ deposit, which suggests that the product grew via the inward transport of Ca and O through the $Ca_4Al_6O_{16}S$ / $CaAl_2O_4$ layer.

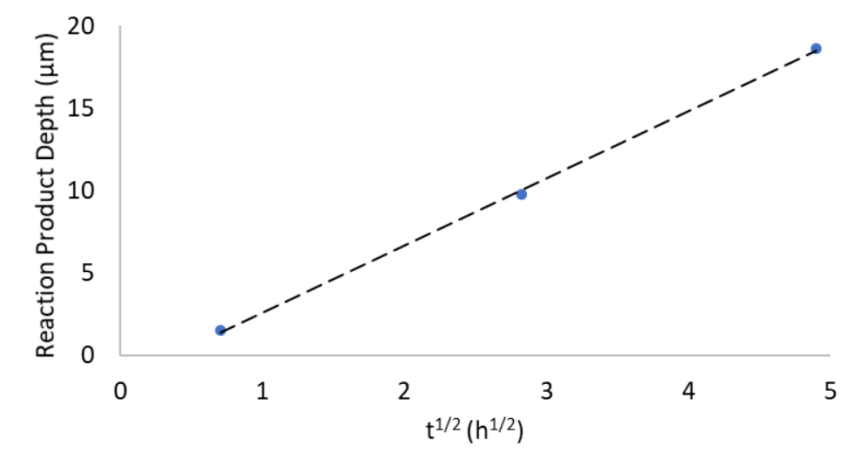

Figure 6-8. Parabolic plot of $Ca_4Al_6O_{16}S$ / $CaAl_2O_4$ growth at 1150°C.

The growth rate measured for the $Ca_4Al_6O_{16}S$ / $CaAl_2O_4$ structure at 1150°C can be compared to the growth of calcium aluminate at 1100°C measured by Gheno et al. [72] (k_p = 8x10^{-13} $\frac{cm^2}{s}$) and, in turn, those two rate constants can be substituted into equation 6.1 to determine an effective activation energy.

$$\ln\left(\frac{k_2}{k_1}\right) = -\frac{Q}{R}\left(\frac{1}{T_2} - \frac{1}{T_1}\right) \tag{6.1}$$

Specifically, using $k_1 = 8x10^{-13}\ \frac{cm^2}{s}$ at $T_1 = 1373K$ and $k_2 = 4.6x10^{-11}\ \frac{cm^2}{s}$ at $T_2 = 1423K$, equation 6.1 gives an activation energy of 1316 $\frac{kJ}{mol}$. This is an unrealistically large activation energy and thoroughly invalidates the calculation. Indeed, the activation energy for $CaAl_2O_4$ formation was reported by Mohamed et al. [79] to be 205 $\frac{kJ}{mol}$. What this does verify is that the growth rate of the $Ca_4Al_6O_{16}S$ / $CaAl_2O_4$ product is high and not dictated by the $CaAl_2O_4$ growth.

The solid-state synthesis of pure $Ca_4Al_6O_{16}S$ through the sintering of $CaCO_3$, Al_2O_3, and $CaSO_4 \cdot 2H_2O$ powders in air was the subject of a recent publication from Khessaimi et al. [86]. These authors utilized differential thermal analysis and thermogravimetric analysis measured in conjunction with XRD and electron microscopy to describe the formation of calcium aluminates and $Ca_4Al_6O_{16}S$ as a function of sintering time and temperature. They found that $CaAl_2O_4$ can be formed by reaction between Al_2O_3 and CaO, with the latter produced by the thermal decomposition of $CaCO_3$ and $CaSO_4$, as shown in equation 6.2. $Ca_4Al_6O_{16}S$ was formed through the reaction between $CaSO_4$ and $CaAl_2O_4$ as shown in equation 6.3.

$$CaO + Al_2O_3 \rightarrow CaAl_2O_4 \tag{6.2}$$

$$CaSO_4 + 3CaAl_2O_4 \rightarrow Ca_4Al_6O_{16}S \tag{6.3}$$

However, for the case of the present research, the XRD and EDS analysis of the $Ca_4Al_6O_{16}S$ / $CaAl_2O_4$ product did not detect CaO. Because of this, it is most likely that the reaction proceeds

due to direct interaction between $CaSO_4$ and Al_2O_3, as proposed in Fig 2.29 in section 2.3.2.2. Based on this information, schematics for the assemblage of the reaction product and an inferred diffusion path for the development of the product are shown in Figs. 6.9 and 6.10. The directions in the diffusion path shown in Fig. 6.10 reflect a predominance of Ca diffusion to form the $CaAl_2O_4$ product.

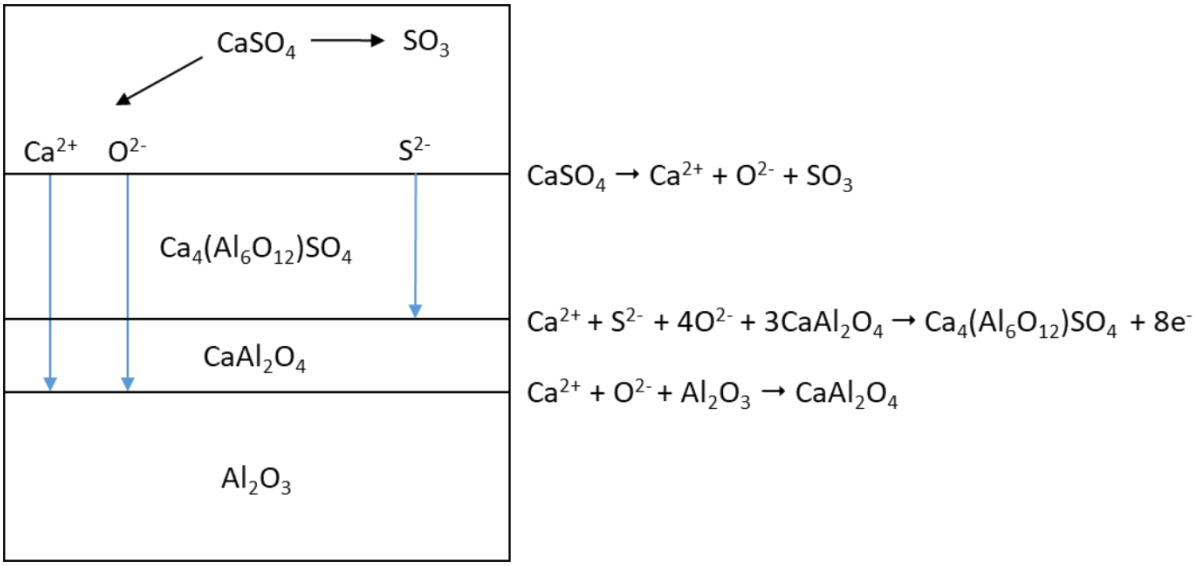

Figure 6-9. Assemblage of $CaSO_4$-Al_2O_3 reaction product and deduced principal interfacial reaction and diffusing species.

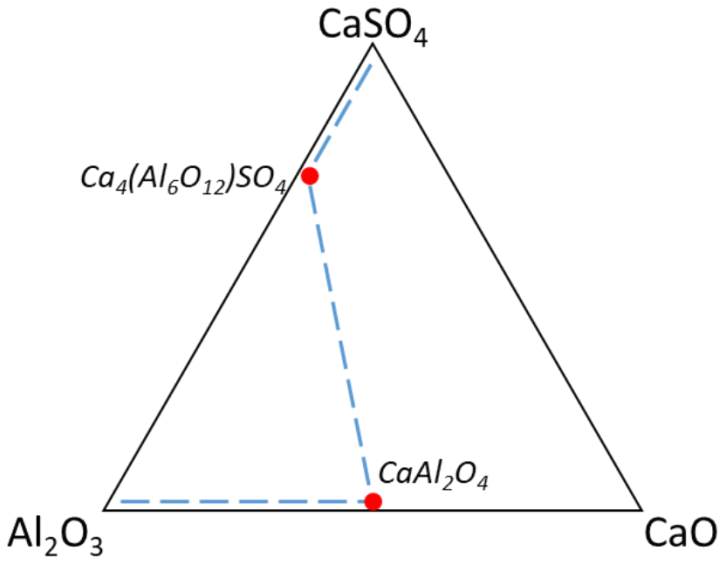

Figure 6-10. Inferred diffusion path for the formation of $CaSO_4$-Al_2O_3 reaction product.

During the initial stages of exposure, $CaSO_4$ reacts with Al_2O_3 to form Ca^{2+} and O^{2-} and release SO_3. $CaAl_2O_4$ is formed by reaction between Ca^{2+}, O^{2-}, and Al_2O_3. The generation of $CaAl_2O_4$ in contact with the $CaSO_4$ deposit results in the formation of $Ca_4Al_6O_{16}S$ through the reaction $CaSO_4 + 3CaAl_2O_4 = Ca_4Al_6O_{16}S$. Additionally, as described by Stringer and Minchener [12], the SO_3 released by the decomposition establishes a P_{S_2} gradient across the reaction product sufficient to drive the inward diffusion of S^{2-} through the reaction product. This would explain how nickel and chromium sulfides formed during the alloy exposures.

6.3 Conclusions

The experiments investigating the interactions between CaO deposit and N5 and N500 at 900°C and 1150°C reveal that CaO-induced degradation takes place through the same mechanisms

previously described by Gheno et al. and Jung at both temperatures [72, 73]. During the initial stages of oxidation, CaO deposit reacted with Al- and Cr-rich oxides to form non-protective C_xA_y and Ca_xCr_yO which prevented the establishment of a protective oxide scale. This resulted in broad front base-alloy oxidation. While this accelerated oxidation is severe, the results from the current experiments and the published literature did not show any signs of breakaway internal oxidation during prolonged exposure.

The experiments investigating the interactions between $CaSO_4$ deposit and N5 and N500 at 900°C and 1150°C revealed a significant difference in the extent of degradation between the two temperatures. At 900°C, both alloys formed an external Al_2O_3 scale. The presence of a small amount of Ca in the product indicated that there was reaction, though limited, between the deposit and the thermally grown oxides. At 1150°C, extensive oxidation and sulfidation was observed in both N5 and N500 due to the formation of fast growing $Ca_4Al_6O_{16}S$ / $CaAl_2O_4$ which eventually results in scale breakdown and base metal oxidation. It is inferred from the results of the $CaSO_4$-Al_2O_3 diffusion couple at 1150°C that the development of the $Ca_4Al_6O_{16}S$ / $CaAl_2O_4$ reaction product began with the formation of an external $CaAl_2O_4$ layer on the surface of the alloy through direct interaction between $CaSO_4$ and Al_2O_3. With $CaSO_4$ in contact with $CaAl_2O_4$ the reaction $CaSO_4 + 3CaAl_2O_4 = Ca_4Al_6O_{16}S$ takes place quite quickly as $Ca_4Al_6O_{16}S$ is detected by XRD after only 0.5 h of exposure. Additionally, this reaction involves the release of SO_3 from the $CaSO_4$ which establishes sulfur potential across the reaction product that drives the inward diffusion of sulfur. The ingress of sulfur results in the formation of CrS particles and, eventually, Ni_3S_2 in the alloy subsurface. Shortly after $Ca_4Al_6O_{16}S$ / $CaAl_2O_4$ formation, the external product broke down locally and NiO nodules began to form. NiO nodule formation was observed after 0.5 h in N500 and after 1 h in N5. After 8 h of exposure at 1150°C the NiO nodules on both alloys grew and

coalesced to form a relatively uniform external Ni-rich layer. After 24 h of exposure, the subsurface of the alloys were significantly depleted of aluminum and chromium and enriched with sulfur.

7.0 Development of the Bi-Thermal Replication Testing Procedure

7.1 Introduction

The isothermal experiments done on alloys N5 and N500 with CaO and $CaSO_4$ deposits provided further insights into how deposit-alloy interactions take place in the high-pressure turbine environment. It is inferred that $CaSO_4$-induced degradation, and the resulting subsurface depletion of Al and Cr and enrichment in S, make the alloy susceptible to internal oxidation. However, prolonged isothermal exposures at high temperatures do not result in the breakaway internal oxidation seen in the field-exposed parts. It was inferred that there is an important link between the conditions of the exposure and the kinetic competition between internal and external oxidation. Therefore, a new experiment was designed which applied what was learned about $CaSO_4$-alloy interactions at 1150°C with knowledge of the high-pressure turbine environment to replicate the breakaway internal oxidation observed in the field-exposed parts. In this experiment, alloys were subjected to $CaSO_4$-induced degradation then subsequently exposed to conditions representative of a high-pressure turbine which promote internal oxidation. The development of the experimental procedure was based on the thermodynamic and kinetic aspects of the selective oxidation of aluminum in nickel-based alloys.

7.2 High Pressure Turbine Exposure Conditions Which Promote Internal Oxidation

The influence of subsurface Al and Cr depletion on the susceptibility of a nickel-based alloy to internal oxidation can be visualized by plotting the bulk composition of N500 and the composition of the γ'-denuded zone after 24 h of exposure with $CaSO_4$ at 1150°C onto the oxide map for Ni-Cr-Al alloys at 1200°C (Fig. 7.1). Here it is seen that, even though the depleted zone composition lies in the region for internal oxidation, breakaway internal oxidation did not occur during the 1150°C exposure with $CaSO_4$. The reason for this is that the oxide map predicts behavior based on the bulk alloy composition. For the exposures with $CaSO_4$ deposit, the supply of aluminum to the oxidation front from the unaffected aluminum-rich bulk was sufficient to form protective Al_2O_3 during prolonged exposure at 1150°C. Therefore, the approach taken to replicate the internal oxidation-sulfidation observed in the components of interest was to expose the subsurface-depleted alloy to conditions that are more favorable to internal oxidation in the kinetic competition between internal and external oxidation of aluminum.

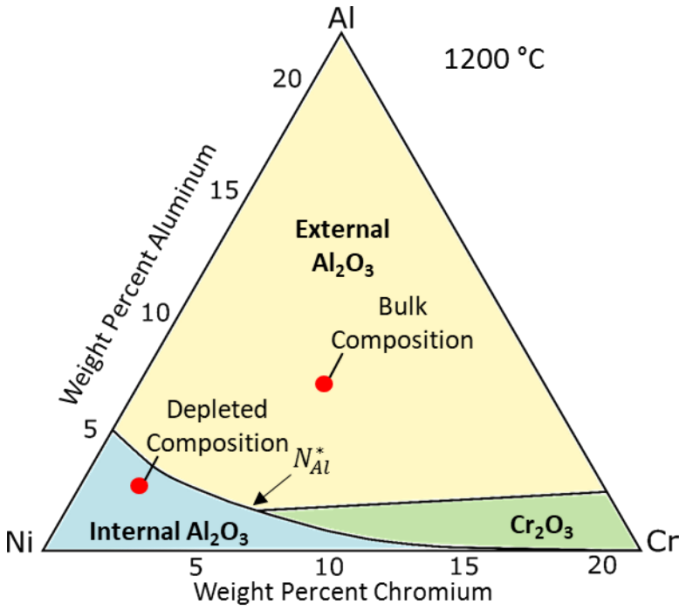

Figure 7-1. The "oxide map" for Ni-Cr-Al at 1200°C with bulk composition of N500 and subsurface composition after 8 h of exposure in air at 1150°C with 20 ± 1 mg/cm^2 of CaSO4. Adapted from [19].

Two environmental factors in the high-pressure turbine environment that influence the kinetic boundary between internal and external oxidation are temperature variation and the presence of steam in the atmosphere as presented in sections 2.2.3.2 and 2.2.3.3. For a brief review of the influence of temperature and steam on $N_{Al}^{*,establish}$ recall equation 2.21.

$$N_{Al}^{*,establish} = \left[\frac{\pi g^{*}}{3} N_{O}^{(S)} \frac{D_O V_m}{D_{Al} V_{ox}}\right] \tag{2.21}$$

Both temperature and the presence of steam influence $N_{Al}^{*,establish}$. When temperature increases, the values of both D_O and D_{Al} increase but, due to the difference in activation energy for interstitial oxygen diffusion and substitutional aluminum diffusion in nickel, $\frac{D_O}{D_{Al}}$ and hence

$N_{Al}^{*,establish}$ increase with decreasing temperature [19]. With regard to steam, recent research shows that its presence during high temperature oxidation can increase $N_{Al}^{*,establish}$ in Ni-Cr-Al alloys by affecting the thermodynamic driving forces for the nucleation of Al_2O_3 precipitates resulting in an increase of g*, the critical volume fraction of oxide precipitates needed to establish a continuous scale [55].

The temperature of high-pressure turbine components during a flight is highly variable. During takeoff and climb, components can briefly see temperatures as high as 1200°C. In the subsequent cruise stage, components are exposed for longer times at intermediate temperatures typically between 600°C and 900°C [87]. This means that the beginning of the thermal cycle for a flight may expose components with $CaSO_4$ deposits to temperatures high enough to cause significant degradation. Following this initial high-temperature exposure, the subsurface-depleted alloy would then see a longer exposure at a lower temperature in the presence of steam generated by the combustion of jet fuel. Internal oxidation in the subsurface-depleted alloy is more kinetically favorable during the cruise stage of the thermal cycle due to lower exposure temperature and could initiate should external scale breakdown occur. This insight led to the development of a two-stage "bi-thermal" test procedure for coupons with $CaSO_4$ deposits in the presence of steam.

The test procedure begins with an 8-h "initiation stage" exposure at 1150°C (2100°F) and is followed immediately by a 96-h exposure at 871°C (1600°F). The atmosphere for the test is air + 30% steam. A schematic diagram of the exposure conditions is presented in Fig. 7.2.

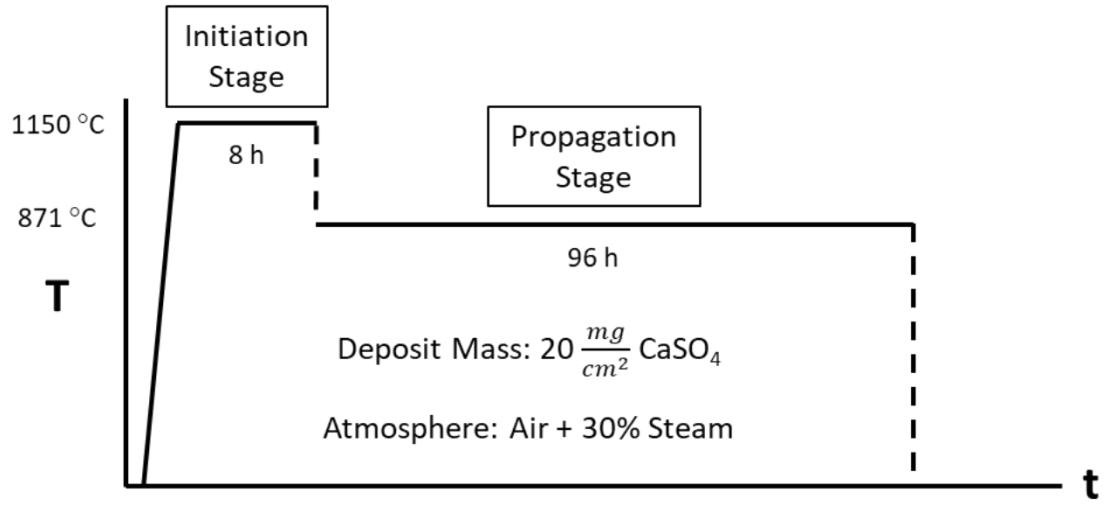

Figure 7-2. Bi-thermal replication testing procedure.

7.3 Results of the Bi-Thermal Replication Testing Procedure

Cross-sectional images of N5 and N500 coupons after the bi-thermal experiment are shown in Fig. 7.3. This figure also contains images from field-exposed component #3 (N500) for the sake of comparison. The morphology of the reaction product present in the coupons from the bi-thermal test and in component #3 consists of three characteristic features. The first is a thick external layer comprised of mixed oxides (primarily NiO) and, in the coupons from the bi-thermal tests, calcium aluminate. The second characteristic feature is a thick internal oxidation zone containing coarse Al- and Cr-rich oxide precipitates. The third characteristic feature is a distribution of fine CrS precipitates in the γ'-denuded zone ahead of the internal oxidation front. The similarities between the degradation in the coupons exposed to the bi-thermal test and the field-exposed components indicate that the new test procedure accurately reproduces the mode of degradation seen in the field-exposed components.

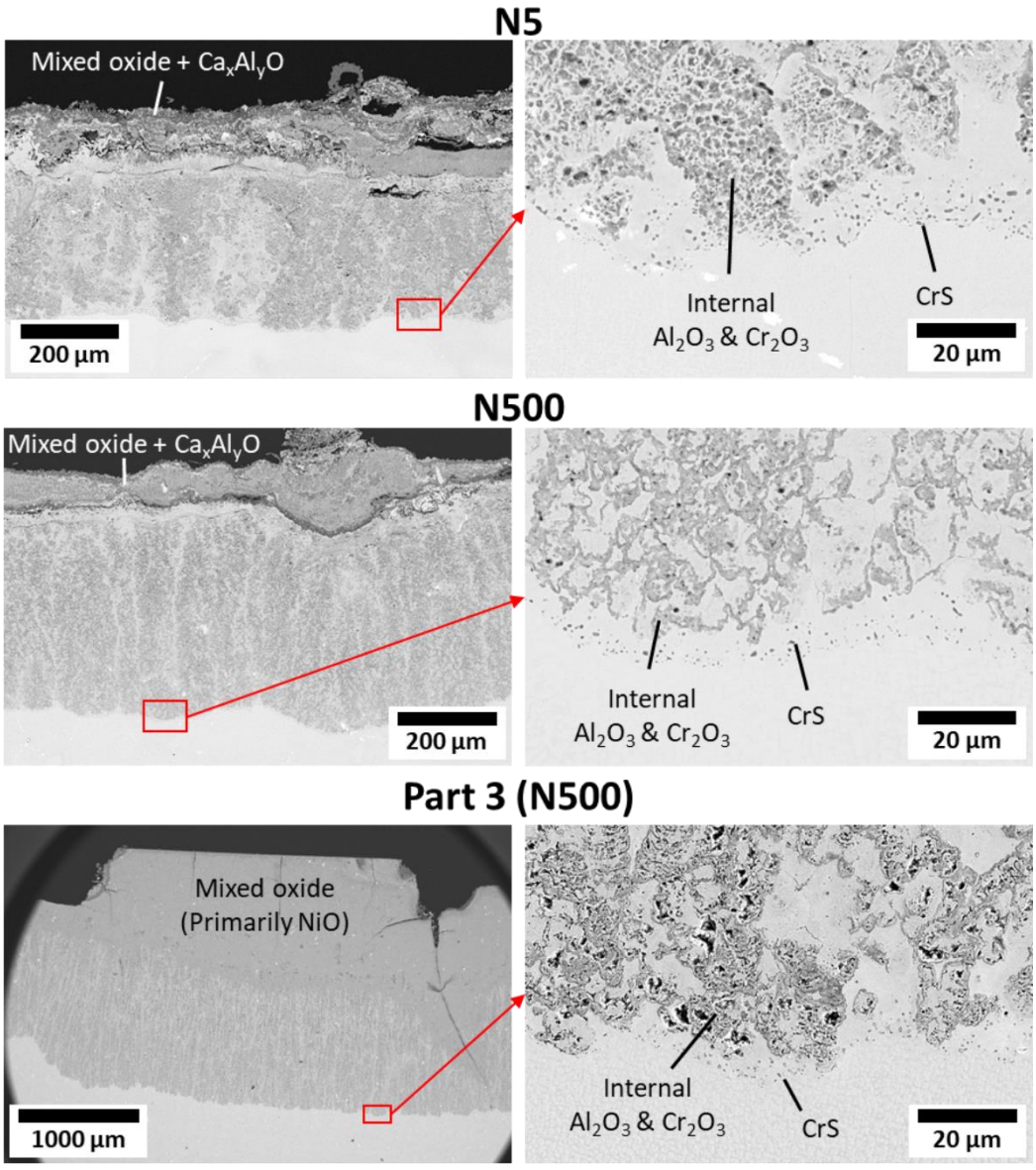

Figure 7-3. Cross-sectional images of N5 and N500 coupons exposed to bi-thermal test and of N500 component #3.

7.4 Evolution of the Corrosion Product During Bi-Thermal Testing

A time study was conducted to determine how the degradation develops during the bi-thermal exposure. This was done by conducting additional experiments and stopping the test at three different points during the bi-thermal exposure. Figure 7.4 displays the results of these experiments where N5 and N500 coupons were removed: a.) after the 8-h 1150°C initiation stage; b.) after 1 h at the propagation-stage temperature of at 871°C; and c.) after the full 96-h duration of the 871°C propagation stage. After the 8-hour initiation stage, $CaSO_4$-induced degradation as described in section 6.2.2 has caused the subsurface depletion of Al and Cr and enrichment of S in the alloy subsurface. After 1 h at the propagation-stage temperature of 871°C, there are areas on the alloy where the external product was NiO + NiS_x and internal oxide precipitates rich in Al and Cr had formed in the alloy subsurface. CrS precipitates were present ahead of the internal oxidation front. After the full 96-h propagation stage, the degradation matched that found observed in Fig 7.3.

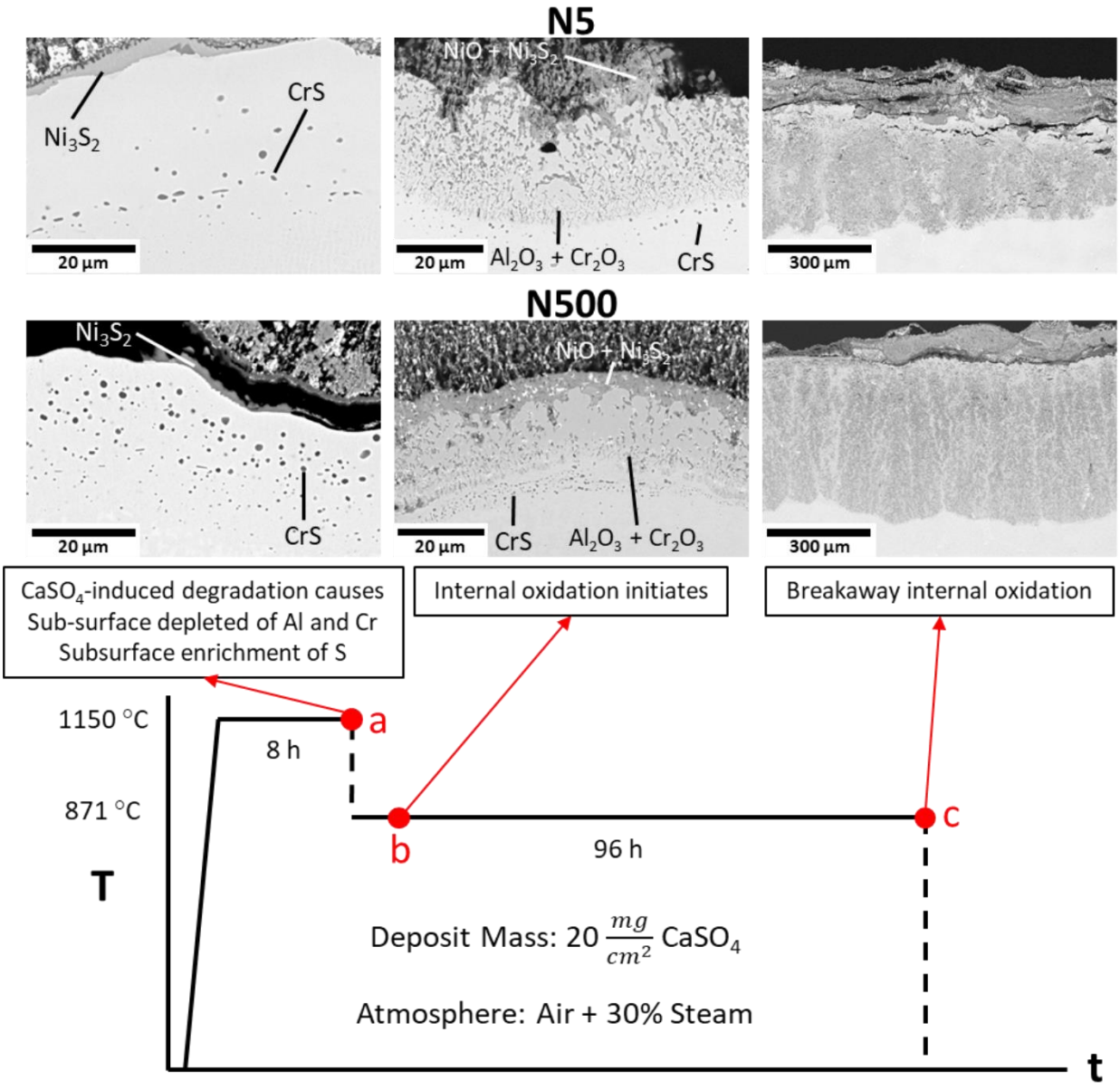

Figure 7-4. Cross-sectional images of coupons removed a.) after the 8-h initiation stage b.) after 1 h of the 871°C propagation stage exposure and c.) after 96 h of the 871°C propagation stage exposure.

The results of this experiment prove that alloys attacked by $CaSO_4$ at high temperature become susceptible to internal oxidation at lower temperatures in a steam-containing atmosphere; however, the individual influence of the thermal profile, steam content, and subsurface sulfur enrichment is not provided by these results. To gain a deeper understanding of the mechanisms by which $CaSO_4$-induced internal oxidation take place, further experiments were carried out to isolate the influence of thermal profile, water vapor, and subsurface sulfur enrichment on the mode of degradation in alloy N500.

7.5 Influence of Thermal Profile and Water Vapor on the Mode of Degradation

The influence of thermal profile was isolated by comparing the degradation from the bi-thermal exposure in air + 30% steam (*cf.* Fig. 7.3) to a 104-h isothermal exposure at 1150°C in air + 30% steam. The initial $CaSO_4$ deposit mass was 20 $\frac{mg}{cm^2}$ in both experiments. A cross-sectional micrograph of the coupon from the isothermal exposure is shown in Fig. 7.5. No internal oxidation was observed. Most of the external reaction product spalled on cooling but, in regions where the product was retained, continuous Al_2O_3 was observed. Thus, it is inferred that, even in the presence of steam in the atmosphere, internal oxidation is kinetically unfavorable in the subsurface depleted alloy at 1150°C. The most likely reason for this is that diffusion of aluminum from the aluminum-rich bulk of the alloy is large enough at 1150°C to establish and maintain an Al_2O_3 scale that prevents internal oxidation in the steam containing atmosphere.

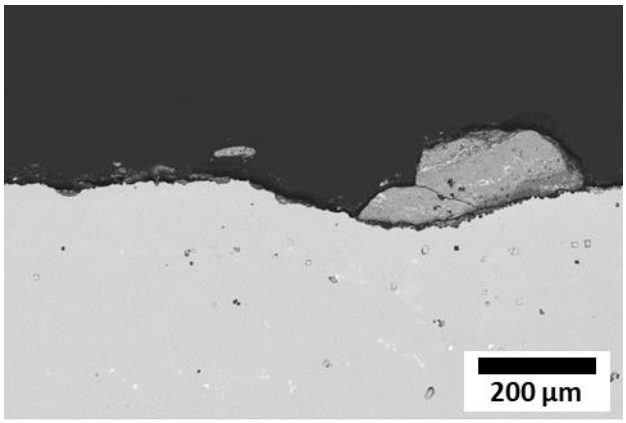

Figure 7-5. Cross-sectional micrograph isothermal 1150°C exposure in air + 30% steam.

The influence of steam was isolated by comparing a bi-thermal exposure in air + 30% steam to an identical exposure in bottled air. The thermal profile for the exposures is the same as described in Fig. 7.2 but now with an 871°C propagation-stage duration of 60 h. Cross-sectional micrographs of coupons after the experiments are shown in Fig. 7.6. The coupon exposed to air + 30% steam exhibits typical $CaSO_4$-induced breakaway internal oxidation. The coupon exposed to air formed an external mixed oxide and calcium aluminate layer typical of $CaSO_4$-induced degradation at 1150°C; however, Ni- and Al-rich oxide (likely spinel) is present at the scale-alloy interface and there is no significant internal oxidation. Jung [73] reported that the presence of steam during high temperature exposure of nickel-based alloys with calcium-rich deposits accelerated the depletion of aluminum from the subsurface of the alloy. In this thesis, an experiment was conducted where the 8-h 1150°C initiation stage exposure was done in air followed by a 60-h 871°C propagation stage exposure in air + 30% steam. The same internal oxidation zone morphology as formed during the experiments conducted entirely in air + 30% steam develops. This suggests that the subsurface depletion caused by $CaSO_4$-induced degradation

at 1150°C in air is sufficient to make the alloys susceptible to internal oxidation during the propagation stage.

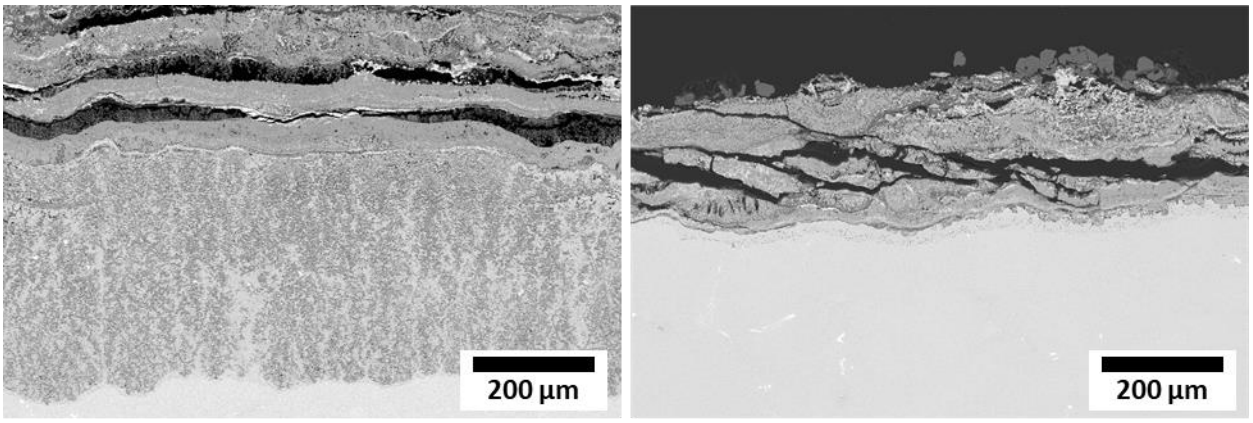

Figure 7-6. Cross-sectional image of the coupons exposed to bi-thermal exposure in air + 30% steam (left) and in bottled air (right).

The results of these experiments prove that both a lower temperature "propagation stage" temperature and the presence of steam in the atmosphere during the propagation stage are necessary for breakaway internal oxidation to occur in N5 and N500 subjected to $CaSO_4$-induced degradation at 1150°C. This supports the assertion that the kinetic competition between internal and external oxidation dictates the subsequent oxidation behavior of alloys attacked by $CaSO_4$ deposits.

7.6 Influence of Subsurface Sulfur Enrichment on the Mode of Degradation

The influence of subsurface sulfur enrichment on the oxidation behavior of subsurface depleted N5 and N500 was investigated using two experiments. The first was comparing the bi-

thermal experiment in air + 30% steam with $CaSO_4$ deposit from Fig 7.6 to a test with the same exposure conditions but with 8.25 $\frac{mg}{cm^2}$ of CaO deposit (8.25 $\frac{mg}{cm^2}$ deposit of CaO has the same number of moles as the 20 $\frac{mg}{cm^2}$ $CaSO_4$ deposit used). The experiment was an 8-h initiation stage at 1150°C followed by a 60-h propagation stage exposure at 871°C in air + 30% steam. The results of the test with CaO are shown in Fig. 7.7. The coupon exposed with CaO did not exhibit internal oxidation and the structure of the external product had no significant differences from that reported in Fig. 6.1. The external product formed on the coupon with CaO deposit appeared to be well adhered to the alloy while the external product formed with $CaSO_4$ was highly defective due to significant porosity and apparent delamination of the product.

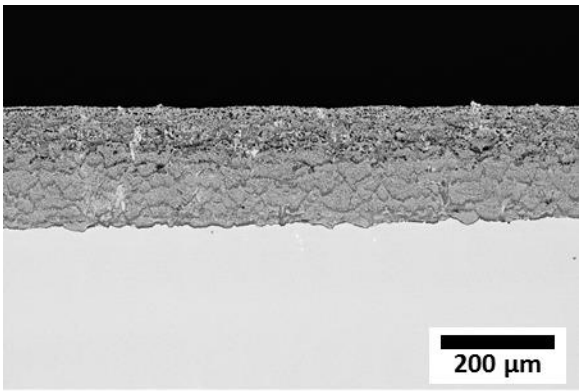

Figure 7-7. Cross-section of N500 after bi-thermal exposure in air + 30% steam with CaO deposit (*cf.* Fig. 7.6 (Left)).

The detrimental influence of sulfur enrichment is likely tied to the effect of sulfur on external scale adherence. From the time study done to determine how internal oxidation initiates during the bi-thermal exposure with $CaSO_4$ in section 7.4, it was determined that the internal oxidation initiates locally where non-protective external $NiO+NiS_x$ was present. There is a large body of research that definitively shows that sulfur impurities in Ni-based alloys segregate to the

scale-alloy interface during oxidation. This segregation results in the promotion of void formation and porosity at the scale-alloy interface and poor scale adherence which increases susceptibility to scale spallation [88–93].

It is possible that the scale breakdown during bi-thermal testing in air + 30 % steam with $CaSO_4$ deposit occurs due to spallation caused by the accumulation of stresses in the poorly adherent scale. This could occur during the bi-thermal experiments due a combination of growth stresses and thermal stresses. When external scales grow thick, as they do during $CaSO_4$-induced degradation at 1150°C, the compressive strain energy in the product increases [94]. Upon cooling from 1150°C to the propagation-stage temperature of 871°C, additional compressive stress is generated in the product due to a mismatch in the coefficient of thermal expansion for the scale and the underlying alloy [95]. Should the stress exceed the toughness of the interface, cracking or spallation will occur and create initiation sites for internal attack during the propagation stage. This would also explain why no internal attack occurred in the coupon exposed with CaO. While there is significant subsurface depletion of Al caused by CaO-induced degradation, the external product is quite adherent due to the absence of sulfur and there is a smaller possibility for scale breakdown to allow for internal oxidation.

Additional insight into the influence of sulfur on the mode of degradation during bi-thermal exposure was gained by comparing a control bi-thermal test with $CaSO_4$ deposit to one where the alloy was de-sulfurized after the 8-h initiation stage. The test began when N500 coupons with 20 $\frac{mg}{cm^2}$ of $CaSO_4$ deposit were exposed for 8 h at 1150°C in air + 30% steam. After this initiation stage, the coupons were removed from the furnace and the surface of the coupons were grit blasted with silica to remove any external oxide scale on the coupons. Descaling was done to ensure that the surface of the coupon to be de-sulfurized was exposed to the reducing gas during the de-

sulfurization treatment. The control coupon underwent the same de-scaling procedure to match the surface preparation of the de-sulfurized coupon prior to the propagation-stage exposure. The coupon to be de-sulfurized was exposed in a reducing atmosphere of Ar + 5% H_2 at 1000°C for 24 h. After this de-sulfurization treatment, both alloys were exposed for 60 h at 871°C in air + 30% steam. The results from this set of experiments are shown in Fig. 7.8. The corrosion product formed on the control coupon consisted an external layer of NiO above internal intrusions of Al- and Cr-rich oxides with a morphology similar to that observed in standard bi-thermal tests. NiO was also formed on the de-sulfurized coupon but an Al-rich scale was present at the scale-alloy interface. No internal oxidation was observed in the de-sulfurized coupon.

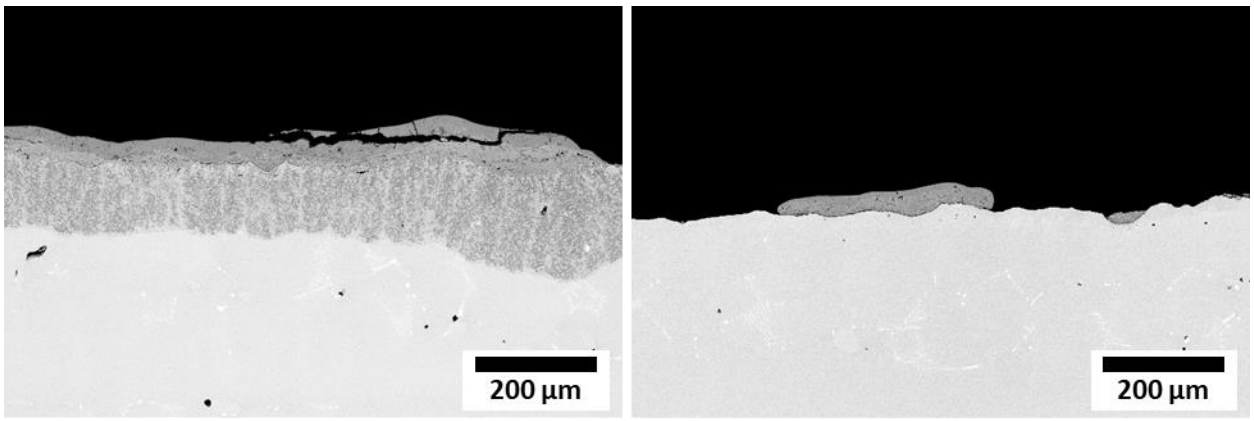

Figure 7-8. Cross-sectional micrographs of control bi-thermal test coupon (left) and the coupon which was de-sulfidized prior to the propagation stage (right).

The results of this experiment suggest that CrS formation and sulfur enrichment in the subsurface are detrimental to the establishment of a protective Al_2O_3 scale even when the subsurface depleted alloy is exposed to the oxidizing environment. Several researchers have reported that the enrichment of sulfur at the oxidation front can indeed promote coarse internal oxide morphologies similar to those observed in the current bi-thermal experiments [96–98]. The

formation of CrS particles ahead of the oxidation front is likely to be detrimental to the establishment of Al_2O_3 because the sulfide formation removes Cr, an element that known to be very beneficial in decreasing $N_{Al}^{*,establish}$ as described in section 2.2.3.1, from the alloy near the oxidation front. The depletion of Cr from the oxidation front is also a self-sustaining process during internal oxidation-sulfidation. During oxidation-sulfidation, sulfur is continuously forced deeper into the alloy ahead of the oxidation front due to the oxidation of CrS precipitates as described by Spengler et al. [98] and Meijering [99]. Because CrS is less thermodynamically stable than Cr_2O_3, as the P_{O_2} ahead of the internal oxidation front increases, CrS becomes unstable. The precipitates oxidize and release the tied-up sulfur. The freed sulfur then diffuses deeper into the alloy where the sulfur and oxygen activity are low and the chromium activity is high. This allows new CrS particles to form ahead of the internal oxidation front which maintains the depletion of chromium at the oxidation front.

7.7 Conclusions

The bi-thermal testing procedure in air + 30% steam with $CaSO_4$ deposit was shown to be very effective in reproducing the severe internal oxidation observed in the field-exposed components examined in this study. It appears that the key to achieving reproduction of the degradation observed in the field-exposed components at the lab scale was more accurately simulating the thermal profile and atmosphere that high pressure turbine components are exposed to during flight. Characterizing the development of the internal oxidation product helped us identify three criteria that must be met for breakaway internal oxidation to occur in alloys N5 and N500.

The first criterion for causing internal oxidation in alloys N5 and N500 is that subsurface depletion of Al and Cr as well as subsurface enrichment of S are necessary for internal oxidation to occur during testing. This critical depletion was attained through $CaSO_4$-induced degradation during the initial 1150°C exposure. The second criterion is that external scale breakdown must occur to allow oxygen to permeate into the alloy. Early in the 871°C propagation stage exposure it was observed that internal oxide precipitates only formed in areas where there was no evidence of an external Al-rich oxide layer. During bi-thermal testing, scale breakdown most likely occurs due to stress buildup upon cooling to 871°C. The final criterion is that the environmental conditions must favor internal oxidation in the exposed subsurface-depleted alloys. The experiments in this chapter showed that both a lower exposure temperature and the presence of 30% steam in the atmosphere are necessary for internal oxidation to occur in the alloy.

8.0 Factors Affecting the Susceptibility of Superalloys to Breakaway Internal Oxidation-Sulfidation

8.1 Design of Systematic Experiments

Three sets of experiments were completed to systematically address how the: 1.) 1150°C initiation-stage duration; 2.) initial $CaSO_4$ deposit mass; and 3.) propagation-stage temperature influence the susceptibility of Rene N5 and N500 to breakaway internal oxidation.

The influence of the 1150°C initiation-stage duration on the susceptibility of N5 and N500 to internal oxidation was investigated by linking the susceptibility to internal oxidation to the extent of subsurface aluminum depletion and sulfur enrichment caused by $CaSO_4$-induced degradation. To accomplish this, the subsurface regions of the N5 and N500 coupons exposed with $20\frac{mg}{cm^2}$ of $CaSO_4$ for 0.5, 1, 8, and 24 h at 1150°C in air from Fig. 6.4 in section 6.2.2 and were characterized in greater detail. The extent of subsurface aluminum depletion was measured by EDS analysis and the extent of subsurface sulfur enrichment was quantified using image analysis to measure the volume fraction of CrS particles in the γ'-denuded zone. Following this, a series of bi-thermal experiments in air + 30% steam were conducted on N5 and N500 coupons with 1150°C initiation-stage durations of 0.5, 1, 8, or 24 h followed by a 60-h propagation stage at 871°C. A schematic summarizing the conditions of the bi-thermal tests is given in Fig. 8.1.

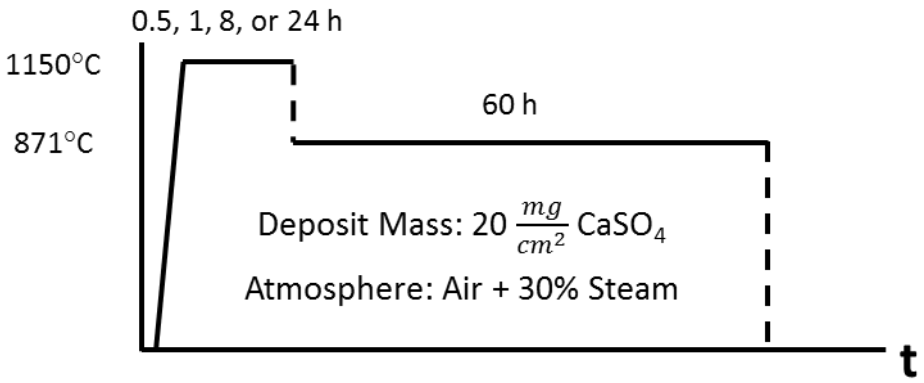

Figure 8-1. Experiments used to determine the effect of 1150°C initiation-stage duration on the mode of $CaSO_4$-induced internal attack.

The influence of initial deposit mass on the susceptibility of the alloys to breakaway internal oxidation was investigated by exposing N500 coupons with 5, 10, 20, or 40$\frac{mg}{cm^2}$ of $CaSO_4$ to a bi-thermal exposure in air + 30% steam with an initiation stage duration of 1 or 8 h at 1150°C followed by a 96-h propagation-stage exposure at 925°C. A schematic summarizing the conditions used for this set of experiments is shown in Fig. 8.2.

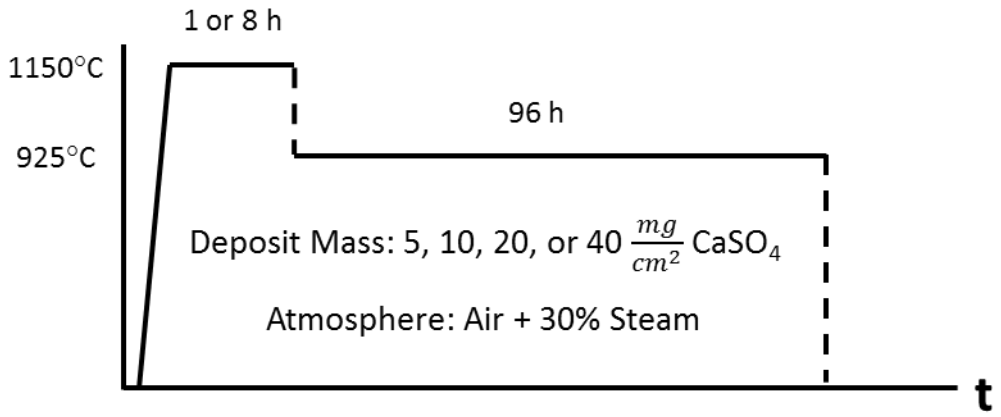

Figure 8-2. Experiments used to evaluate influence of $CaSO_4$ deposit mass on alloy susceptibility to breakaway internal oxidation.

The influence of the propagation-stage temperature on the rate of degradation during the propagation stage was investigated by conducting a series of exposures having an 8-h initiation stage at 1150°C followed by a 96-h propagation stage at a temperature of 704, 816, 925, 1038 or 1150°C. The atmosphere for the tests was air + 30% steam and the initial deposit mass was 20 $\frac{mg}{cm^2}$ of $CaSO_4$. The severity of the attack as a function of the propagation-stage temperature was quantified by measuring the maximum sound metal attack in each coupon. The sound metal attack is defined in this paper as the depth of the degradation from the original coupon surface (three cross-sections per coupon were examined). Accurate measurements were made possible by leaving a portion of the alloy surface free of deposit to retain the original surface of the coupon. The thermal profiles for these experiments are shown in Fig. 8.3.

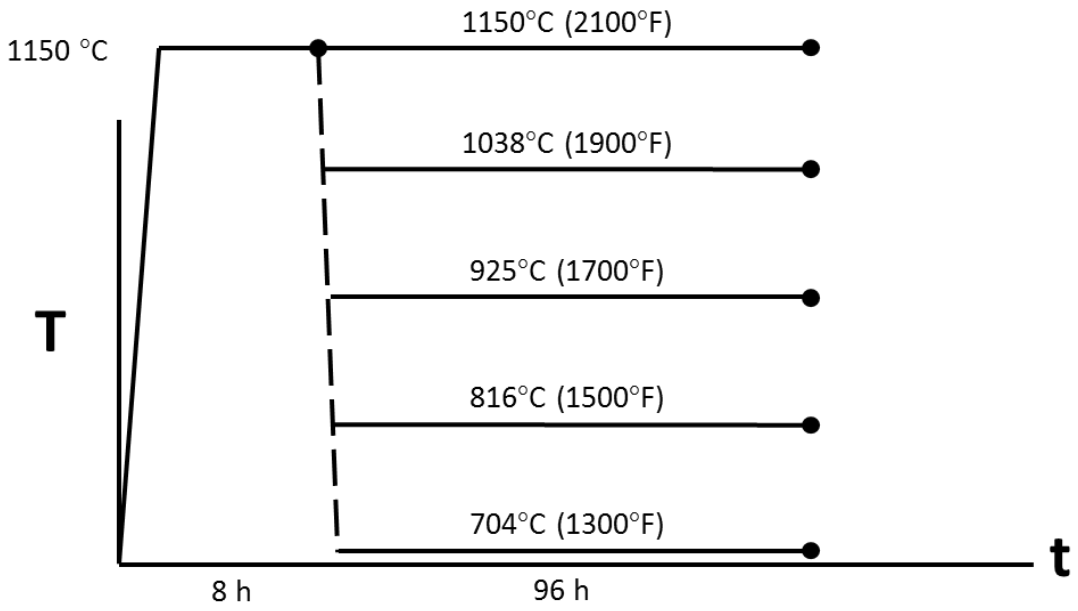

Figure 8-3. Experiments used to determine the effect of propagation stage temperature on the mode and extent of degradation. Initial $CaSO_4$ deposit mass is 20 $\frac{mg}{cm^2}$ and the atmosphere is air + 30% steam.

8.2 Influence of 1150°C Initiation Stage Duration on the Susceptibility of N5 and N500 to Internal Attack

Cross-sectional SEM images of N5 and N500 exposed to the conditions outlined in Fig 8.1 are shown in Fig. 8.4. The plots in Fig. 8.5 show the measurements of: 1) the depth of the γ′-denuded zone; 2) the concentration of aluminum near the scale-alloy interface; and 3) the extent of subsurface sulfidation for each exposure time. Three areas per sample where external product remained intact were chosen for analysis. Taking measurements of the alloy subsurface with intact external scale was done because it would yield more consistent data regarding the conditions of the subsurface prior to the propagation stage. In areas where the external product had broken down,

measuring denuded zone depth and composition became difficult due to rapid degradation in the subsurface.

The measurements of the aluminum concentration near the scale-alloy interface reveal that it decreases rapidly from the bulk value of 13.9 at% to about 6.5 at% in both alloys after only 0.5 h of exposure at 1150°C. The interfacial aluminum content remains relatively constant with exposure time up to 24 h around a value of roughly 7 at% aside from an outlying value of 2.1 at% for the 8 h N5 sample. Plotting the γ'-denuded zone depth versus the square root of time confirms that the depth increases with diffusion-controlled kinetics because the line that the data points is linear. This implies that the $CaSO_4$ deposit maintains good adherence with the growing reaction product up to 24 h of exposure and that Al consumption rate is controlled by Al diffusion through the denuded zone with fixed boundary conditions at the scale-denuded zone interface and the denuded zone-base alloy interface. From this information, a kinetic analysis can be done to quantify the rate of Al consumption from the alloy subsurface. This rate can then be compared to the rate of Al consumption required to form $Ca_4Al_6O_{16}S$ / $CaAl_2O_4$ in the $CaSO_4$-Al_2O_3 diffusion couple from section 6.2.3 in order to determine if the rate of aluminum consumption from the alloy during $CaSO_4$-induced degradation at 1150°C is consistent with the aluminum consumption required to form $Ca_4Al_6O_{16}S$ / $CaAl_2O_4$ in the more well behaved $CaSO_4$-Al_2O_3 diffusion couple.

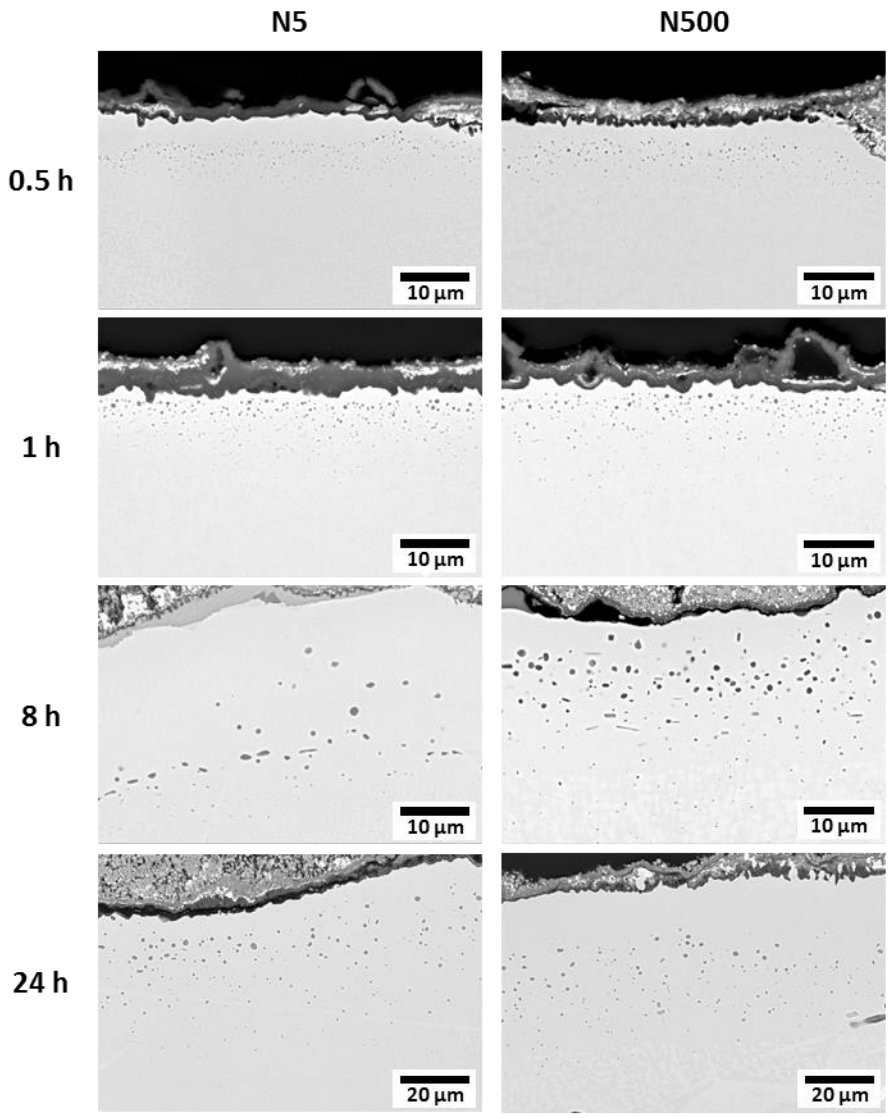

Figure 8-4. Images of the subsurface depletion zone that develops in alloys N5 and N500 during $CaSO_4$-induced degradation in air at 1150°C.

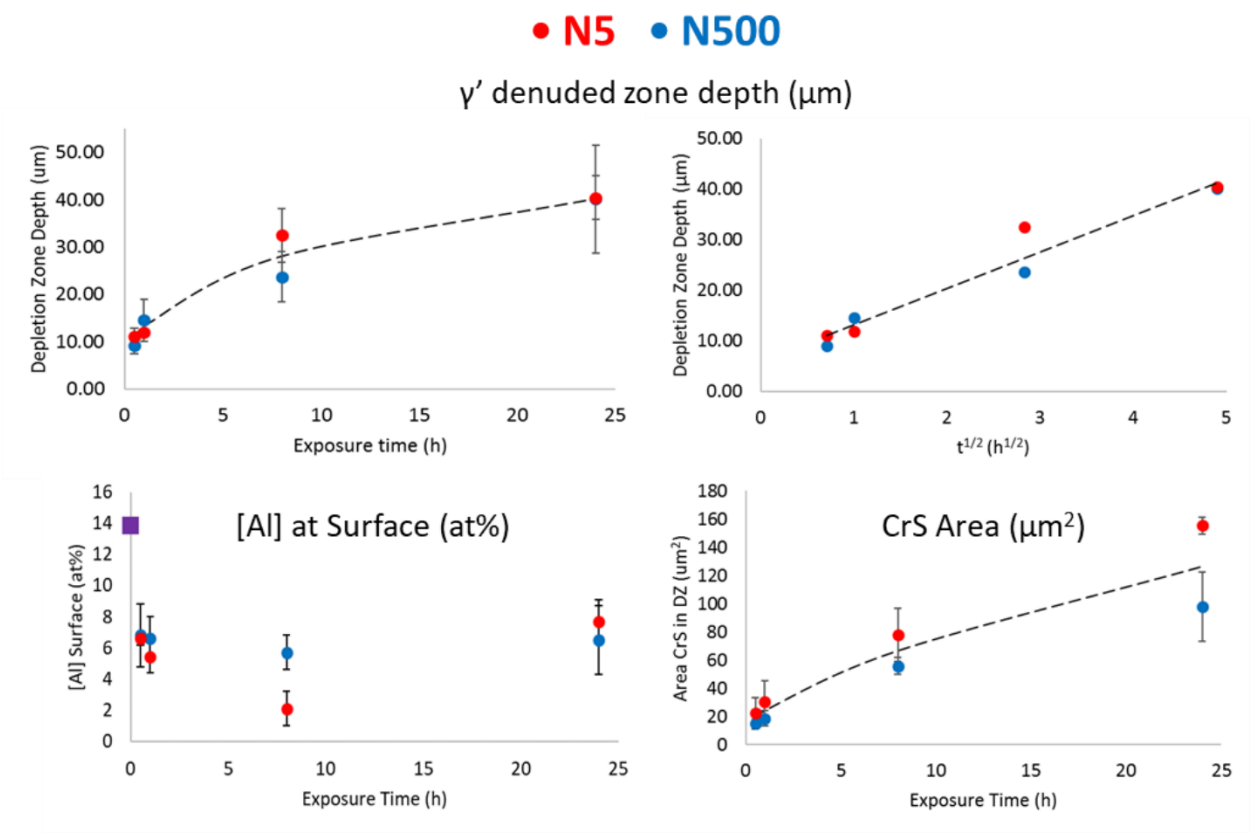

Figure 8-5.Charts showing the depth of the γ' denuded zone (top left and right), the concentration of aluminum near the scale-alloy interface (bottom left), and the area of CrS particles formed in the γ'-denuded zone (bottom right) with increasing exposure time at 1150°C in air + 30% steam with 20$\frac{mg}{cm^2}$ of $CaSO_4$ deposit.

The Al concentration at the scale-denuded zone interface is fixed by the equilibrium between the scale and the denuded zone which was measured to be roughly 7 at%. The concentration at the denuded zone-base alloy interface is the solubility limit for Al in the γ-phase at 1150°C. CALPHAD (CALculation of PHAse Diagrams) computations for alloys with the composition of N5 and N500 predict this value to be 9.9 at% in both alloys. The depth and rate of denuded zone growth can be modeled by equation 8.1 as presented by Carter et al. [100] where N_{Al}^{γ} is the Al concentration at the γ-γ + γ' interface, N_{Al}^{o} is the Al concentration in the bulk alloy, and N_{Al}^{i} is the Al concentration at the scale-alloy interface. The quantities u and α are given in

equations 8.2 and 8.3 where k_c is a corrosion constant that measures the aluminum consumption rate, X_d is the denuded zone depth, and V_i is the molar volume of phase "i". The value of k_c can be converted to a k_p that represents the growth rate constant of an Al_2O_3 scale required to form a denuded zone of depth X_d in time t using equation 8.4. This k_p will be called k_p^{DZ}. Fig. 8.6 is a schematic showing the concentration profile for Al in the alloy subsurface with the variables for the analysis. The result of this analysis yields a value of $6.2 \times 10^{-10} \frac{cm^2}{s}$ for the k_p^{DZ} of an Al_2O_3 scale required to form a 40.3 μm γ'-denuded zone in 24 h.

$$\frac{N_{Al}^{\gamma} - N_{Al}^{i}}{N_{Al}^{o} - N_{Al}^{\gamma}} = \sqrt{\pi}\, \alpha\, exp(\alpha^2)\, [erf(\alpha) - erf(u)] \tag{8.1}$$

$$u = \sqrt{\frac{k_c}{4D_{Al}}} \tag{8.2}$$

$$\alpha = \frac{X_d}{2\sqrt{D_{Al}t}} \tag{8.3}$$

$$k_p^{DZ} = k_c \left(\frac{V_{Al_2O_3}}{2V_{Al}}\right)^2 \tag{8.4}$$

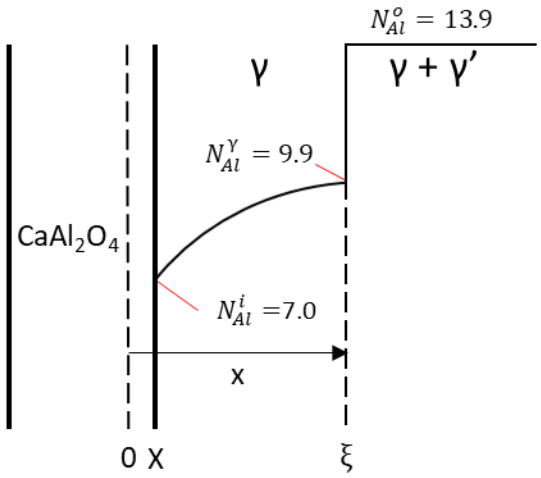

Figure 8-6. Schematic diagram used for the kinetic analysis to quantify the rate of Al consumption required to form the γ'-denuded zone.

To compare the value of 6.2x10^{-10} $\frac{cm^2}{s}$ for the k_p^{DZ} of an Al_2O_3 scale required to form a 40.3 μm γ'-denuded zone in 24 h to the aluminum consumption rate required to form the $Ca_4Al_6O_{16}S$ / $CaAl_2O_4$ product in the $CaSO_4$-Al_2O_3 diffusion couple at 1150°C, the rate constant for $Ca_4Al_6O_{16}S$ / $CaAl_2O_4$ growth (4.6x10^{-11} $\frac{cm^2}{s}$) must be converted to an equivalent rate constant for Al_2O_3 growth. For this analysis, The $Ca_4Al_6O_{16}S$ / $CaAl_2O_4$ thickness is approximated to be entirely $Ca_4Al_6O_{16}S$ because the EDS and XRD analysis show the $CaAl_2O_4$ layer to be thin. Because there are 3 units of Al_2O_3 in each unit of $Ca_4Al_6O_{16}S$, the equivalent rate constant for Al_2O_3 growth from the diffusion couple (k_p^{DC}) is given by equation 8.5 and yields k_p^{DC} = 1.5x10^{-11} $\frac{cm^2}{s}$.

$$k_p^{DC} = 4.6 \times 10^{-11} \left(\frac{3V_{Al_2O_3}}{V_{Ca_4Al_6O_{16}S}} \right) \tag{8.5}$$

$\frac{k_p^{DZ}}{k_p^{DC}}$ = 41 which means that the aluminum consumption from the alloy during $CaSO_4$-induced degradation is greater than the aluminum consumption required to form $Ca_4Al_6O_{16}S$ / $CaAl_2O_4$ at 1150°C in the $CaSO_4$-Al_2O_3 diffusion couple. This is reasonable because it can be seen from figure 8.4 that reaction product that forms on the alloys is poorly adherent and contains porosity. These defects would reasonably accelerate the consumption of aluminum from the alloy. However, this analysis only provides an estimation of the Al consumption. Due to assumptions in the analysis, the exact degree to which Al consumption from the alloy is greater than the Al consumption required to form $Ca_4Al_6O_{16}S$ / $CaAl_2O_4$ in the $CaSO_4$-Al_2O_3 diffusion couple is unknown. In any case, as the 1150°C initiation stage duration increases, the extent of depletion in the denuded zone increases. Because of this it is reasonable to expect that the susceptibility of the alloys to internal oxidation during bi-thermal testing with $CaSO_4$ deposit should increase with increasing initiation stage duration.

Figure 8.7 shows cross-sectional images of the corrosion product formed on alloys N5 and N500 after bi-thermal tests in air + 30% steam with 20 $\frac{mg}{cm^2}$ of $CaSO_4$ deposit using a fixed propagation stage of 60 h at 871°C. The 1150°C initiation-stage duration for these experiments was 0.5, 1, 8, or 24 h. Significant internal oxidation occurred for initiation-stage durations of 0.5, 1, and 8 h in alloy N500 and only after the 8-h initiation stage in N5. No internal oxidation occurred in the samples subjected to a 24-h initiation stage.

In alloy N500, the internal oxidation presented as localized pits for the 0.5- and 1-h initiation-stage exposures but was more uniform for the 8-h exposure where about 80% of the surface in the cross-section exhibited internal attack to a similar depth. The maximum attack depth was relatively low for the 0.5-h initiation stage but then similarly deep for the 1-h and 8-h initiation-stages. In alloy N5, several NiO nodules formed along the alloy surface for the 0.5- and

1-h initiation-stage exposures; however, Al-rich subscale had formed below the nodules, which must have prevented internal oxidation during the propagation stage. Like in N500, the depth of internal oxidation zone formed in the N5 coupons exposed with the 8-h initiation stage was relatively uniform across the surface of the alloy. The influence of alloy composition on susceptibility to internal oxidation will be covered in chapter 9. The following paragraphs will focus on the influence of 1150°C initiation-stage duration on the extent of degradation in N500.

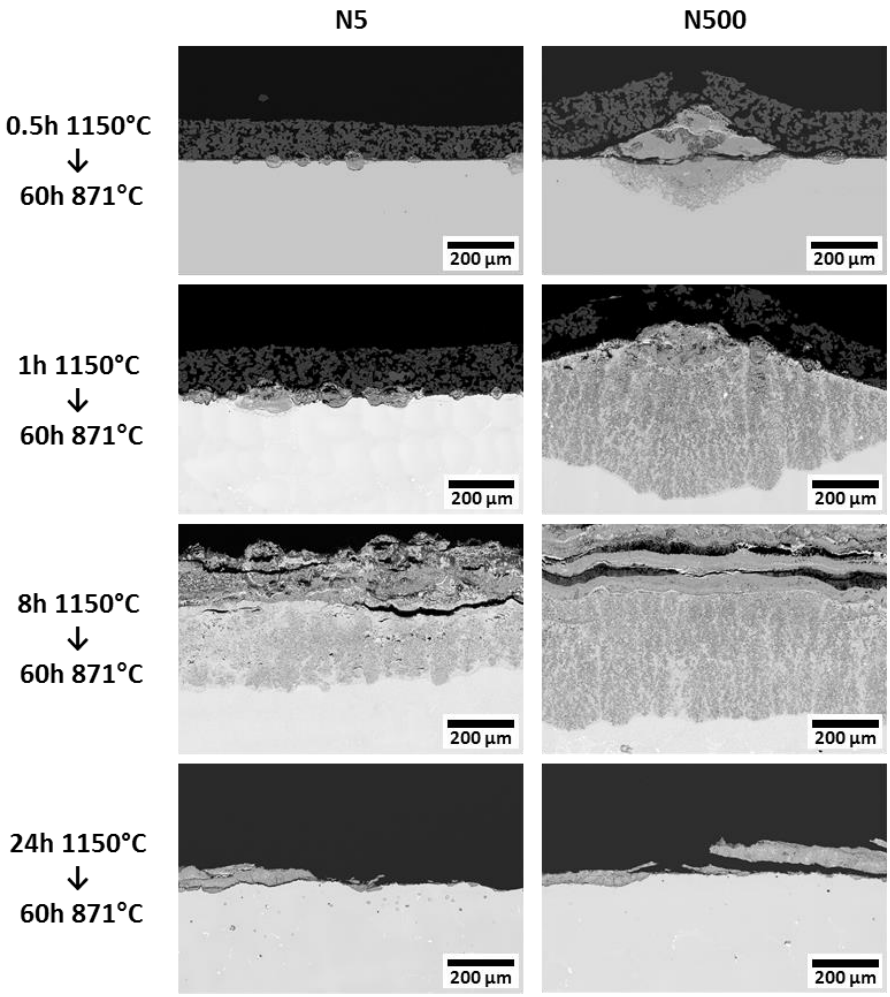

Figure 8-7. Corrosion product developed on coupons subjected to bi-thermal exposure in air + 30% steam with initiation stage durations of 0.5, 1, 8, or 24 h.

In alloy N500, the transition in the attack morphology from localized pits for coupons subjected to an initiation-stage exposure of 0.5 or 1 h to more uniform degradation for the coupon with an 8-h initiation-stage suggests that the number of initiation sites for internal oxidation increases with initiation time up to at least 8 h and then, for some reason, the alloy becomes less susceptible to degradation as the initiation-stage duration increases to 24 h. In chapter 7 we inferred that two important factors related to the alloy's susceptibility to internal oxidation after the initiation stage are the propensity for external scale spallation and the extent of Al and Cr depletion in the alloy subsurface. Unfortunately, how the results of the subsurface analysis are linked quantitatively to the propensity for scale spallation and extent of depletion remains unclear. However, qualitative inferences for the behavior can be made from these observations.

The results of the subsurface analysis suggest that the propensity for scale spallation should remain high with increasing initiation time. It is well known that impurities of S in the alloy subsurface segregate to and embrittle the scale-alloy interface and increase the tendency for scale spallation [88–93]. Because the volume fraction of CrS in the γ'-denuded zone increases with exposure time, the alloy subsurface likely remains enriched in S throughout the initiation stage up to 24 h. Therefore, the scale is likely to spall when growth or thermal stresses develop in the scale, particularly upon cooling to the propagation stage temperature. In fact, the strain energy in the reaction product should increase with initiation stage duration due to the thickening of the product. With respect to the subsurface depletion of Al, because the depletion zone thickens with time, the alloy subsurface should become more susceptible to degradation with initiation stage duration.

The increase in susceptibility to internal oxidation for initiation times between 0 and 8 h is consistent with these observations but the absence of internal oxidation after the 24-h initiation stage is an unexpected result. A second identical 24 h initiation stage experiment with two coupons

of N5 and N500 was completed with the same results; the alloys were less susceptible to $CaSO_4$induced internal oxidation in air + 30% steam with a 24 h 1150°C initiation-stage duration compared to an 8h 1150°C initiation-stage duration. Because the depth of Al depletion was greatest after 24 hours, it was inferred that the low susceptibility to internal attack after 24 h is more closely linked to the probability of scale breakdown than the susceptibility of the subsurface to internal oxidation. To test this, an additional experiment on alloy N500 was done where the alloy was subjected to a 24-h exposure at 1150°C in air + 30% steam with $CaSO_4$ deposit. Following the 24 h initiation-stage, the surface of the coupon was grit blasted to remove any external oxide product. The bare and subsurface depleted alloy was then subjected to the 60-h propagation stage exposure at 871°C in air + 30% steam. Cross-sectional analysis shows that internal oxidation occurred in the coupon. The result of this experiment is shown in Fig. 8.8.

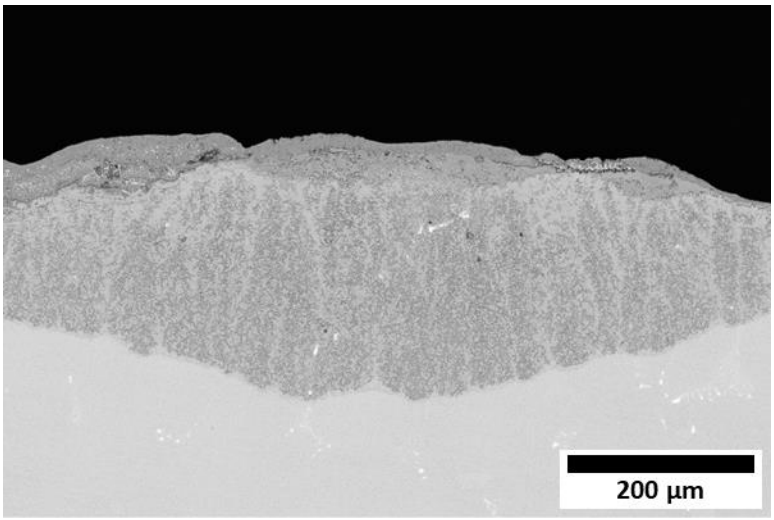

Figure 8-8. Internal attack observed in a sample subjected to bi-thermal testing with a 24 h initiation stage at 1150°C followed by de-scaling prior to being exposed for 60 h at 871°C in air +30% steam.

This result shows the subsurface of N500 after a 24-h initiation-stage exposure has, indeed, been sufficiently depleted to undergo internal oxidation should the subsurface be exposed to the environment but, evidently, scale cracking or spallation did not occur on cooling to the propagation stage temperature. The reason for this behavior is unknown, but it is possible that the growth strain during the prolonged initiation stage became large enough to cause crack formation in the scale during the high temperature initiation stage when external Al_2O_3 formation is favorable. If this occurred, the alloy would be able to re-establish Al-rich oxide product with less accumulated growth strain; therefore, the external product would be protective upon cooling to 871°C. This is only speculation however and requires further study that is beyond the scope of this thesis.

8.3 Influence of Deposit Mass on the Susceptibility N500 to Internal Attack

The influence of deposit mass was investigated by conducting the set of bi-thermal tests from Fig 8.2. Cross-sectional images from the coupons are shown in Fig 8.9. For the bi-thermal tests with the 1-h initiation stage, all four deposit masses caused localized internal oxidation with similar morphology and depth. For the set of bi-thermal tests with the 8-h initiation stage, the coupons with 10, 20, and 40 $\frac{mg}{cm^2}$ of $CaSO_4$ deposit yielded similar internal oxidation attack while no internal oxidation occurred in the coupon with 5 $\frac{mg}{cm^2}$ of deposit.

The results indicated that a certain amount of deposit is needed to cause breakaway internal oxidation, but, for every mass above that critical amount, there was variability. For the samples exposed to an initiation stage of 8 h, only ≈50% of the coupon surface in cross-section underwent internal oxidation for deposit amounts of 10 and 40 $\frac{mg}{cm^2}$ of $CaSO_4$ while the entire cross-section

examined for the coupon with 20 $\frac{mg}{cm^2}$ of $CaSO_4$ underwent internal oxidation. Due to the localized nature of the degradation, this set of experiments is not sufficient to conclude if there is a significant effect of deposit mass on the fraction of the surface attacked during bi-thermal exposure.

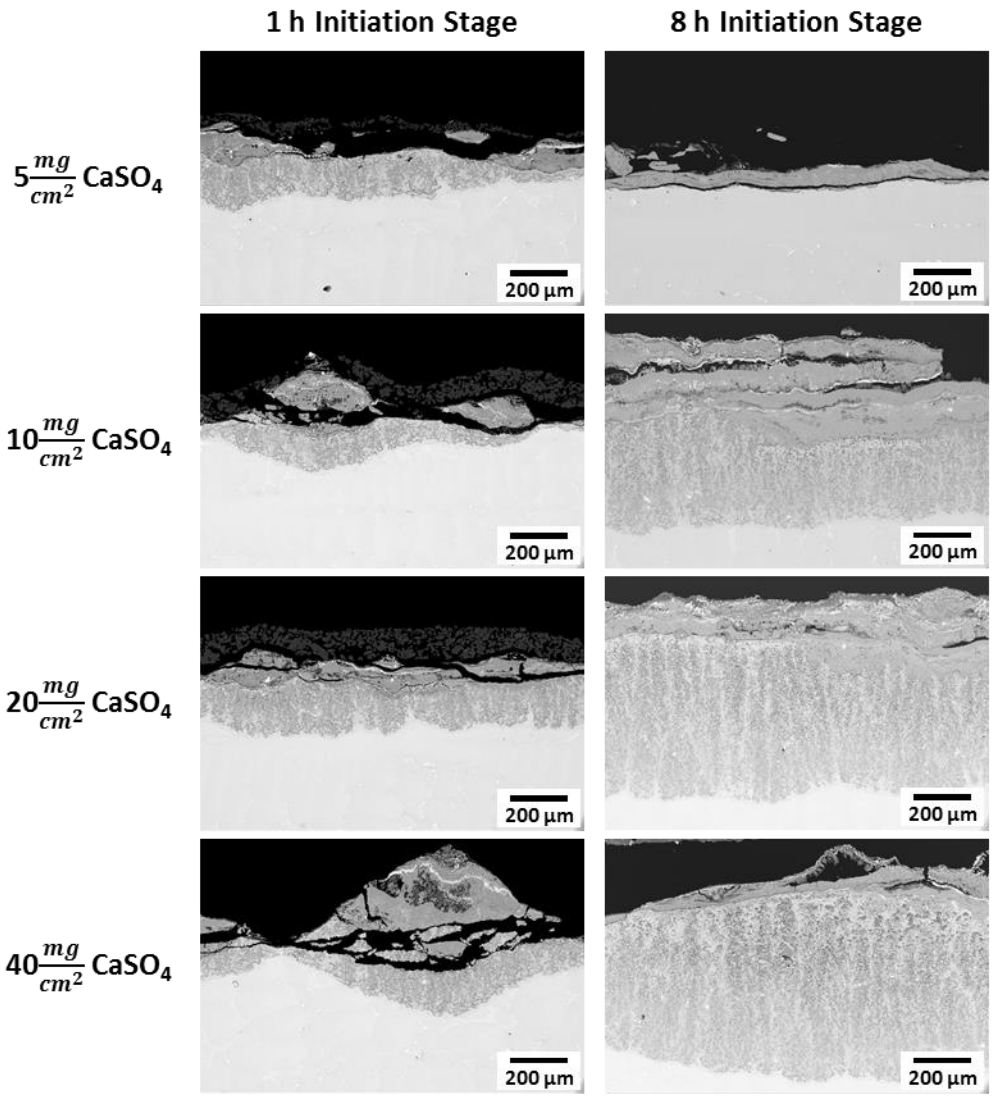

Figure 8-9. Cross-sectional images of N500 subjected to bi-thermal exposure in air + 30% steam. The 1150°C initiation-stage duration was 1 or 8 h and the subsequent 96-h propagation stage temperature of 925°C.

Based on the similarity of the morphology and depth of the internal attack observed for both initiation-stage durations, it was inferred that the initial $CaSO_4$ deposit mass, when sufficient, does not significantly affect the mode of degradation during bi-thermal testing. This is a logical conclusion because $CaSO_4$-induced degradation takes place through solid state reactions between the deposit and thermally grown oxides at the deposit-alloy interface; therefore, any amount of built-up deposit not in contact with the alloy cannot affect the reaction. However, the results for the 1- and 8-h coupons exposed with 5 $\frac{mg}{cm^2}$ of $CaSO_4$ do show that there is a relationship between the deposit mass and the duration of the initiation stage. Internal oxidation was present in the coupon having a 1-h initiation-stage but not in the coupon exposed with an 8-h initiation stage. The most likely reason for this is that 5 $\frac{mg}{cm^2}$ of deposit is fully consumed before the end of the 8-h initiation stage so the accelerated consumption of Al ceases prior to the temperature dropping to 925°C for the propagation stage. Presumably, without the continued formation of $CaAl_2O_4$ accelerating the consumption of Al from the alloy subsurface, an Al_2O_3 scale is able to establish which allows more Al to accumulate in the subsurface and better protects the alloy from internal oxidation.

8.4 Influence of Propagation Stage Temperature on the Susceptibility of N5 and N500 to Internal Attack

Figures 8.10 and 8.11 present representative cross-sectional images of N5 and N500 from the set of bi-thermal exposures in air + 30% steam outlined in Fig. 8.3, *i.e.*, 96-h propagation-stage temperatures of 704, 816, 925, 1038, and 1150°C. Each coupon was cross-sectioned three times

to ensure that an accurate and representative assessment of the reaction product could be made. Apart from the 1150°C exposure (which represents an isothermal exposure), the general morphology of the corrosion products observed in both alloys is found to have two distinct regions. The outermost part of the reaction product is an external layer comprised of a mix of oxides and calcium aluminates. This region has the characteristics of the product formed during the 1150°C initiation stage. Below the external layer is the internal oxidation zone that developed during the propagation stage. It was observed that the inner-layer morphology varies with propagation-stage temperature. At 704°C a broad front of what is presumed to be nickel-aluminum spinel formation developed with no evidence of enhanced internal oxidation. The coupons exposed with propagation-stage temperatures of 816°C and 925°C exhibited extensive internal oxidation with the characteristic morphology of $CaSO_4$-induced internal oxidation observed in lab-scale tests and field-exposed components (*e.g.*, Fig. 7.3). At a propagation-stage temperature of 1038°C there was also extensive internal oxidation; however, the morphology of the IOZ was significantly different from that formed at 816°C and 925°C. At 1038°C, the internal oxidation zone is stratified horizontally with alternating layers of mixed aluminum-rich oxide and highly depleted γ-Ni with discontinuous internal oxide precipitates. Finally, when the propagation stage temperature was 1150°C, in regions where the external product had not spalled, Al_2O_3 scale was observed at the oxidation front and there was no evidence of internal oxidation.

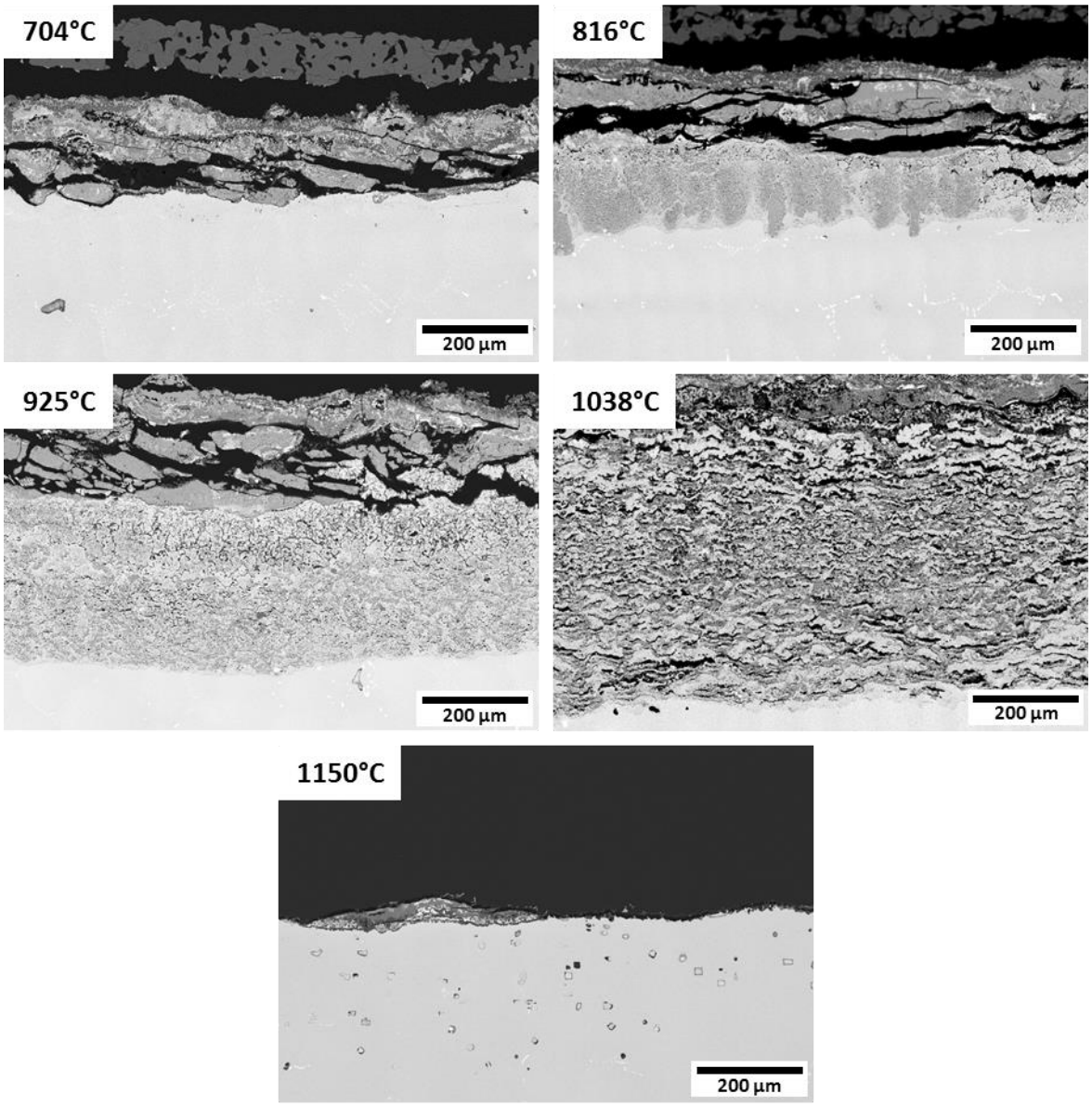

Figure 8-10. Cross-sectional images of $CaSO_4$-induced corrosion morphology developed in alloy N5 after bi-thermal exposure with a propagation stage temperature of 704, 816, 925, 1038, and 1150°C.

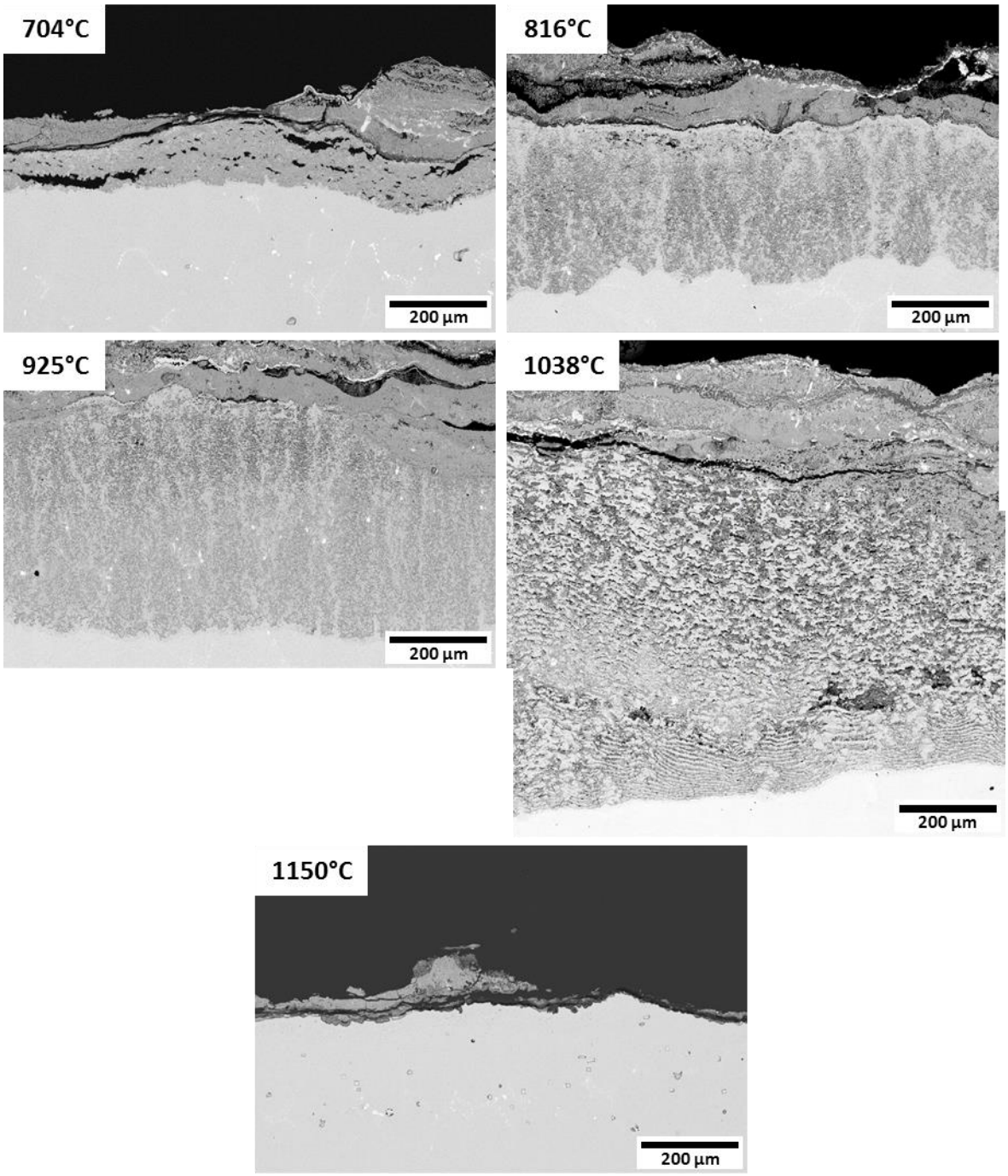

Figure 8-11. Cross-sectional images of $CaSO_4$-induced corrosion morphology developed in alloy N500 after bi-thermal exposure with a propagation stage temperature of 704, 816, 925, 1038, and 1150°C.

The maximum sound metal attack, measured as the depth of oxidation from the original metal surface, was recorded for each propagation-stage temperature in both alloys. For N5, the maximum sound metal attack depth for each propagation-stage temperature was 105.6 μm for 704°C, 205.4 μm for 816°C, 401.4 μm for 925°C, 434.0 μm for 1038°C, and 120.2 μm for 1150°C. For N500, the maximum sound metal attack depth for each propagation stage temperature was 145.5 μm for 704°C, 323.5 μm for 816°C, 492.0 μm for 925°C, 617.9 μm for 1038°C, and 258.8 μm for 1150°C. These results are summarized in Fig. 8.12. The maximum sound metal attack is seen to increase with propagation-stage temperature between 704-1038°C and then decrease as the temperature increases from 1038°C to 1150°C. Additionally, the maximum internal zone thickness for N5 was measured to be 193 μm at 816°C, 484 μm at 925°C, and 621 μm at 1038°C. The maximum internal zone thickness for N500 was measured to be 393 μm for 816°C, 598 μm for 925°C, and 886 μm for 1038°C.

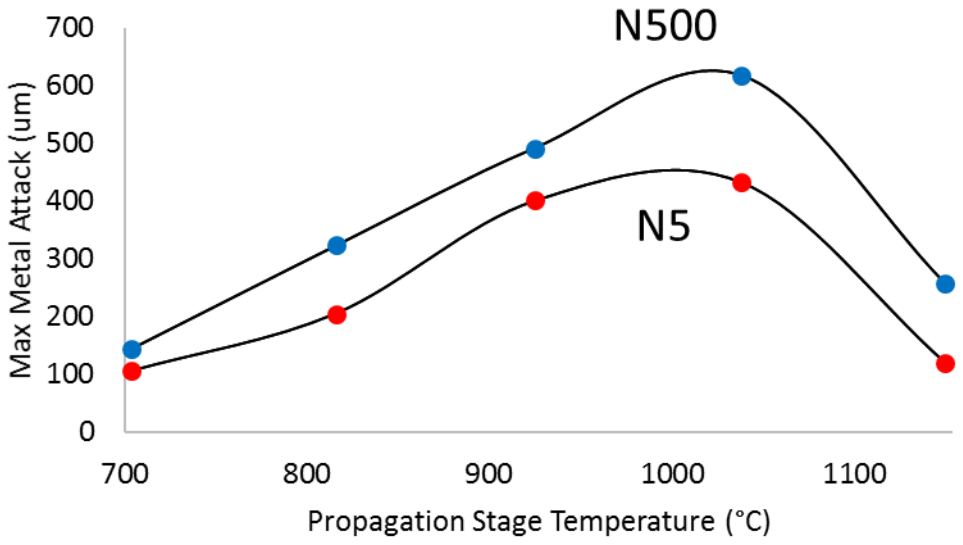

Figure 8-12. Maximum metal recession as a function of propagation stage temperature.

The trend for the maximum metal recession depth as a function of temperature can be explained by considering the kinetic competition between internal aluminum oxidation and the establishment of an Al_2O_3 scale. We know from section 2.2.2 and equation 2.13 that the rate of internal oxidation increases with increasing temperature due to increasing D_O. However, as reviewed in section 2.2.3 and in equation 2.21, $N_{Al}^{*,establish}$ is proportional $\frac{D_O}{D_{Al}}$ which decreases with increasing temperature. Therefore, it is expected that the rate of internal oxidation should increase with propagation-stage temperature until a critical temperature is reached at which Al_2O_3 formation is kinetically favored. This "critical" propagation stage temperature is evidently near 1038°C in alloys N5 and N500 under these experimental conditions.

A kinetic analysis was done using measurements of the maximum depth of sound metal attack in alloys N5 and N500 to develop expressions for the rate of sound metal attack in the alloys as a function propagation stage temperature between 816°C and 1038°C (the temperatures where internal oxidation occurred) after an 8-h 1150°C initiation stage. The maximum sound metal attack depth was used to calculate a parabolic rate constant for the maximum sound metal attack (k_a) for N5 and N500 for propagation stage temperatures of 816°C, 925°C, and 1038°C. Plotting $\ln(k_a)$ versus (1/T) (Fig. 8.13) allows an expressions of k_a values for N5 and N500 to be derived. These expressions are shown in equations 8.6 and 8.7. It is unknown how these expressions would change with varying 1150°C initiation stage duration.

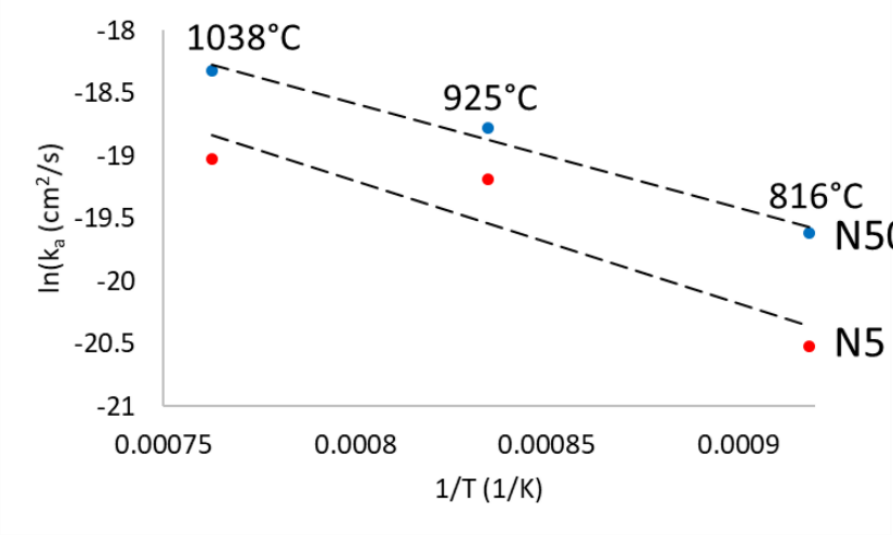

Figure 8-13. Plot of ln(k_a) vs (1/T) where k_a is the parabolic rate constant for maximum sound metal attack.

$$k_a^{N5}\left(\frac{cm^2}{s}\right) = 1.158 \times 10^{-5}\, exp\left(\frac{-81.42\frac{kJ}{mol}}{RT}\right) \tag{8.6}$$

$$k_a^{N500}\left(\frac{cm^2}{s}\right) = 6.879 \times 10^{-6}\, exp\left(\frac{-69.57\frac{kJ}{mol}}{RT}\right) \tag{8.7}$$

A second kinetic analysis was done to compare the internal oxidation rate of N5 and N500 during $CaSO_4$-induced internal oxidation in bi-thermal testing to the internal oxidation rate of Ni-8Al (at%) from the literature [101]. Similarly to the previous analysis with the maximum sound metal attack depth, the maximum internal oxidation zone thickness measurements from the bi-thermal testing were used to calculate the rate constant (k_p^{IOZ}) for internal oxidation at 816°C, 925°C, and 1038°C. These values were then compared to the values of the internal oxidation rate

constants at 800°C, 1000°C, and 1100°C for Ni-8Al calculated from the data of Martinez-Villafane et al. [101] using a plot of ln(k_p^{IOZ}) versus (1/T). This plot is shown in Fig. 8.14. It is clear that the $CaSO_4$-induced internal oxidation rate of N5 and N500 is much greater than that of Ni-8Al undergoing internal oxidation in air. Additionally, the activation energies for the $CaSO_4$-induced internal oxidation rates of N5 and N500 are much lower than that for the internal oxidation of Ni-8Al in air.

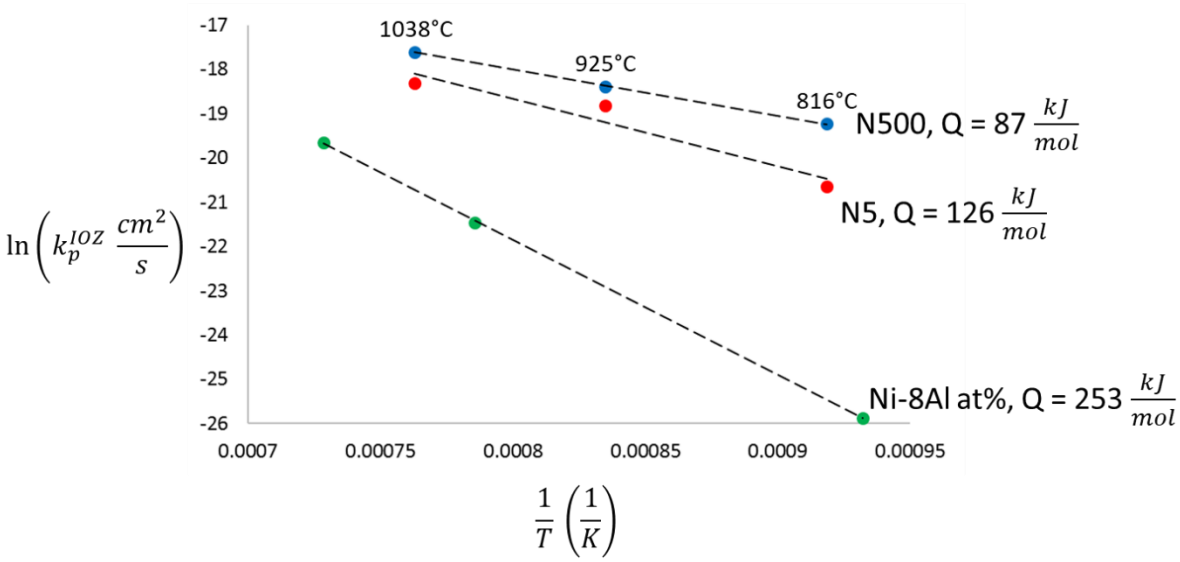

Figure 8-14. plot of ln(k_p^{IOZ}) versus (1/T) for the internal oxidation thickness of N5 and N500 formed during $CaSO_4$-induced internal oxidiaton and Ni-8Al (at%) from the literature [101].

It is known from equation 2.13 that internal oxidation rate and, therefore, the activation energy for internal oxidation, is largely dependent on the oxygen diffusivity in the alloy. It is possible that the $CaSO_4$-induced internal oxidation rate is larger than the internal oxidation rate of dilute Ni-Al alloys in air due to the microstructure of the internal oxidation precipitates formed during $CaSO_4$-induced internal oxidation. It is well known that, during the internal oxidation of

Ni-Al in air, the boundaries between the rod-like oxide precipitates and the metal matrix act as fast diffusion paths for oxygen resulting in an increase in the effective oxygen diffusivity in the alloy [35, 101, 102]. The TEM analysis of the internal oxidation product formed by $CaSO_4$-induced degradation revealed that the internal oxidation product was very fine grained (*cf.* Figs. 5.5 and 5.7). This fine structure could possibly result in an increase in the volume of short circuit diffusion paths available for oxygen diffusion into the alloy. This may explain the larger oxidation rate and lower activation for $CaSO_4$-induced internal oxidation compared to the internal oxidation of dilute Ni-Al alloys in air.

The transition between the dendrite-like internal oxidation morphology observed at propagation-stage temperatures between 816°C and 925°C and the stratified morphology observed at 1038°C is also likely a result of the kinetic competition between internal and external oxidation. Higher magnification images of the internal oxidation fronts from N500 coupons exposed with a propagation-stage temperature of 871°C and 1038°C are presented in Fig. 8.15 to highlight the difference in morphology.

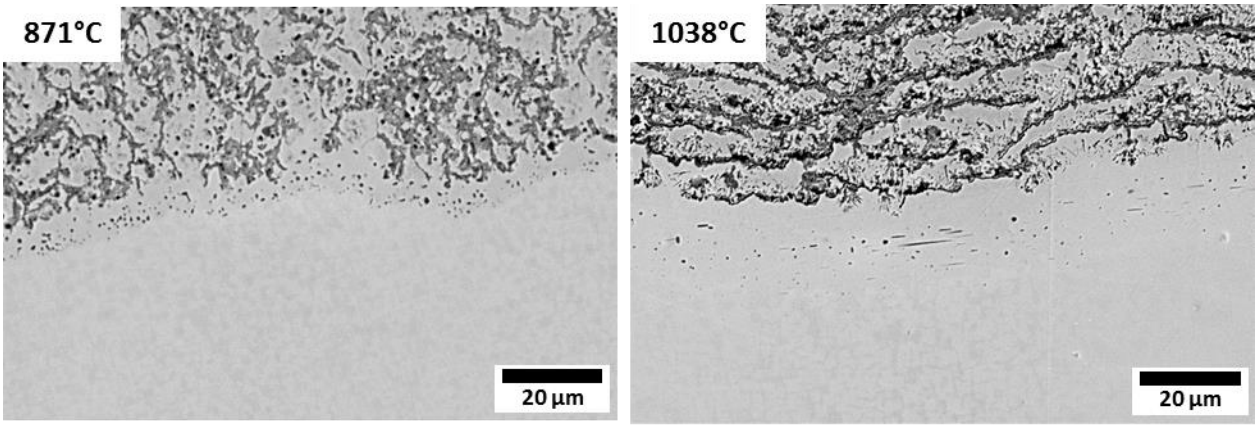

Figure 8-15. Higher magnification images of the internal oxidation front for N500 coupons exposed to bi-thermal exposures with a propagation stage temperature of 871°C and 1038°C.

Internal oxide-band formation parallel to the alloy surface has been reported and reviewed before in Ag- and Cu-based alloys [103, 104]. Bosch et al. [105] observed that the internal oxidation zone in Ag-Mg consisted of a thick precipitate-free zone below the alloy surface and above a continuous or semi-continuous network of magnesium oxide bands. The authors rationalized this morphology by proposing that reaction between Mg and O does not occur at a sharp interface where the activity product $a_{Mg}a_O$ for MgO formation is satisfied; rather, a thick region supersaturated with Mg and O develops and, when the supersaturation reaches a critical level, MgO nucleates and grows rapidly to form internal films to relieve the supersaturation. It is postulated that the formation of the Al-rich oxide bands in the present study develops by a different method because there were no signs of oxygen or aluminum supersaturation in the coupons. This is evident by the formation of internal oxide precipitates between the oxide bands and the presence of a γ'-denuded zone ahead of the internal oxidation front.

We propose a non-equilibrium mechanism for the observed oxide band formation which is dependent on the kinetic boundary between internal oxidation and Al_2O_3 scale formation. Our proposed mechanism for this process is shown in Fig. 8.16.

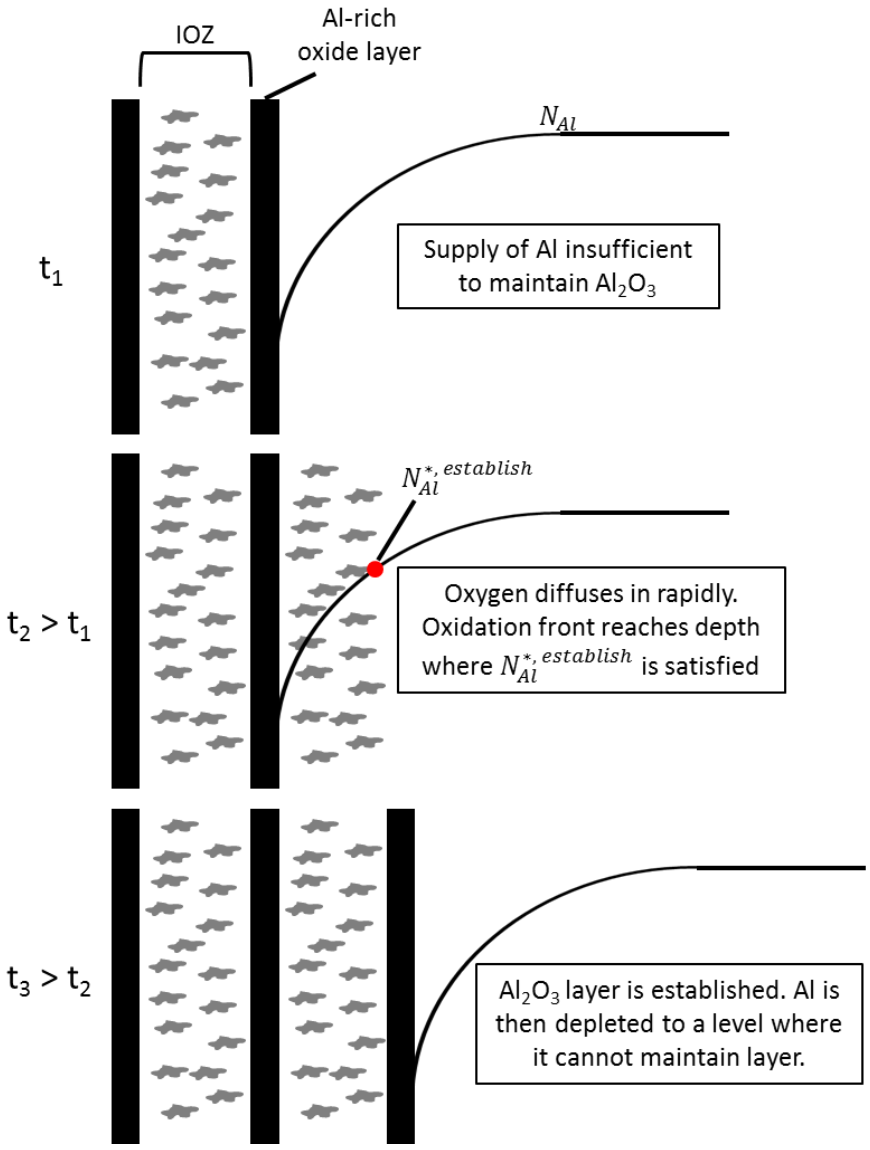

Figure 8-16. Proposed mechanism for oxide band formation at a propagation stage temperature of 1038°C.

After an oxide band has formed at the internal oxidation front, the alloy is unable to supply the flux of aluminum required to maintain the growth of the oxide layer *i.e.* $N_{Al}^{*,maintain}$ from equation 2.23 is not satisfied. Consequently, scale breakdown occurs and oxygen penetrates the layer to form internal oxide precipitates beneath the layer. After a given period, the internal oxidation front advances into the alloy and reaches a point where the concentration of aluminum is high enough to satisfy $N_{Al}^{*,establish}$ (equation 2.21) and a new Al-rich oxide layer forms. As time continues and Al is consumed to supply this layer, the concentration of Al in the sub-scale region drops below $N_{Al}^{*,maintain}$ and the process begins again. This mechanism would only be possible at temperatures very close to the critical temperature between internal oxidation and external scaling where the difference between $N_{Al}^{*,establish}$ and $N_{Al}^{*,maintain}$ becomes very small. Figure 8.17 shows a plot of the temperature dependent variables in the equations that define $N_{Al}^{*,establish}$ (equation 2.21) and $N_{Al}^{*,maintain}$ (equation 2.23) to demonstrate the relationship between the two. As temperature increases, both N_{Al}^{*} approach each other which would facilitate the transition between internal and external oxidation as described above. At lower propagation stage temperatures (*i.e.* between 816°C and 925°C) the difference between the two N_{Al}^{*} is too great for the toggling to occur. At high propagation-stage temperatures, such as 1150°C, the subsurface concentration never drops below either N_{Al}^{*} and no internal oxidation can initiate or propagate.

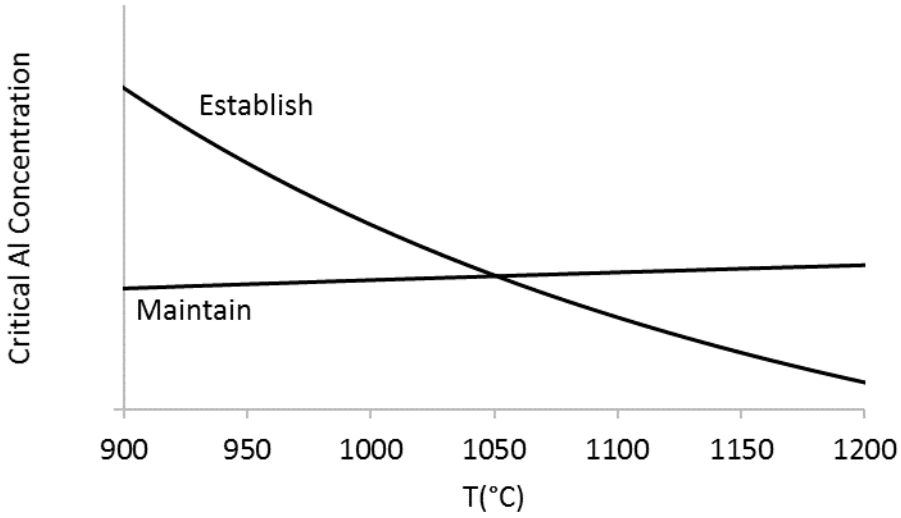

Figure 8-17. A schematic plot of the temperature dependent variables for N_{Al}^{*}. Please note that the temperature values are artificial because none of the constants were included in the calculation.

8.5 Conclusions

The systematic experiments investigating the influence of the 1150°C initiation-stage duration on the susceptibility of N5 and N500 to internal oxidation show that the susceptibility to internal oxidation is likely linked to how resulting subsurface microstructural changes affect the propensity for spallation and extent of subsurface depletion. For alloy N500, the degradation became more severe with initiation time up to at least 8 h but no internal oxidation was observed in the 24-h coupon. The increased susceptibility between 0 and 8 h of initiation-stage duration was attributed to the extent of aluminum and chromium depletion increasing with initiation-stage duration and the Al-rich oxide product being susceptible to cracking and spalling on cooling due to scale embrittlement caused by S enrichment and the development of large growth and thermal stresses. The reason why susceptibility to attack is lower after a 24-h exposure requires further

study but, it was shown that the subsurface depleted alloy is still susceptible to internal oxidation if the external product is removed after the 24-h initiation stage. Speculatively, the susceptibility to internal attack could be decreased by stress relaxation in the scale via cracking before cooling to 871°C. In this case, the alloy could re-establish an Al_2O_3 scale containing less accumulated strain energy that is less likely to spall on cooling.

With regard to the influence of $CaSO_4$ deposit mass, it was determined that the initial $CaSO_4$ deposit mass has little effect on the rate and mode of $CaSO_4$-induced internal oxidation. Because $CaSO_4$-induced degradation is a solid-state mode of attack, built-up $CaSO_4$ above the $CaSO_4$-reaction product interface cannot cause reaction. However, there is a critical amount of deposit necessary to cause degradation. In the N500 coupons exposed for a 1- or 8-h 1150°C initiation stage with 5 $\frac{mg}{cm^2}$ of $CaSO_4$, no internal oxidation occurred in the 8-h coupon while it did occur in the 1-h coupon. Because deposit mass does not affect the rate or mode of degradation, the most likely explanation for this observation is that 5 $\frac{mg}{cm^2}$ deposit was fully consumed before the end of the 8-h initiation stage which would end the accelerated consumption of Al from the alloy subsurface. This would allow the formation of a thicker and slower growing Al_2O_3 scale and lower the extent of depletion of Al in the subsurface.

The last topic addressed in this chapter was determining how propagation-stage temperature influenced the oxidation behavior of N5 and N500. The results showed that the mode and rate of degradation during the propagation-stage is directly linked to the kinetic competition between internal and external oxidation of aluminum. At 704°C, no internal oxidation occurred and the overall depth of attack was low. This was attributed to the temperature being too low for significant internal oxidation to occur. Internal oxidation was observed for propagation-stage temperatures between 816°C and 1038°C and the maximum attack depth increased with

temperature. In this temperature range, there is sufficient thermal activation for the inward diffusion of oxygen to cause significant internal oxidation while the diffusion of aluminum to the oxidation front is insufficient to form a protective Al_2O_3 scale. For the isothermal exposure at 1150°C, no internal oxidation occurred and the maximum attack depth in both alloys was much lower than the coupons exposed between 816° and 1038°C. Comparing influence of temperature on the rate of internal oxidation and on $N_{Al}^{*,establish}$ reveals that the degradation should increase with propagation stage temperature until a critical temperature is reached at which $Al_2 O_3$ can be established.

9.0 Influence of Alloy Composition on Susceptibility of Nickel-Based Superalloys to $CaSO_4$-Induced Internal Oxidation

The examination of field-exposed components and the results of lab-scale bi-thermal experiments have consistently shown that alloy N5 is more resistant to $CaSO_4$-induced internal oxidation attack than alloy N500 (see Fig 8.12). Developing an understanding of the reasons why N5 is more resistant than N500 was important because such an understanding could improve the alloy design and selection process for high-pressure turbine components that may be subjected to $CaSO_4$-induced attack. Comparing the composition of the two alloys, as well as an alloy called N500(Hi Cr) with the base composition of N500 but with the higher Cr content of N5, in Table 9.1 shows significant differences in the Cr, W, Re, and Y concentration between N5 and N500.

Table 9-1. Composition of alloys N5 and N500.

At%	Ni	Cr	Co	Al	Mo	W	Ta	Re	Hf	Y
N5	Bal	8.1	7.7	13.8	0.9	1.6	2.2	1.0	0.1	0.01
N500 (Hi-Cr)	Bal	8.1	7.6	13.9	0.9	2.0	2.1	-	0.1	0.03
N500	Bal	6.9	7.6	13.9	0.9	2.0	2.1	-	0.1	0.03

The differences of the Cr and Re contents between the alloys were of the greatest interest for further study regarding their influence on degradation resistance. The strong link between Cr content and the oxidation behavior of Al_2O_3-forming nickel-based alloys is well established (see section 2.2.3.1) while the influence of Re on the oxidation behavior of superalloys is poorly understood and of interest to engine manufacturers due to the desire to reduce the use of the expensive element Re [106]. With regard to W and Y, it is possible that the higher content of these

elements in N500 may play a role in causing poorer resistance to $CaSO_4$-induced degradation; however, this is postulated to be rather unlikely. Indeed, refractory alloying elements, including W, can have a deleterious effect on the oxidation behavior of Al_2O_3-forming alloys in two ways [107]. The first is that adding a large amount of refractory elements to an alloy may significantly slow the diffusivity of aluminum in the alloy. The second is that refractory oxides generally are non-protective and can therefore be detrimental to the integrity of an external scale if incorporated into the product during oxidation. However, a recent publication investigated the influence of W on the oxidation rate of superalloys and showed that a difference of 0.4 at% W would likely have little, if any, effect on the oxidation behavior of N5 and N500 [108]. A higher concentration of the reactive element yttrium in N500 may be detrimental to the oxidation behavior if the alloy was over-doped. Over-doping with Y can result in the formation of oversized Y_2O_3 oxide pegs at the scale-alloy interface which act as stress concentration points during thermal cycling and can lead to scale spallation [109, 110]. However, no such oversized pegs were observed in any N5 and N500 coupons examined in this research, so it is unlikely that either of the alloys are over-doped with Y.

9.1 Experimental Procedure

The influence of Cr and Re contents on the $CaSO_4$-induced degradation resistance of N5 and N500 was investigated with two sets of experiments using model alloys. The first set of experiments provided insights into the role of both Cr and Re. To accomplish this, coupons of the model alloy N500(Hi Cr) were produced and exposed to a bi-thermal exposure with conditions

shown in Fig 9.1. The resulting cross-sectional images were compared to N5 and N500 coupons previously exposed under the same experimental conditions (see Fig. 7.3).

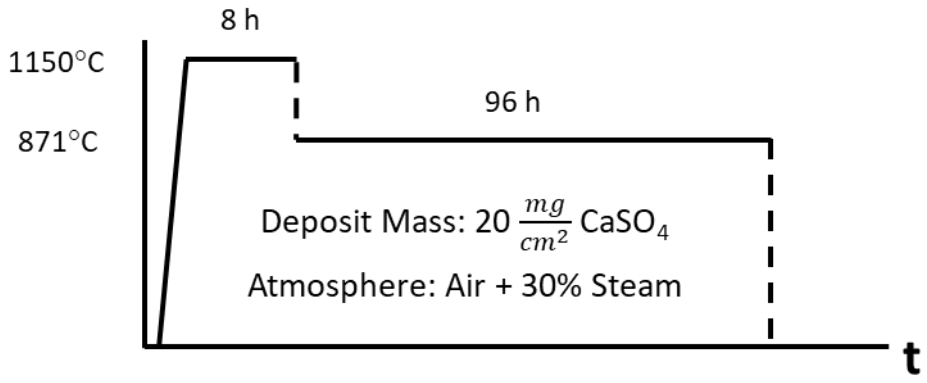

Figure 9-1. Conditions of the bi-thermal exposure conducted to evaluate the influence of Cr and Re content on CaSO4-induced corrosion resistance of 2nd generation superalloys.

The second set of experiments isolated the influence of Re on the internal oxidation behavior of nickel-based alloys by exposing model NiCrAlRe alloys in air at 1000°C for 24 h. Single-phase γ-Ni alloys with the composition Ni-6.5Al-3.5Cr-0, 1, 3Re at% were cast by argon-arc melting 99.995% Ni, 99.999% Al, 99.95% Cr, and 99.9% Re pieces together. Each casting was re-melted three times to eliminate chemical segregation in the alloys. The base Ni-Al-Cr composition was chosen so that the alloys would internally oxidize during exposure in air at 1000°C while maintaining an Al:Cr ratio similar to that of alloys N5 and N500. This composition facilitates the study of rhenium's influence on the internal oxidation of nickel-based alloys under simplified conditions that remove the complexities of how the bi-thermal exposure with $CaSO_4$ deposit sensitizes the alloys to internal oxidation.

9.2 Results

Cross-sectional images from N5, N500, and N500(Hi Cr) coupons exposed to the bi-thermal exposure conditions in Fig. 9.1 are shown in Fig 9.2. The average internal-oxidation zone depth from 100 measurements in each coupon were 303 ± 57 μm for N5, 418 ± 42 μm for N500 and 406 ± 58 μm for N500(Hi Cr). Additionally, higher magnification images of the internal oxide precipitates shown in Fig. 9.3 reveal that the internal oxide precipitates in N500 and N500(Hi Cr) have a similar "wispy" morphology while the precipitates were more globular in N5. Therefore, the addition of 1.2 at% Cr to alloy N500 does not have as significant an effect on the resistance to $CaSO_4$-induced internal oxidation as Re.

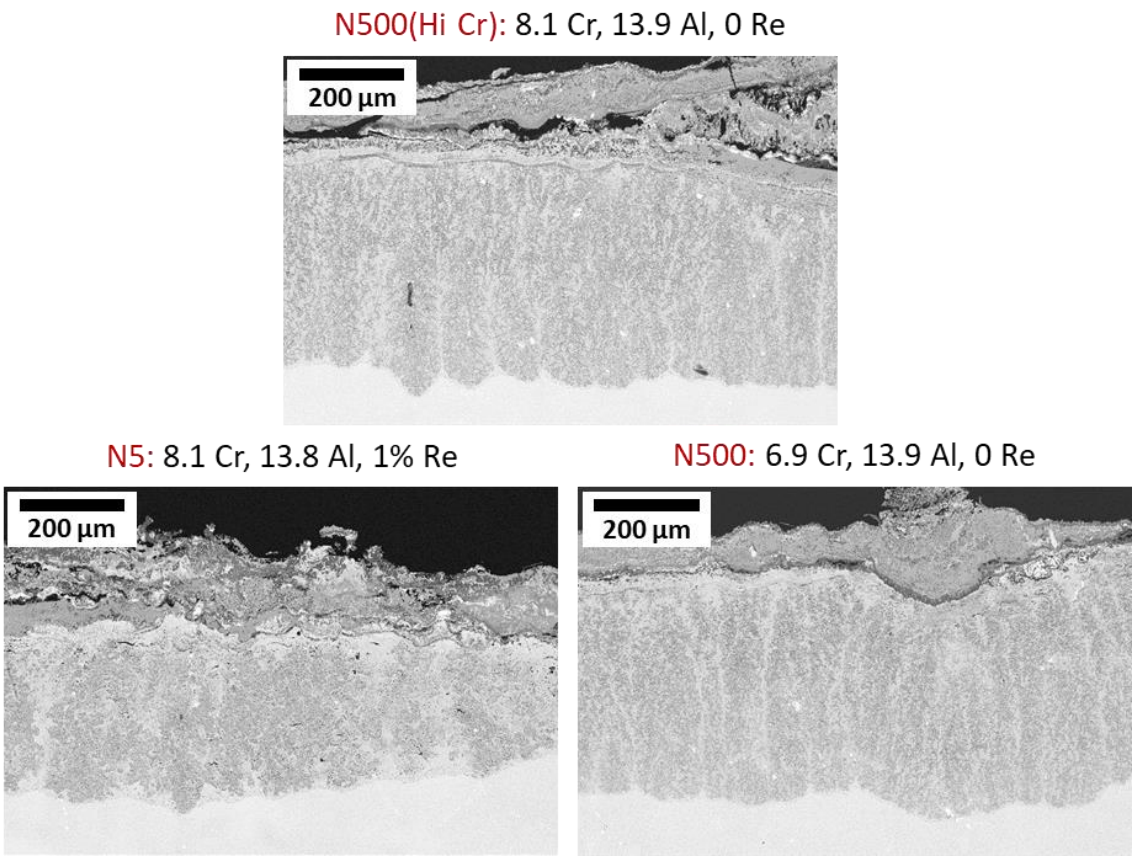

Figure 9-2. Cross-sectional SEM micrographs of N500(Hi Cr), N5, and N500 exposed to the experiment shown in Fig. 9.1. The Cr, Al, and Re content of the alloys in at% are listed above the image of the coupons.

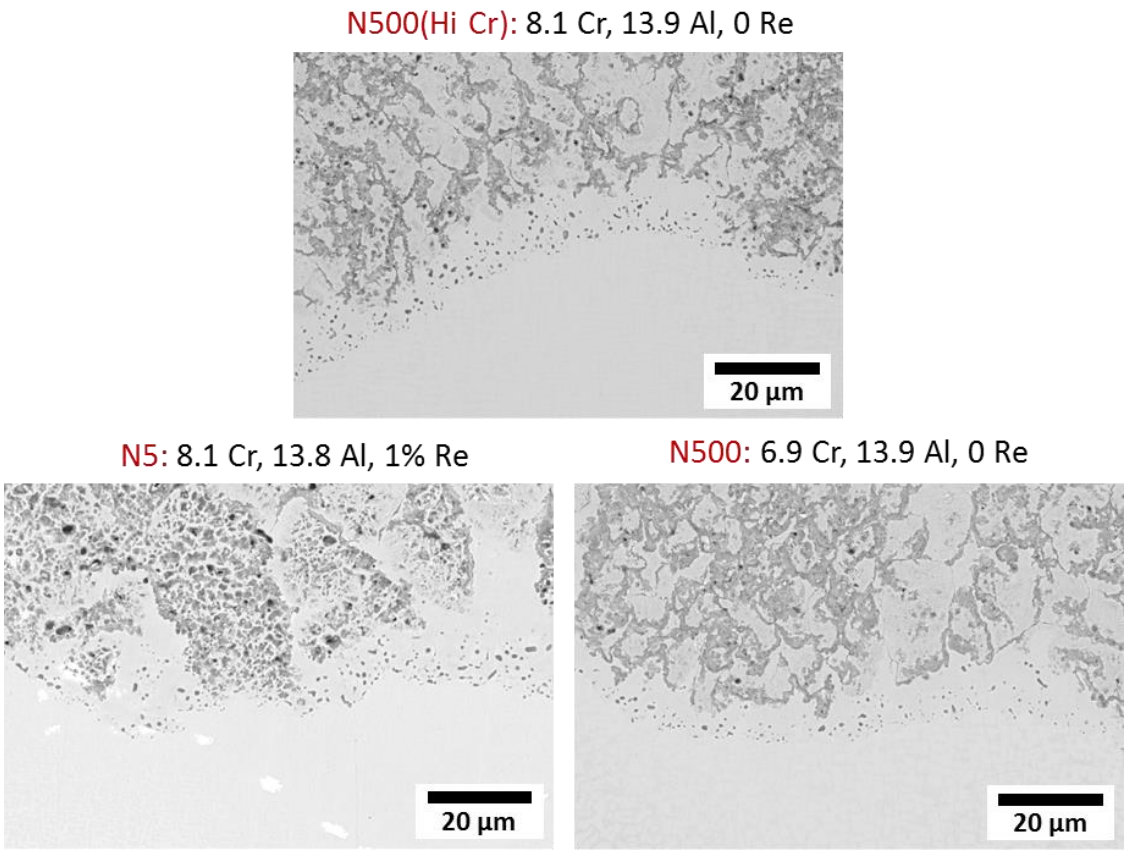

Figure 9-3. High magnification images of N500(Hi Cr), N5, and N500 which show internal oxide precipitate morphology.

Stitched SEM images of the model Ni-6.5Al-3.5Cr-0, 1, 3Re alloys after 24 h of exposure at 1000°C in air are shown in Fig 9.4. The 0-Re alloy exhibited internal oxidation across the entire surface of the alloy. The 1-Re alloy exhibited internal oxidation over a majority of the alloy surface, but, in some areas, external Al_2O_3 scale was present. The 3-Re alloy had formed an external Al_2O_3 scale over nearly the entire alloy surface with only isolated NiO nodule formation and internal oxidation. Where formed, the internal oxidation zone depth is 65.9 ± 0.9 µm for the 0-Re alloy, 70.7 ± 1.2 µm in the 1-Re alloy. The presence of grain boundaries appears to have a significant effect on the oxidation behavior of the alloys. In the 0-Re alloy, the depth of internal oxidation was less around grain boundaries and the areas which formed Al_2O_3 scale on the 1-Re

alloy are associated with areas where grain boundaries meet the surface of the alloy. This suggests that the more rapid supply of Al to the surface in these areas is enough to favor external oxidation over internal oxidation in the 1-Re alloy. The images of the degradation in Fig. 9.5 better show the assemblage of the product formed on the alloys and areas on the 1-Re and 3-Re alloys where external Al_2O_3 formed. More detailed examination of the internal oxidation zone in 0-Re and 1-Re revealed that rhenium had little effect on the morphology and depth of the internal oxidation zone. The volume fraction of oxide precipitates in the bottom 40 μm of the IOZ measured by color threshold analysis was 29-32% in 0-Re and 28-34% in 1-Re. The internal oxide precipitate spacing was 0.99 $\frac{precipitate}{\mu m}$ in 0-Re and 0.96 $\frac{precipitate}{\mu m}$ for 1-Re. The assemblage of the IOZ in these alloys is similar to that described by Hindam and Whittle [35]. There is external NiO above an internal oxidation zone consisting of two regions of rod-like internal oxide precipitates. The first region of the IOZ is γ-Ni + $NiAl_2O_4$ and the second is γ-Ni + Al_2O_3.

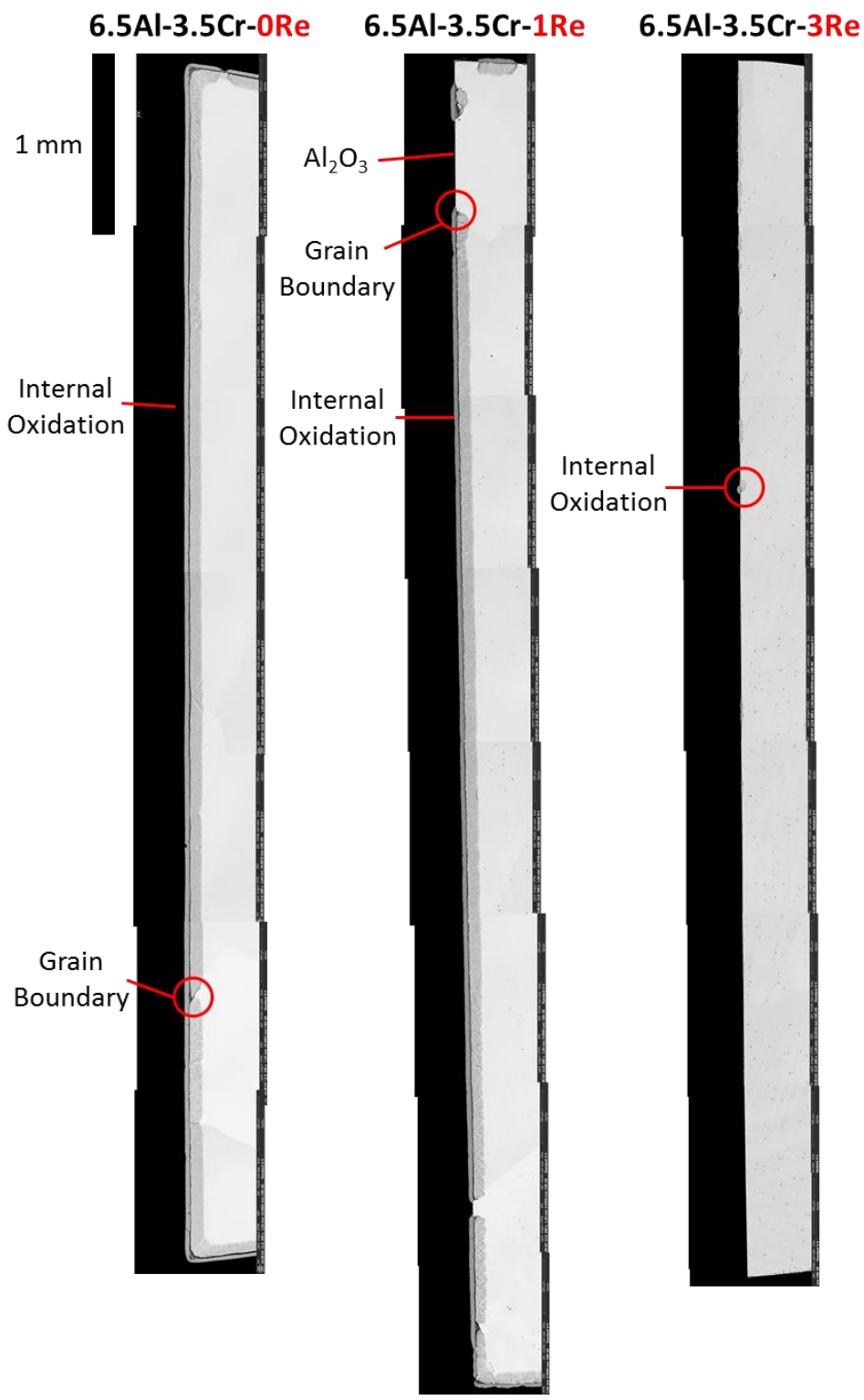

Figure 9-4. Macroscopic images of Ni-6.5 Al-3.5 Cr-0, 1, or 3Re exposed for 24 h at 1000°C.

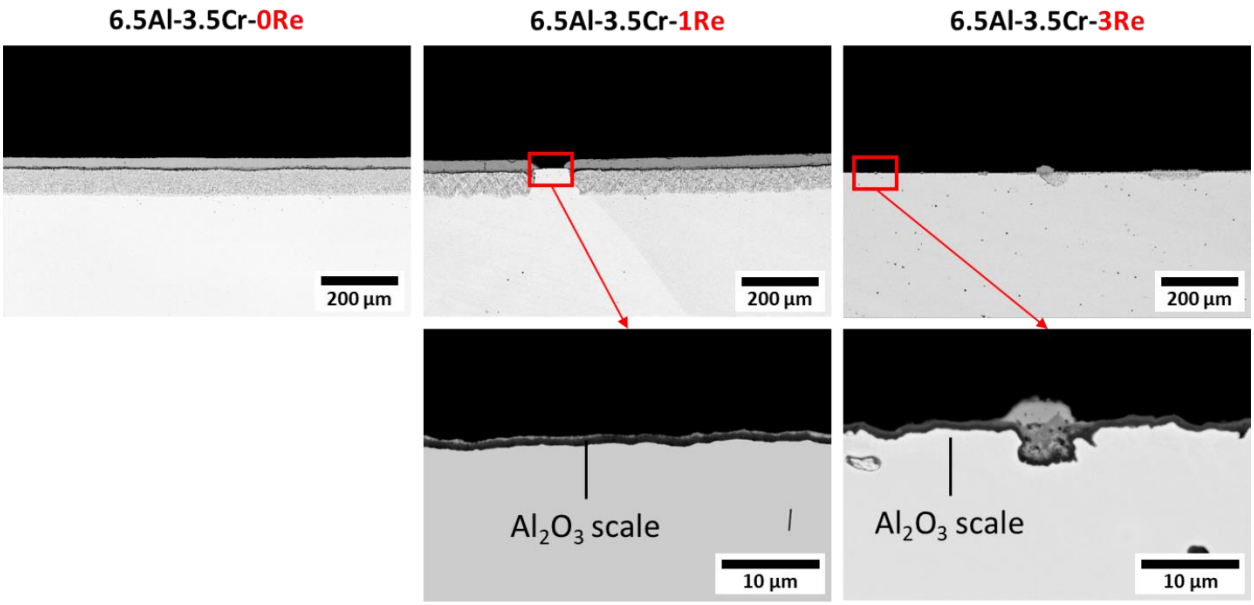

Figure 9-5. Higher magnification images of internal oxidation and areas with Al_2O_3 formation in the model Ni-Al-Cr-Re alloys.

9.3 Discussion

The beneficial effect of Re on the transition between internal and external oxidation must be linked to decreasing one or both of the N_{Al}^{*} for the establishment (equation 2.21) and maintenance (equation 2.23) of an Al_2O_3 scale. Hints as to how Re is beneficial to this transition can be gained by considering how the addition of Re could affect the variables in these equations.

$$N_{Al}^{*,establish} = \left[\frac{\pi g^{*}}{3} N_{O}^{(S)} \frac{D_O V_m}{D_{Al} V_{ox}}\right] \tag{2.21}$$

$$N_{Al}^{*,maintain} = \frac{V_m}{48}\left(\frac{\pi k_p}{D_{Al}}\right)^{1/2} \tag{2.23}$$

Because the internal oxidation zone depth in the 0- and 1-Re alloys are very similar, it is unlikely that Re has a strong influence on the oxygen permeability ($N_O^{(S)} D_O$) in the model alloys. Additionally, the similarity in the volume fraction of oxide precipitates and oxide particle spacing in the IOZ means that it is unlikely that Re is significantly affecting g^* (the critical volume fraction of oxide required to form a continuous Al_2O_3 scale). Eliminating, these variables leaves the possibility that the enhanced oxidation resistance in the 1- and 3-Re alloy is related to the effect of Re on growth rate of the Al_2O_3 scale formed on NiAlCrRe alloys (k_p) or the diffusivity of aluminum in the alloys.

Currently, there is a paucity of literature which investigates the effect of Re addition on the rate of Al_2O_3 scale growth. There have been studies that report the influence of rhenium on the Al_2O_3 scaling behavior in superalloys; however, they give an unclear picture. Specifically, some papers have reported that the addition of Re improves the oxidation resistance of superalloys by improving Al_2O_3 tenacity and lowering Al_2O_3 growth rate [111, 112] while another reports that Re increases the oxidation rate of Al_2O_3-forming superalloys by promoting the formation of spinel oxides on alloys with significant micro-segregation between the dendritic and inter-dendritic regions [113].

With respect to the effect of Re additions on D_{Al}, a study published by Zeng et al. measured the influence of Re on the diffusivity of aluminum in nickel [114]. The authors added 1, 2, or 3 Re to Ni-5.3Al (wt%) and found that increasing Re results in an increase in the activation energy for Al diffusion but also an increase in the pre-exponential factor. This means that Re may boost Al diffusion at higher temperatures. According to these measurements (see equations 9.1-9.3), D_{Al}^{3Re} becomes larger than D_{Al}^{1Re} at temperatures above 1085°C.

$$D_{Al}^{1Re}\left(\frac{m^2}{s}\right) = 1.4x10^{-5}\exp\left(-\frac{230\,kJ/mol}{RT}\right) \quad (9.1)$$

$$D_{Al}^{2Re}\left(\frac{m^2}{s}\right) = 2.7x10^{-5}\exp\left(-\frac{238\,kJ/mol}{RT}\right) \quad (9.2)$$

$$D_{Al}^{3Re}\left(\frac{m^2}{s}\right) = 1.4x10^{-4}\exp\left(-\frac{256\,kJ/mol}{RT}\right) \quad (9.3)$$

9.4 Conclusions

The effect of alloy composition on the $CaSO_4$-induced degradation resistance of alloys N5 and N500 was found to be most strongly affected by Re content, specifically, that the addition of Re in alloy N5 improves the degradation resistance of the alloy. This was proved by comparing the degradation caused by $CaSO_4$-induced degradation during bi-thermal testing of N5, N500, to a model alloy, N500(Hi Cr). The results of this experiment showed that increasing the concentration of Cr in alloy N500 to match that of N5 did not significantly affect the depth and morphology of degradation that took place in the alloy.

Model Ni-6.5Al-3.5Cr-0, 1, or 3Re (at%) alloys were made to further study the influence of Re on the internal oxidation behavior of nickel-based alloys during exposure in air at 1000°C for 24 h. The results of the experiment showed that the addition of Re to Ni-6.5Al-3.5Cr decreases N_{Al}^{*} required for Al_2O_3 scale formation. Because the depth and morphology of the internal oxidation zones formed in the 0-Re and 1-Re alloys were unaffected by rhenium content, the most likely variables that Re can affect to decrease N_{Al}^{*} are the growth rate of Al_2O_3 scale (k_p) and the diffusivity of aluminum in nickel-based alloys. A survey of the literature does not provide a

conclusive description for the effect of Re on the growth rate of Al_2O_3 scale on Ni-based alloys [111–113]. However, it is possible that the addition of Re to Ni-Al increases the diffusivity of Al in the alloy at high temperatures [114]. A more fundamental study on the effect of rhenium on the oxidation behavior of Ni-based alloys lies outside of the bounds of this research but the authors believe that such a study would be a valid research endeavor for the application of improving superalloy design.

10.0 Summary

The goals of this research project were to provide the foundational understanding of CaO- and $CaSO_4$-induced degradation in aviation gas-turbine engines and to develop a lab-scale test procedure which accurately replicates the degradation observed in field-exposed N5 and N500 components. Characterizing the degradation observed in the field-exposed parts showed that N5 and N500 components with $CaSO_4$ deposit had experienced aggressive internal oxidation. Investigating the mode of degradation caused by CaO and $CaSO_4$ deposits on N5 and N500 at 900°C and 1150°C revealed that the most likely initiator for the degradation observed in the field-exposed parts was $CaSO_4$-induced degradation at 1150°C (roughly the maximum surface temperature that components reach during takeoff and climb). It was determined that $CaSO_4$ deposit can cause significant subsurface depletion of Al and Cr and enrichment in S through reaction between $CaSO_4$ and Al_2O_3 to form $Ca_4Al_6O_{16}S$ / $CaAl_2O_4$. It was put forward that the subsurface-depleted alloys were susceptible to internal oxidation when exposed to conditions that are detrimental to Al_2O_3 establishment and maintenance. These principles were used to design a lab-scale experiment that successfully reproduced the degradation observed in the field-exposed components by better simulating the exposure conditions in gas-turbine engines during flight.

The experimental procedure was developed while considering that, in service, the temperature of the components is variable and that there is steam present in the atmosphere due to the combustion process. During takeoff, the components can reach temperatures as high as 1150°C and then the temperature of the components decreases to temperatures between 600°C and 900°C during cruise [87]. Therefore, the experiment developed begins with an 8-h exposure at 1150°C and is followed by a 96-h exposure at 871°C. The atmosphere for the exposure is air + 30% steam.

With $CaSO_4$ deposit, $CaSO_4$-induced degradation will occur during the 1150°C exposure and cause the subsurface depletion of Al and Cr and enrichment in S. It is well known that it is more difficult to establish and maintain Al_2O_3 at lower temperatures [19, 50] in steam containing atmospheres [55]; therefore, internal oxidation initiates and propagates during the second stage of the exposure at 871°C. When the experiment was completed, internal oxidation matching that seen in the field-exposed components was observed. A time study was completed to observe the development of the reaction product and it was determined that the internal oxidation began early during the second stage of the bi-thermal exposure. After 1-h at 871°C localized areas of internal oxidation were observed where no external NiO + NiS_x was present. This suggested that the external scale must be compromised during the second stage of the exposure to expose the depleted subsurface to the oxidizing environment. The remainder of the research project was dedicated to determining how exposure environment, subsurface S enrichment, extent of $CaSO_4$-induced degradation with initiation time, propagation stage temperature, and alloy composition affect the mode of $CaSO_4$-induced degradation during bi-thermal testing.

It was determined that, for alloys N5 and N500, both a low temperature exposure after the initial 1150°C exposure and the presence of steam in the atmosphere are required for breakaway internal oxidation to occur. This is because a lower exposure temperature and the presence of steam in the atmosphere are conditions that are kinetically unfavorable to the establishment of Al_2O_3 scale. The subsurface enrichment of sulfur was also found to be required for internal oxidation to occur in the alloys during bi-thermal testing. When alloys are de-sulfurized in Ar + 5% H_2 after the initial 8-h exposure at 1150°C then subsequently subjected to the 871°C exposure in air + 30% steam, no internal oxidation is present. The influence sulfur is most likely tied to the removal of

Cr from the alloy subsurface due to the formation of CrS particles and the negative effect of S on the adherence of external oxide scales [88–93].

The systematic experiments done to investigate the effect of 1150°C initiation stage duration on the susceptibility of N5 and N500 to internal oxidation revealed that N5 is only susceptible to internal oxidation for an initiation stage duration of 8 h while the extent of internal oxidation observed in N500 increases with time up to 8 h. However, no internal oxidation was observed for an initiation stage duration of 24 h in either alloy. The increasing susceptibility to attack of N500 up to 8 h is most likely due to increased Al depletion with exposure time and increasing probability of scale spallation upon cooling to 871°C due to the accumulation of growth and thermal stresses in the external reaction product formed at 1150°C. The reason that N500 became less susceptible to internal attack after a longer 24 h initiation stage requires further investigation, but one possible reason is that accumulated stresses in the reaction product are relaxed by cracking at 1150°C. The reestablished oxide would therefore be less likely to crack on cooling.

The study on the effect of propagation stage temperature revealed that the mode and rate of degradation during the propagation stage is directly linked to the kinetics of internal oxidation and the transition between internal and external oxidation. At a propagation-stage temperature of 704°C, the maximum attack depth was low and no internal oxidation was observed. For propagation stage temperatures of 816°C, 925°C, and 1038°C internal oxidation occurred and the maximum attack depth increased with temperature due to increasing D_O in the alloy. However, because $\frac{D_O}{D_{Al}}$ decreases with increasing temperature due to a difference in activation energy for D_O and D_{Al}, for the isothermal exposure at 1150°C, no internal oxidation occurred because Al_2O_3 was be established and maintained at this high temperature. When comparing the maximum sound

metal attack in N5 and N500, for all temperatures, the maximum depth of attack in N5 was less than that of N500.

When comparing the composition of N5 and N500, the difference in Cr and Re content were of greatest interest for further study on the effect of alloy composition on the resistance of the alloys to $CaSO_4$-induced degradation. N5 has higher Cr and Re than N500. Experiments on a model alloy called N500(Hi Cr) with the composition of N500 but with the higher Cr content of N5 revealed that the difference in Cr content had little effect on the depth of attack and the morphology of the internal oxide precipitates. As such, the influence of Re became the primary focus. Model Ni-6.5Al-3.5Cr-0, 1, or 3Re alloys were cast to isolate the effect of Re on the internal oxidation behavior of NiAlCr. The base NiAlCr content chosen to be slightly subcritical (internally oxidizing) at 1000°C. When these alloys were exposed for 24 h at 1000°C in air, it was clear that the NiAlCrRe alloys were better able to establish and maintain Al_2O_3 with increasing Re content. The influence of Re on the oxidation behavior of Ni-based alloys is outside of the scope for this research but should be investigated further.

11.0 Future Work

The process of discovering how $CaSO_4$ deposits cause breakaway internal oxidation in nickel-based superalloys revealed two criteria that must be met for internal attack to occur. First, the alloy subsurface must be depleted of Al and Cr and enriched in S. Second, the subsurface depleted alloy must be exposed to an oxidizing environment where internal oxidation is kinetically favorable. Should these be valid assumptions, $CaSO_4$-induced internal oxidation through bi-thermal testing would only be a specific case of a more generalized mode of deposit-induced degradation. These assumptions were tested by conducting an experiment where the initiator for the subsurface depletion and S enrichment was type 1 hot corrosion caused by pure Na_2SO_4 deposit at 900°C (see section 2.3.1 for a review of type 1 hot corrosion).

The bi-thermal exposure in air + 30% steam with $20\frac{mg}{cm^2}$ of Na_2SO_4 deposit shown in Fig. 11.1. The initiation stage exposure was 8 h at 900°C followed by a 60-h propagation stage exposure at 871°C. It should be noted that 871°C is below the melting point of Na_2SO_4. Therefore, it was assumed that the development of the corrosion product during the propagation stage would not be influenced by any remaining liquid Na_2SO_4. The results of the experiment are shown in Fig. 11.2.

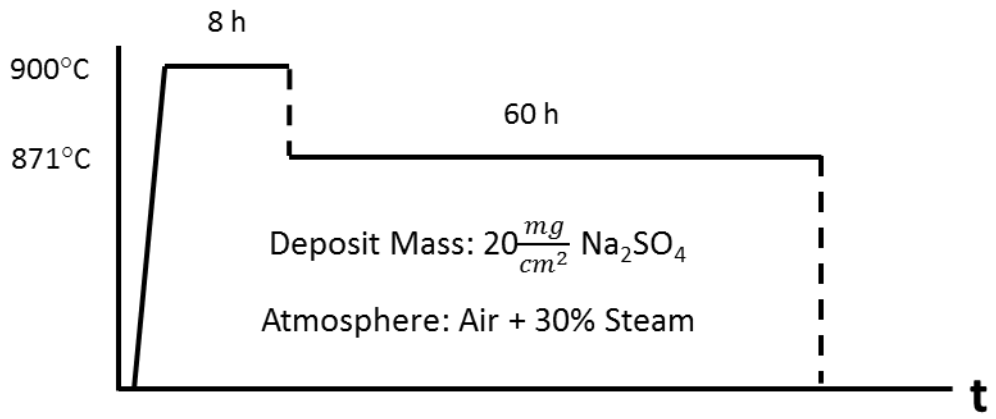

Figure 11-1. Experimental conditions for bi-thermal exposure with Na_2SO_4 deposit.

The reaction product formed shows the same three characteristic features that are present in the internal attack observed in the field-exposed components and in the bi-thermal exposures in air + 30% steam with $CaSO_4$ deposit. There is an external layer of Ni-rich oxide, the internal oxidation zone contains coarse Al- and Cr-rich oxide precipitates, and a fine distribution of CrS precipitates are present in the γ'-denuded zone ahead of the internal oxidation front.

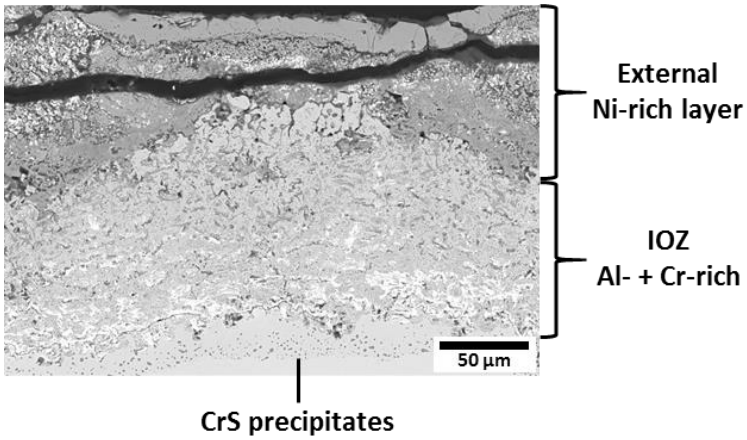

Figure 11-2. Reaction product formed from bi-thermal tests with Na2SO4 deposit.

The commonality of the characteristic features between internal oxidation initiated by $CaSO_4$-induced degradation at 1150°C and internal oxidation initiated by Na_2SO_4-induced degradation at 900°C shows that deposit-induced internal oxidation can be caused over a wide range of temperatures based on deposit composition. This means that components other than those that are exposed to the highest temperature in the gas-turbine environment with $CaSO_4$ could be susceptible to aggressive internal oxidation. Based on this, there is a need to develop a more comprehensive understanding of how subsurface depletion behavior affects the subsequent oxidation behavior of an alloy that has undergone deposit-induced degradation. Conducting such a study would allow engineers and alloy designers to predict which high pressure turbine components would be susceptible to deposit-induced internal oxidation based on the alloy composition, surface temperature range, and anticipated deposit composition during service.

Bibliography

[1] International Air Transport Association, “Airline Industry Economic Performance - 2018 End Year.” 2018.

[2] P. Spittle, “Gas turbine technology,” *Phys. Educ.*, vol. 38, no. 6, pp. 504–511, 2003.

[3] T. M. Pollock and S. Tin, “Nickel-Based Superalloys for Advanced Turbine Engines: Chemistry, Microstructure and Properties,” *J. Propuls. Power*, vol. 22, no. 2, pp. 361–374, 2006.

[4] R. Schafrik and R. Sprague, “Saga of Gas Turbine Materials Part III,” *Adv. Mater. Process.*, vol. 162, no. 5, pp. 29–33, 2004.

[5] International Air Transport Association Maintenance Cost Task Force, “Airline Maintenance Cost Executive Commentary.” 2017.

[6] B. Gleeson, “High-Temperature Corrosion of Metallic Alloys and Coatings,” in *Corrosion and environmental degradation*, 2000, p. 173.

[7] M. B. Krisak, B. I. Bentley, A. W. Phelps, and T. C. Radsick, “Review of Calcium Sulfate as an Alternative Cause of Hot Corrosion,” *J. Propuls. Power*, vol. 33, no. 3, pp. 697–703, 2017.

[8] R. A. Rapp, “Hot corrosion of materials: A fluxing mechanism?,” *Corros. Sci.*, vol. 44, no. 2, pp. 209–221, 2002.

[9] B. A. Pint, “High-temperature corrosion in fossil fuel power generation: Present and future,” *JOM*, vol. 65, no. 8, pp. 1024–1032, 2013.

[10] D. A. Shifler, “The Increasing Complexity of Hot Corrosion,” *J. Eng. Gas Turbines Power*, 2017.

[11] T. J. Nijdam and R. van Gestel, “Service experience with single crystal superalloys for high pressure turbine shrouds.” 2010.

[12] J. Stringer and A. J. Minchener, “High temperature corrosion in fluidized bed combustion systems,” *J. Mater. Energy Syst.*, vol. 7, no. 4, pp. 333–344, 1986.

[13] V. Nagarajan, R. D. Smith, and I. G. Wright, “Influence of solid-state CaS-CaO-CaSO4 deposits on corrosion of high-temperature alloys in simulated FBC environments,” *Oxid. Met.*, vol. 31, no. 3–4, pp. 325–340, 1989.

[14] K. T. Chiang, G. H. Meier, and R. A. Perkins, “The effects of deposits of CaO, CaSO4, and MgO on the oxidation of several Cr2O3-forming and Al2O3-forming alloys,” *J. Mater. Energy Syst.*, vol. 6, no. 2, pp. 71–86, 1984.

[15] R. Darolia, “Development of strong, oxidation and corrosion resistant nickel-based superalloys: critical review of challenges, progress and prospects,” *Int. Mater. Rev.*, vol. 64, no. 6, pp. 355–380, 2019.

[16] T. Massalski, *Binary Alloy Phase Diagrams*. American Society for Metals, 1986.

[17] G. Dieter, *Mechanical Metallurgy*, 3rd ed. McGraw-Hill, 1986.

[18] W. S. Walston, K. S. O’Hara, E. W. Ross, T. M. Pollock, and W. H. Murphy, “Rene’ N6: Third Generation Single Crystal Superalloy,” in *Superalloys*, 1996, pp. 27–34.

[19] C. S. Giggins and F. S. Pettit, “Oxidation of Ni-Cr-Al Alloys Between 1000° and 1200°C,” *J. Electrochem. Soc.*, vol. 118, no. 11, pp. 1782–1790, 1971.

[20] B. A. Pint, “Progress in Understanding the Reactive Element Effect Since the Whittle and Stringer Literature Review,” in *Proc. John Stringer Symposium on High Temperature Corrosion. Materials Park, Ohio: ASM International*, 2003, pp. 9–19.

[21] N. Birks, G. H. Meier, and F. S. Pettit, *Introduction To The High Temperature Oxidation of Metals*, 2nd ed. Cambridge University Press, 2006.

[22] C. Wagner, “Beitrag zur Theorie des Anlaufvorgangs,” *Zeitschrift für Phys. Chemie*, vol. 21, no. 1, pp. 25–41, 2017.

[23] A. Atkinson, “Wagner theory and short circuit diffusion,” *Mater. Sci. Technol.*, vol. 4, no. 12, pp. 1046–1051, 1988.

[24] B. A. Pint and K. B. Alexander, “Grain Boundary Segregation of Cation Dopants in a-Al2O3 Scales,” *J. Electrochem. Soc.*, vol. 145, no. 6, p. 1819, 1998.

[25] D. Naumenko, B. Gleeson, E. Wessel, L. Singheiser, and W. J. Quadakkers, “Correlation between the Microstructure , Growth Mechanism , and Growth Kinetics of Alumina Scales on a FeCrAlY Alloy,” *Metall. Mater. Trans. A*, vol. 38A, p. 2974, 2007.

[26] A. H. Heuer, “Oxygen and aluminum diffusion in a-Al2O3: How much do we really understand?,” *J. Eur. Ceram. Soc.*, vol. 28, pp. 1495–1507, 2008.

[27] A. H. Heuer *et al.*, “The Band Structure of Polycrystalline Al2O3 and its Influence on Transport Phenomena,” *J. Am. Ceram. Soc.*, vol. 99, no. 3, pp. 733–747, 2016.

[28] A. H. Heuer, D. B. Hovis, J. L. Smialek, and B. Gleeson, “Alumina Scale Formation : A New Perspective,” *J. Am. Ceram. Soc.*, vol. 94, pp. S146–S153, 2011.

[29] W. J. Quadakkers, H. Holzbrecher, K. G. Briefs, and H. Beske, “Differences in growth mechanisms of oxide scales formed on ODS and conventional wrought alloys,” *Oxid. Met.*, vol. 32, no. 1–2, pp. 67–88, 1989.

[30] E. W. A. Young and J. H. W. De Witt, “An 180 Tracer Study on the Growth Mechanism of Alumina Scales on NiAI and NiAIY Alloys,” *Oxid. Met.*, vol. 26, no. 5–6, pp. 351–361, 1986.

[31] S. Kitaoka, T. Matsudaira, and M. Wada, “Mass-Transfer Mechanism of Alumina Ceramics under Oxygen Potential Gradients at High Temperatures,” *Mater. Trans.*, vol. 50, no. 5, p. 1023, 2009.

[32] C. Wagner, “Reaktionstypen bei der Oxydation von Legierungen,” *Zeitschrift fur Elektrochemie*, vol. 63, no. 7, pp. 772–782, 1959.

[33] R. A. Rapp, “Kinetics, Microstructures and Mechanism of Internal Oxidation - Its Effect and Prevention in High Temperature Alloy Oxidation,” *Corrosion*, vol. 21, no. 12, pp. 382–401, 1965.

[34] F. Maak, “Untersuchungen Uber Die Oxydation Von Kupfer-Beryllium-Legierungen Bei Erhohter Temperatur,” *Zeitschrift Fur Met.*, vol. 52, no. 8, pp. 538–545, 1961.

[35] H. Hindam and D. P. Whittle, “High-temperature internal oxidation behavior of dilute nickel-aluminum alloys,” *J. Mater. Sci.*, vol. 18, no. 5, pp. 1389–1404, 1983.

[36] C. Wagner, “Oxidation of Alloys Involving Noble Metals,” *J. Electrochem. Soc.*, vol. 103, no. 10, p. 571, 1956.

[37] C. Wagner, “Passivity and inhibition during the oxidation of metals at elevated temperatures,” *Corros. Sci.*, vol. 5, pp. 751–764, 1965.

[38] B. H. Kear, F. S. Pettit, D. E. Fornwalt, and L. P. Lemaire, “On the transient oxidation of a Ni-15Cr-6Al alloy,” *Oxid. Met.*, vol. 3, no. 6, pp. 557–569, 1971.

[39] P. Tomaszewicz and G. R. Wallwork, “The Oxidation of Fe-Al Alloys Containing Chromium, Nickel, or Manganese,” *Corrosion*, vol. 40, no. 4, pp. 152–157, 1984.

[40] P. R. S. Jackson and G. R. Wallwork, “High temperature oxidation of iron-manganese-aluminum based alloys,” *Oxid. Met.*, vol. 21, no. 3–4, pp. 135–170, 1984.

[41] Y. Kang, “In-Situ And Ex-Situ Studies On Early-Stage Scale Establishment,” University of Pittsburgh, 2016.

[42] H. J. Grabke, M. W. Brumm, and B. Wagemann, “The Oxidation of NiAl,” *Mater. Corros.*, vol. 47, pp. 675–677, 1996.

[43] G. C. Rybicki and J. L. Smialek, “Effect of the Theta-Alpha-Al2O3 transformation on the oxidation behavior of Beta-NiAl + Zr,” *Oxidation of Metals*, vol. 31, no. 3–4. pp. 275–304, 1989.

[44] Y. Kitajima, S. Hayashi, T. Nishimoto, T. Narita, and S. Ukai, “Acceleration of metastable to alpha transformation of Al2O 3 scale on Fe-Al alloy by pure-metal coatings at 900 °c,” *Oxid. Met.*, vol. 75, no. 1–2, pp. 41–56, 2011.

[45] Y. Kitajima and S. Hayashi, “Rapid Formation of a-Al2O3 Scale on an Fe-Al Alloy,” *Oxid. Met.*, vol. 73, pp. 375–388, 2010.

[46] A. Shaaban, S. Hayashi, and K. Azumi, “Effects of nano metal coatings on growth kinetics of α-Al 2O3 formed on Ni-50Al alloy,” *Oxidation of Metals*, vol. 82, no. 1–2. pp. 85–97, 2014.

[47] M. H. Heinonen, K. Kokko, M. P. J. Punkkinen, E. Nurmi, J. Kollár, and L. Vitos, “Initial oxidation of Fe-Al and Fe-Cr-Al alloys: Cr as an alumina booster,” *Oxid. Met.*, vol. 76, no. 3–4, pp. 331–346, 2011.

[48] E. Airiskallio *et al.*, “Third element effect in the surface zone of Fe-Cr-Al alloys,” *Phys. Rev. B - Condens. Matter Mater. Phys.*, vol. 81, no. 3, pp. 8–11, 2010.

[49] E. Airiskallio *et al.*, “High temperature oxidation of Fe-Al and Fe-Cr-Al alloys: The role of Cr as a chemically active element,” *Corros. Sci.*, vol. 52, no. 10, pp. 3394–3404, 2010.

[50] F. S. Pettit, “Oxidation Mechanisms for Ni-Al Alloys at Temperatures Between 900 And 1300 C,” *Trans. Metall. Soc. AIME*, vol. 239, pp. 1296–1305, 1967.

[51] M. S. A. Karunaratne, P. Carter, and R. C. Reed, “On the diffusion of aluminium and titanium in the Ni-rich Ni-Al-Ti system between 900 and 1200°C,” *Acta Mater.*, vol. 49, no. 5, pp. 861–875, 2001.

[52] J. W. Park and C. J. Altstetter, “The diffusion and solubility of oxygen in solid nickel,” *Metall. Trans. A*, vol. 18, no. 1, pp. 43–50, 1987.

[53] W. J. Quadakkers and J. Zurek, “Oxidation in Steam and Steam/Hydrogen Environments,” in *Shrier’s Corrosion*, vol. 1, 2010, pp. 407–456.

[54] J. L. Smialek, “Moisture-induced delayed spallation and interfacial hydrogen embrittlement of alumina scales,” *JOM*, vol. 58, no. 1, pp. 29–35, 2006.

[55] W. Zhao and B. Gleeson, “Assessment of the Detrimental Effects of Steam on Al2O3-Scale Establishment,” *Oxid. Met.*, vol. 83, no. 5–6, pp. 607–627, 2015.

[56] A. Prillieux, D. Jullian, J. Zhang, D. Monceau, and D. J. Young, “Internal Oxidation in Dry and Wet Conditions for Oxygen Permeability of Fe – Ni Alloys at 1150,” *Oxid. Met.*, vol. 87, pp. 273–283, 2017.

[57] R. A. Rapp, “Chemistry and Electrochemistry of Hot Corrosion of Metals,” *Mater. Sci. Eng.*, vol. 87, pp. 319–327, 1987.

[58] D. K. Gupta and R. A. Rapp, “The Solubilities of NiO , Co3O4, and Ternary Oxides in Fused Na2SO4 at 1200 K,” *J. Electrochem. Soc.*, vol. 127, no. 10, p. 2194, 1980.

[59] M. L. Deanhardt and K. H. Stern, “Solubility Products of Metal Oxides in Molten Salts by Coulometric Titration of Oxide Ion Through Zirconia Electrodes,” *J. Electrochem. Soc.*, vol. 128, no. 12, p. 2577, 1981.

[60] P. D. Jose, D. K. Gupta, and R. A. Rapp, “Solubility of α-Al2O3 in Fused Na2SO4 at 1200 K,” *J. Electrochem. Soc.*, vol. 132, no. 3, p. 735, 1985.

[61] Y. S. Zhang and R. A. Rapp, “Solubilities of a-Fe2O3 and Fe3O4 in Fused Na2SO4 at 1200K,” *J. Electrochem. Soc.*, vol. 132, no. 10, p. 2498, 1985.

[62] Y. S. Zhang, “Solubilities of Cr2O3 in Fused Na2SO4 at 1200 K,” *J. Electrochem. Soc.*, vol. 133, no. 3, p. 655, 1986.

[63] D. Shi and R. A. Rapp, “Solubility of SiO2 in fused Na2SO4 at 900 degrees C,” *J. Electrochem. Soc.*, vol. 133, no. 4, p. 849, 1986.

[64] F. S. Pettit and G. H. Meier, “Oxidation and Hot Corrosion of Superalloys,” in *5th International Symposium on Superalloys*, 1984, pp. 651–687.

[65] N. S. Jacobson, “Sodium sulfate: Deposition and dissolution of silica,” *Oxid. Met.*, vol. 31, no. 1–2, pp. 91–103, 1989.

[66] R. A. Rapp and K. S. Goto, “The hot corrosion of metals by molten salts,” in *ECS Proceedings Volumes*, 1981, pp. 159–177.

[67] T. Gheno and B. Gleeson, “On the Hot Corrosion of Nickel at 700 °C,” *Oxid. Met.*, vol. 84, no. 5–6, pp. 567–584, 2015.

[68] N. S. Bornstein and W. P. Allen, “The Chemistry of Sulfidation Corrosion-Revisited,” *Mater. Sci. Forum*, vol. 251–254, pp. 127–134, 1997.

[69] J. L. Smialek, “The Chemistry of Saudi Arabian Sand - A Deposition Problem on Helicopter Turbine Airfoils,” *NASA Technical Memorandum 105234*. Cleveland, Ohio, 1991.

[70] I. Barin, *Thermochemical Data of Pure Substances*, 3rd ed. Wiley, 2008.

[71] J. Stringer and I. G. Wright, “Materials issues in fluidized bed combustion,” *J. Mater. Energy Syst.*, vol. 8, no. 3, pp. 319–331, 1986.

[72] T. Gheno, G. H. Meier, and B. Gleeson, “High Temperature Reaction of MCrAlY Coating Compositions with CaO Deposits,” *Oxid. Met.*, vol. 84, pp. 185–209, 2015.

[73] K. Jung, “Solid Deposit-Induced High Temperature Oxidation,” University of Pittsburgh, 2008.

[74] A. Kaiser, B. Sommer, and E. Woermann, “The System CaO-‘CaCr204’-CaAl2O4 in Air and under Mildly Reducing Conditions,” *J. Am. Ceram. Soc.*, vol. 75, no. 6, pp. 1463–1471, 1992.

[75] (Editors), E. M. Levin, C. R. Robbins, and H. F. McMurdie, *Phase Diagrams for Ceramists, Volume 1*. Columbus, Ohio: The American Ceramic Society, 1964.

[76] G. J. Yurek, J. P. Hirth, and R. A. Rapp, “The Formation of Two-Phase Layered Scales on Pure Metals,” *Oxid. Met.*, vol. 8, no. 5, pp. 265–281, 1974.

[77] W. Weisweiler and S. J. Ahmed, “Kinetics of solid-state reactions in the system CaO-Al2O3,” *Zement-Kalk-Gips*, vol. 33, p. 84, 1980.

[78] M. Gulgun, O. Popoola, and W. Kriven, “Chemical Synthesis and Characterization of Calcium Aluminate Powders,” *J. Am. Ceram. Soc.*, vol. 77, no. 2, p. 531, 1994.

[79] B. M. Mohamed and J. H. Sharp, “Kinetics and mechanism of formation of monocalcium aluminate , CaAl2O4,” *J. Mater. Chem.*, vol. 7, no. 8, pp. 1595–1599, 1997.

[80] C. Ghoroi and A. K. Suresh, “Solid-solid reaction kinetics: Formation of tricalcium aluminate,” *AIChE J.*, vol. 53, no. 2, pp. 502–513, 2007.

[81] V. Nagarajan, R. D. Smith, and I. G. Wright, “Corrosion of nickel-base and iron-base alloys in a simulated fluidized-bed coal-combustion environment,” *Oxid. Met.*, vol. 31, no. 1–2, pp. 123–143, 1989.

[82] W. M. Swift, A. F. Panek, G. W. Smith, G. J. Vogel, and A. A. Janke, “Decomposition of Calcium Sulfate: a Review of the Literature.” pp. 1–64, 1976.

[83] I. Colussi and V. Longo, “La Decomposizione Termica Del Solfato Di Calcio,” *Cem.*, vol. 2, pp. 75–98, 1974.

[84] C. F. Beaton, *Heat Exchanger Design Handbook*. Hemisphere Publishing Corp, 1986.

[85] K. Jung, F. S. Pettit, and G. H. Meier, “The Effect of Ca-rich Deposits on the High Temperature Degradation of Coated and Uncoated Superalloys,” *Mater. Sci. Forum*, vol. 595–598, pp. 805–812, 2008.

[86] Y. El Khessaimi, Y. El Hafiane, A. Smith, R. Trauchessec, C. Diliberto, and A. Lecomte, “Solid-state synthesis of pure ye’elimite,” *J. Eur. Ceram. Soc.*, vol. 38, pp. 3401–3411, 2018.

[87] D. G. Konitzer and GE Aviation, “Personal Communications.” .

[88] S. Y. Hong, A. B. Anderson, and J. L. Smialek, “Sulfur at nickel-alumina interfaces. Molecular orbital theory,” *Surf. Sci.*, vol. 230, no. 1–3, pp. 175–183, 1990.

[89] J. L. Smialek, “Effect of sulfur removal on Al2O3 scale adhesion,” *Metall. Trans. A*, vol. 22A, no. 3, pp. 739–752, 1991.

[90] H. J. Grabke, D. Wiemer, and H. Viefhaus, “Segregation of sulfur during growth of oxide scales,” *Appl. Surf. Sci.*, vol. 47, pp. 243–250, 1991.

[91] J. Smialek and B. Pint, “Optimizing Single Scale Adhesion Superalloys on Single Crystal Superalloys,” *Mater. Sci. Forum*, vol. 369–372, pp. 459–466, 2001.

[92] J. A. Haynes, B. A. Pint, K. L. More, Y. Zhang, and I. G. Wright, “Influence of sulfur, platinum, and hafnium on the oxidation behavior of CVD NiAl bond coatings,” *Oxid. Met.*, vol. 58, no. 5–6, pp. 513–544, 2002.

[93] B. A. Pint, “On the Formation of Interfacial and Internal Voids in a-Al203 Scales,” *Oxid. Met.*, vol. 48, no. 3/4, pp. 24–27, 1997.

[94] D. R. Clarke, “Stress generation during high-temperature oxidation of metallic alloys,” *Curr. Opin. Solid State Mater. Sci.*, vol. 6, pp. 237–244, 2002.

[95] S. Timoshenko, “Bending and buckling of bimetallic strips,” *J. Opt. Soc. Am.*, vol. 11, p. 233, 1925.

[96] J. A. Goebel and F. S. Pettit, “The influence of sulfides on the oxidation behavior of nickel-base alloys,” *Metall. Trans.*, vol. 1, no. 12, pp. 3421–3429, 1970.

[97] B. Schramm and W. Auer, “Sulfidation behaviour of nickel aluminides,” *Mater. Corros.*, vol. 47, no. 12, pp. 678–684, 1996.

[98] C. J. Spengler and R. Viswanathan, “Effect of Sequential Sulfidation and Oxidation on the Propagation of Sulfur in an 85 Ni-15 Cr Alloy,” *Metall. Trans.*, vol. 3, pp. 161–166, 1972.

[99] J. L. Meijering, *Advances in Materials Science*. Wiley, 1971.

[100] P. Carter, B. Gleeson, and D. J. Young, “Calculation of Precipitate Dissolution Zone Kinetics in Oxidising Binary Two-Phase Alloys,” *Acta Mater.*, vol. 44, no. 10, pp. 4033–4038, 1996.

[101] A. Martínez-Villafañe, F. H. Stott, J. G. Chacon-Nava, and G. C. Wood, “Enhanced oxygen diffusion along internal oxide-metal matrix interfaces in Ni-Al alloys during internal oxidation,” *Oxid. Met.*, vol. 57, no. 3–4, pp. 267–279, 2002.

[102] F. H. Stott, G. C. Wood, D. P. Whittle, B. D. Bastow, Y. Shida, and A. Martinez-Villafane, “The Transport of Oxygen to the Advancing Internal Oxide Front During Internal Oxidation of Nickel-Base Alloys at High Temperature,” *Solid State Ionics*, vol. 12, pp. 365–374, 1984.

[103] D. L. Douglass, B. Zhu, and F. Gesmundo, “Internal-Oxide-Band Formation During Oxidation of Ag-Mg Alloys,” *Oxid. Met.*, vol. 38, pp. 365–384, 1992.

[104] D. L. Douglass, “Anomalous Behavior During Internal Oxidation and Nitridation,” *J. Mater.*, vol. 43, no. 11, pp. 74–79, 1991.

[105] B. A. Bosch, F. V. Lenel, and G. S. Ansell, “The Influence of the Rate of Oxidation Upon the properties of Internally Oxidized Silver-Magnesium Alloys,” *Trans. Am. Soc. Met.*, vol. 57, p. 960, 1964.

[106] P. J. Fink, J. L. Miller, and D. G. Konitzer, “Rhenium Reduction - Alloy Design Using an Economically Strategic Element,” *J. Mater.*, vol. 62, no. 1, pp. 55–57, 2010.

[107] F. S. Pettit and G. H. Meier, “The effects of refractory elements on the high temperature oxidation and hot corrosion properties of superalloys,” in *Refractory Alloying Elements in Superalloys*, 1984, p. 165.

[108] S. Park, S. Seo, Y. Yoo, H. Jeong, and H. Jang, “Statistical Study of the Effects of the Composition on the Oxidation Resistance of Ni-Based Superalloys,” *J. Nanomater.*, vol. 2015, 2015.

[109] B. Pint, “Optimization of Reactive-Element Additions to Improve Oxidation Performance of Alumina-Forming Alloys,” *J. Am. Ceram. Soc.*, vol. 86, no. 4, pp. 686–95, 2003.

[110] T. Gheno *et al.*, “A Thermodynamic Approach to Guide Reactive Element Doping: Hf Additions to NiCrAl,” *Oxid. Met.*, vol. 87, no. 3, pp. 297–310, 2017.

[111] K. Matsugi, Y. Murata, M. Morinaga, and N. Yukawa, “Realistic Advancement for Nickel-Based Single Crystal Superalloys by the d-Electrons Concept,” in *Superalloys*, 1992, pp. 307–316.

[112] C. T. Liu, X. F. Sun, H. R. Guan, and Z. Q. Hu, “Effect of rhenium addition to a nickel-base single crystal superalloy on isothermal oxidation of the aluminide coating,” *Surf. Coatings Technol.*, vol. 194, no. 1, pp. 111–118, 2005.

[113] L. Huang, X. F. Sun, H. R. Guan, and Z. Q. Hu, “Effect of rhenium addition on isothermal oxidation behavior of single-crystal Ni-based superalloy,” *Surf. Coatings Technol.*, vol. 200, pp. 6863–6870, 2006.

[114] Q. Zeng, S. W. Ma, Y. R. Zheng, S. Z. Liu, and T. Zhai, “A study of Re and Al diffusion in Ni,” *J. Alloys Compd.*, vol. 480, pp. 987–990, 2009.